

## Protocol



# RNA sample optimization for cryo-EM analysis

Xingyu Chen<sup>1,7</sup>, Liu Wang<sup>1,7</sup>, Jiahao Xie<sup>1,7</sup>, Jakub S. Nowak<sup>3</sup>, Bingnan Luo<sup>1,6</sup>, Chong Zhang<sup>1</sup>, Guowen Jia<sup>1</sup>, Jian Zou<sup>1</sup>, Dingming Huang<sup>2</sup>, Sebastian Glatt<sup>1,3,4</sup>, Yang Yang<sup>5</sup> & Zhaoming Su<sup>1</sup>✉

## Abstract

RNAs play critical roles in most biological processes. Although the three-dimensional (3D) structures of RNAs primarily determine their functions, it remains challenging to experimentally determine these 3D structures due to their conformational heterogeneity and intrinsic dynamics. Cryogenic electron microscopy (cryo-EM) has recently played an emerging role in resolving dynamic conformational changes and understanding structure–function relationships of RNAs including ribozymes, riboswitches and bacterial and viral noncoding RNAs. A variety of methods and pipelines have been developed to facilitate cryo-EM structure determination of challenging RNA targets with small molecular weights at subnanometer to near-atomic resolutions. While a wide range of conditions have been used to prepare RNAs for cryo-EM analysis, correlations between the variables in these conditions and cryo-EM visualizations and reconstructions remain underexplored, which continue to hinder optimizations of RNA samples for high-resolution cryo-EM structure determination. Here we present a protocol that describes rigorous screenings and iterative optimizations of RNA preparation conditions that facilitate cryo-EM structure determination, supplemented by cryo-EM data processing pipelines that resolve RNA dynamics and conformational changes and RNA modeling algorithms that generate atomic coordinates based on moderate- to high-resolution cryo-EM density maps. The current protocol is designed for users with basic skills and experience in RNA biochemistry, cryo-EM and RNA modeling. The expected time to carry out this protocol may range from 3 days to more than 3 weeks, depending on the many variables described in the protocol. For particularly challenging RNA targets, this protocol could also serve as a starting point for further optimizations.

## Key points

- This protocol describes an iterative workflow to optimize RNA preparation conditions for cryo-EM analysis. Cryo-EM data processing to resolve RNA conformational changes and modeling into cryo-EM density are also described.
- Existing protocols have not extensively described the variables in RNA sample preparation, cryo-EM data processing and modeling, thus are difficult to standardize. Our iterative approach is generally applicable to RNAs and can serve as a starting point for challenging RNAs.

## Key references

Kappel, K. et al. *Nat. Methods* **17**, 699–707 (2020); <https://doi.org/10.1038/s41592-020-0878-9>

Luo, B. et al. *Nat. Catal.* **6**, 298–309 (2023); <https://doi.org/10.1038/s41929-023-00934-3>

<sup>1</sup>The State Key Laboratory of Biotherapy, Department of Geriatrics and National Clinical Research Center for Geriatrics, West China Hospital, Sichuan University, Chengdu, China. <sup>2</sup>The State Key Laboratory of Oral Diseases, National Clinical Research Center for Oral Diseases, National Center for Stomatology, Department of Cardiology and Endodontics, West China Hospital of Stomatology, Sichuan University, Chengdu, China. <sup>3</sup>Malopolska Centre of Biotechnology, Jagiellonian University, Krakow, Poland. <sup>4</sup>Department for Biological Sciences and Pathobiology, University of Veterinary Medicine Vienna, Vienna, Austria. <sup>5</sup>Department of Prosthodontics, West China Hospital of Stomatology, Sichuan University, Chengdu, China. <sup>6</sup>Present address: Department of Molecular Biophysics and Biochemistry, Yale University, New Haven, CT, USA. <sup>7</sup>These authors contributed equally: Xingyu Chen, Liu Wang, Jiahao Xie. ✉e-mail: [zsu@wchscu.cn](mailto:zsu@wchscu.cn)

## Introduction

RNAs participate in various essential biological processes with fundamental cellular functions, such as catalysis and regulation of transcription, translation and signaling pathways<sup>1–3</sup>. Three-dimensional (3D) structures of RNAs primarily determine their functions<sup>4</sup>, e.g., ribozymes form compact core structures to catalyze reactions<sup>5–7</sup>, riboswitches sense ligands of different sizes and environmental changes to regulate gene expressions<sup>8,9</sup>; long noncoding RNAs (lncRNAs) fold into structures and interact with proteins to perform their functions<sup>10–12</sup>.

When the structured RNAs carry out their functions *in vitro* or *in vivo*, their structural domains may undergo large conformational changes and individual nucleotides may undergo local dynamic changes<sup>13–18</sup>. This complicates the preparation of homogeneous RNA samples for structure determination. In addition, conventional structural biology techniques, such as X-ray crystallography, nuclear magnetic resonance (NMR) and cryogenic electron microscopy (cryo-EM) single particle analysis (SPA), all have their technical limitations when dealing with different levels of heterogeneity that collectively pose great challenges to high-resolution 3D structural analyses of RNAs. X-ray crystallography generally requires a large quantity of RNAs baring minimal heterogeneity on global RNA architectures to facilitate molecule packing and lattice formation during crystal growth<sup>19</sup>. Occasionally, conformational changes of structural domains may be observed<sup>20</sup>. NMR is mostly useful in studying the dynamics of individual nucleotide and base tautomerizations of relatively small RNAs with the average size of 30 nucleotides (30 nt) in both low-energy steady states and high-energy excited states<sup>21,22</sup>. Cryo-EM SPA can resolve global conformational changes and local dynamics of nucleotides and ions in relatively large RNAs and their complexes at near-atomic resolution<sup>23</sup>. However, the lower molecular size limit of RNA studied so far is 88 nt (ref. 24), and the majority of RNA cryo-EM structures were resolved at moderate- (4–10 Å) to low resolution (>10 Å)<sup>23</sup>, precluding *de novo* modeling. To study RNA structure–function relationships with density maps at a wide range of resolutions, several RNA modeling algorithms have been recently developed to generate atomic RNA coordinates into cryo-EM density<sup>25–31</sup>.

## Development of the protocol

Here, we present a protocol for the optimization of RNA preparation conditions for cryo-EM structure determination. This protocol is developed for RNAs that form 3D structures to carry out their functions. Structural analyses of such RNAs with well-characterized functions can elucidate their molecular mechanisms. Several methods have been recently developed to determine cryo-EM structures of RNAs with diverse functions and various molecular weights under a wide range of conditions. These include ‘Ribosolve’ that provides a rapid cryo-EM-guided RNA structure determination pipeline<sup>25</sup>, as well as other methods such as oligomeric and higher-order assembly to facilitate cryo-EM analysis<sup>32,33</sup>, and utilizations of large scaffolding RNAs to enable cryo-EM structure determination of small RNAs<sup>34,35</sup>.

Although these recent advances have enabled more efficient RNA structure determination in the past few years (Table 1), RNA structures remain largely underrepresented compared with proteins in both the Protein Data Bank (PDB)<sup>36</sup> and the Electron Microscopy Data Bank<sup>37</sup>, which could be one of the leading reasons for less accurate RNA structure predictions compared with proteins<sup>38,39</sup>. This highlights the need for a systematic protocol that can be generally applied to cryo-EM structure determination of RNAs. In the meantime, we do realize the challenges of proposing such protocols for RNAs, because even for more streamlined protein cryo-EM structure determination, many variables in sample preparation and vitrification need to be iteratively optimized, mostly requiring user expertise and experience. This makes existing protocols difficult to standardize as their effects vary by samples<sup>40</sup>. However, establishment of such protocols for RNAs may enable more biological questions to be answered and may potentially contribute to the continuous growth of the field, so that it eventually develops better solutions to tackle these challenges.

Most methods consist of the following stages: (i) RNA *in vitro* transcription (IVT) and purification followed by native polyacrylamide gel electrophoresis (PAGE) for fast and

**Table 1 | Summary of protein-free RNA cryo-EM structures**

RNA specimen (reference)	Molecular weight (nt/kDa)	Resolution (Å)	RNA folding buffer	Screening method	Grid	Data processing	Modeling
Dimeric rCBL <sup>200</sup>	210/70	3.0–5.3	50 mM MES, pH 6.0, 10 mM KCl, 1 mM MgCl <sub>2</sub>	AFM	300 mesh Au R1.2/1.3 Quantifoil	Relion, CryoSPARC, SIMPLE3	Coot, Phenix
Cotranscriptionally folded <i>O. iheyensis</i> group II intron with a thiamine pyrophosphate riboswitch ( <i>O.i.-TPP</i> ) <sup>201</sup>	497/165	2.4–4.7	5 mM Na-cacodylate pH 6.5, 4 mM MgCl <sub>2</sub>	N/A	300 mesh Cu R1.2/1.3 Quantifoil, 300 mesh Au-flat 1.2/1.3 ProtoChips	Relion, CryoSPARC	Coot, Phenix
HIV-1 DIS <sup>202</sup>	94/31	9.0	20 mM Tris-HCl, pH 7.4, 5 mM NaCl, 140 mM KCl, 1 mM MgCl <sub>2</sub>		200 mesh Cu R1.2/1.3 Quantifoil	EMAN2, Relion	N/A
Cotranscriptionally folded <i>B. subtilis</i> glyQS T-box-tRNA <sup>Gly</sup> <sup>203</sup>	244/79	4.9	10 mM Tris-HCl, pH 7.4, 100 mM KCl, 20 mM MgCl <sub>2</sub>	PAGE	200 mesh Cu R2/1 Quantifoil		Coot, Phenix
<i>M. smegmatis</i> ileS (MS) T-box-tRNA <sup>Ile</sup> <sup>204</sup>	299/74	6.3	20 mM Tris-HCl, pH 7.9, 20 mM NaCl, 10 mM MgCl <sub>2</sub> ,		200 mesh Cu R2/2 Quantifoil	EMAN2, Relion, CryoSPARC	Coot, Phenix, Auto-DRAFTER
MS S3.11-T-box-tRNA <sup>Ile</sup> <sup>204</sup>	251/81	9.6	0.1 mM EDTA				
MS T-box-acc.11-tRNA <sup>Ile</sup> <sup>204</sup>	251/81	7.5					
MS S3.11-T-box-acc.11-tRNA <sup>Ile</sup> <sup>204</sup>	273/88	6.9					
Self-assembled <i>Tetrahymena</i> ribozyme <sup>32</sup>	393/127	2.9–4.1	20 mM Tris-HOAc, pH 8.0, 10–30 mM MgCl <sub>2</sub>		400 mesh R1.2/1.3 Quantifoil	Relion, SPIDER	Coot, Phenix
Trimeric Azoarcus group I intron <sup>32</sup>	223/69	4.9					
Trimeric FMN riboswitch <sup>32</sup>	132/41	5.9					
Cotranscriptionally folded 5TU-t1 heterodimeric triplet polymerase ribozyme <sup>205</sup>	287/92	5.0	50 mM Tris-HCl, pH 8.0, 100 mM MgCl <sub>2</sub>	PAGE, negative stain	300 mesh Au-flat 1.2/1.3 ProtoChips	CryoSPARC	Phenix, DRRAFTER, ISOLDE, QRNAS
ScRNA and cmpRNA complexes <sup>206</sup>	142/43	5.3–9.7		PAGE			Phenix, RNAbuild, ISOLDE
Cotranscriptionally folded <i>Tetrahymena</i> group I intron <sup>14</sup>	~450/150	2.8–4.0	40 mM Tris-HCl, pH 7.0–7.9, 0.01% TritonX-100,		200 mesh Au R2/1 Quantifoil	EMAN2, Relion	Coot, Phenix, DRRAFTER, SimRNA
Cotranscriptionally folded circularly permuted (CP) <i>C. testosterone</i> (Cte 1) group II intron <sup>207</sup>	728/225	2.9	6–20 mM MgCl <sub>2</sub> , 2 mM spermidine, 10 mM DTT		200 mesh R1.2/1.3 with 2 nm C film Quantifoil	EMAN2, Relion, CryoSPARC	Coot, Phenix
CP Cte 1 group II intron catalytic states <sup>207</sup>	814/251	2.6–3.0	10 mM Tris-HCl, pH 7.5, 100 mM KCl, 20 mM CaCl <sub>2</sub>				
CP <i>Tetrahymena</i> ribozyme appended with other RNAs <sup>35,208</sup>	~450/150	2.4–5.1	50 mM Tris-HCl, pH 7.5, 10 mM MgCl <sub>2</sub>		400 mesh C-flat R1.2/1.3 EMS	CryoSPARC	
Hydrolytic endonuclease ribozyme <sup>209</sup>	633/195	2.6–3.4	20–40 mM HEPES, pH 7.5–8.0, 50 mM KCl, 5–10 mM MgCl <sub>2</sub>		300 mesh Au R1.2/1.3 with GO Quantifoil		
Cotranscriptionally folded RNA origami paranemic-crossover triangle <sup>99</sup>	238/76	5.4–6.6		PAGE, negative stain	300 mesh Au-flat 1.2/1.3 ProtoChips		RNAbuild, ISOLDE, Phenix, QRNAS
Cotranscriptionally folded RNA origami 5HT <sup>98</sup>	~560/180	4.1–5.7				CryoSPARC, Warp	
Cotranscriptionally folded RNA origami 6HBC <sup>98</sup>	720/232	4.9–5.7					
Cotranscriptionally folded RNA origami 3-helix tile Traptamer <sup>210</sup>	363/117	5.4		N/A		CryoSPARC	
Cotranscriptionally folded RNA origami with appended fluorescence aptamers <sup>33</sup>	374/121	4.4–4.6					

# Protocol

**Table 1 (continued) | Summary of protein-free RNA cryo-EM structures**

RNA specimen (reference)	Molecular weight (nt/kDa)	Resolution (Å)	RNA folding buffer	Screening method	Grid	Data processing	Modeling
ATP-TTR-3 <sup>25</sup>	130/42	9.6–10	50 mM Na-HEPES, pH 8.0, 10 mM MgCl <sub>2</sub>	PAGE	200 mesh Cu R2/1, R3.5/1 and 300 mesh Cu R1.2/1.3 Quantifoil	EMAN2, Relion, CryoSPARC	Coot, Phenix, Auto-DRRAFTER, FARFAR2
<i>F. nucleatum</i> glycine riboswitch <sup>25</sup>	171/55	7.4–10					
HC16 ligase <sup>25</sup>	349/113	10					
<i>Mycobacterium</i> SAM-IV riboswitch <sup>25</sup>	119/39	3.7–4.8					
<i>V. cholerae</i> glycine riboswitch <sup>25</sup>	231/75	4.8–5.7					
Tetrahymena ribozyme (apo, holo, misfolded states) <sup>25,66,101,211,212</sup>	~400/130	2.4–6.8					
SARS-CoV-2 FSE <sup>24</sup>	88/28	6.9					
SARS-CoV-2 SL5 <sup>213</sup>	124/40	4.7		N/A		CryoSPARC	Phenix, Auto-DRRAFTER, ERRASER2
SARS-CoV-1 SL5 <sup>213</sup>	143/46	7.1					
BtCoV-HKU5 SL5 <sup>213</sup>	135/44	5.9–7.3					
MERS-CoV SL5 <sup>213</sup>	135/43	6.4–6.9					
SARS-CoV-2 SL5 <sup>214</sup>	145/47	6.5	20 mM HEPES, pH 7.5, 50 mM NaCl, 50 mM KCl, 1 mM MgCl <sub>2</sub> /DTT	PAGE, AFM	200 mesh Cu R2/2 Quantifoil		Phenix, SimRNA, QRNAs
OC43-CoV SL5 <sup>214</sup>	222/72	7.1					
RoBat-CoV SL5 <sup>214</sup>	118/38	6.6					
MERS-CoV SL5 <sup>214</sup>	156/50	5.9					
Misfolded Tetrahymena ribozyme <sup>100</sup>	387/125	3.9	50 mM Na-MOPS, pH 7.0, 10 mM MgCl <sub>2</sub>	N/A	400 mesh C-flat R1.2/1.3 EMS	Relion, CryoSPARC	Coot, Phenix, Auto-DRRAFTER, CRYSTAL
Bromo mosaic virus tRNA-like structure RNA <sup>15</sup>	171/55	4.3		PAGE			Coot, Phenix, Auto-DRRAFTER, ERRASER, Namidator
Cotranscriptionally folded dENE-poly(A) <sub>28</sub> complex <sup>215</sup>	104/33	5.6	10 mM MOPS, pH 7.0, 50 mM KCl, 0.025 mM EDTA, 1 mM MgCl <sub>2</sub>		200 mesh Cu R2/1 Quantifoil	EMAN2, Relion, CryoSPARC	Coot, Refmac

FSE, frameshift stimulation element; MES, 2-(N-morpholino)ethanesulfonic acid; MOPS, 3-(N-morpholino)propanesulfonic acid; SL5, stem-loop 5.

inexpensive examination of RNA preparation and folding conditions; (ii) secondary structure probing; (iii) cryo-EM SPA to obtain density maps at subnanometer to near-atomic resolutions; and (iv) RNA modeling based on secondary structures and cryo-EM density maps. In the current protocol, we aim to present an iterative optimization process based on this workflow that we have used for RNA sample and grid preparation for subsequent cryo-EM reconstruction and modeling<sup>14,25</sup>. We have expanded our optimization pipeline to include considerations based on the literature and user experiences from our and other laboratories worldwide.

Our protocol allows for iteration through variables in RNA preparation conditions, including pH, buffer compositions, ion concentrations and additives such as detergents. These can be assessed by the most commonly used PAGE, complemented by alternative methods that provide additional information on sample properties with better resolution or higher throughput, e.g., dynamic light scattering (DLS and nanoDLS)<sup>41</sup>. We also allow for iteration through RNA vitrification conditions such as different types of grids, supporting films, grid pretreatments and blotting conditions, which can be tested by cryo-EM visualizations and preliminary data collections. Optimized specimens can then be subjected to large-scale data collections and processing to resolve RNA heterogeneity at optimal resolution, and RNA modeling algorithms can be used to generate atomic coordinates based on cryo-EM density maps at subnanometer to near-atomic resolutions.

The protocol is modular and most hardware (e.g., freezing apparatuses, microscopes and cameras) and software (e.g., data collection and processing schemes and RNA modeling algorithms) are interchangeable and can be combined to fit the users' needs. Multiple protocols of RNA preparations for structural analyses<sup>42–45</sup> and standard high-resolution cryo-EM SPA have

# Protocol

been described<sup>45–48</sup>, and similar steps shared among these protocols are simplified but retained in the current protocol for integrity purpose.

## Overview of the procedure

A schematic workflow of the protocol is shown in Figs. 1 and 2. Linearized DNA templates are prepared by either PCR or plasmid amplification followed by enzymatic digestion (Steps 1–4), in which additional ribozyme sequences and primer modifications can be introduced to ensure 5' and 3' end homogeneity<sup>49–51</sup>. Subsequently, IVT is usually carried out with T7 RNA polymerase (RNAP) or its variants under conditions optimized for maximal yield and homogeneity (Steps 5–6)<sup>52</sup>.

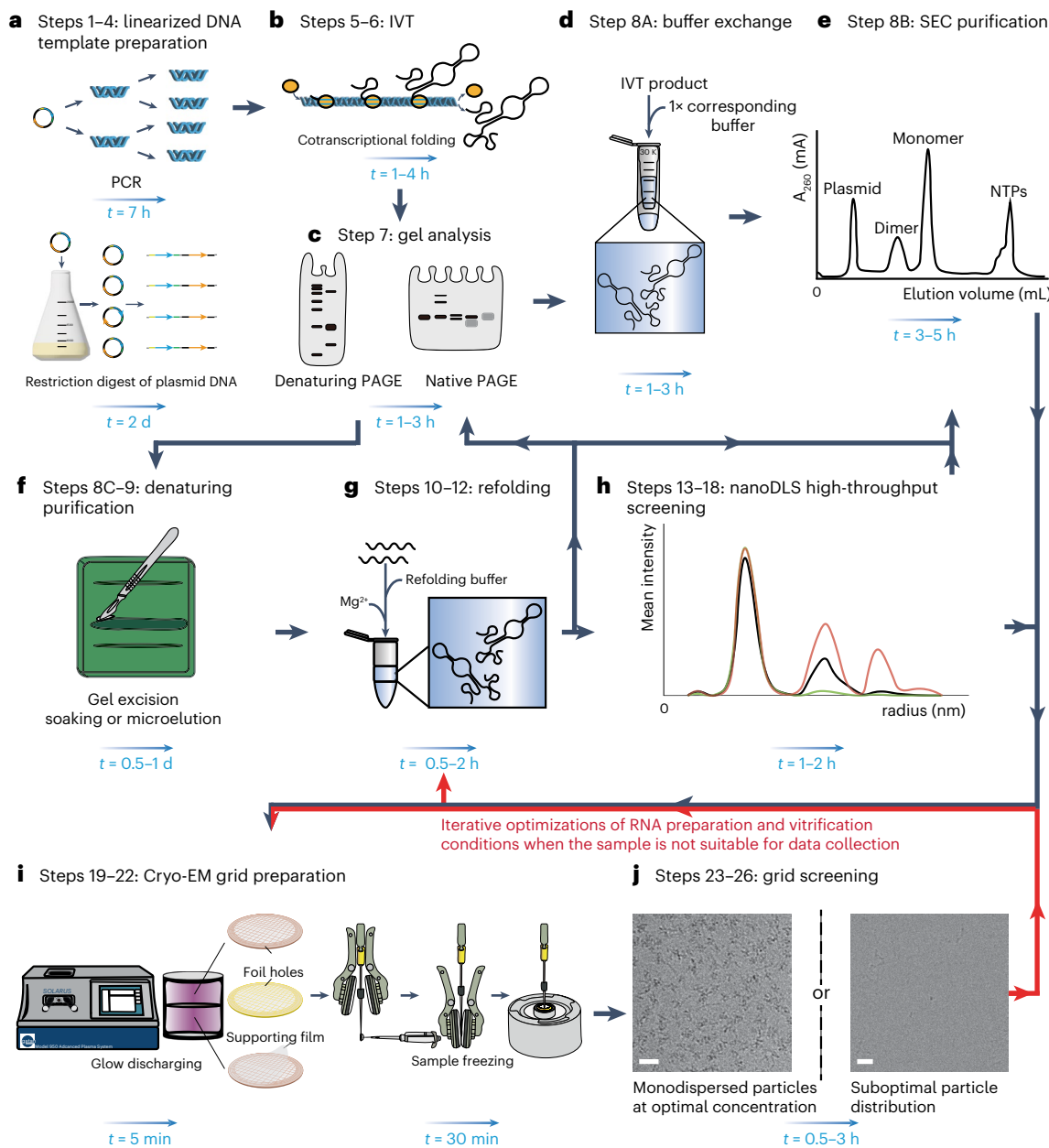


**Fig. 1 | Workflow for RNA sample optimization.** This figure relates to Steps 1–26. A–j, A schematic illustration showing the stages of linearized DNA template preparation (a), IVT (b), PAGE analysis (c), buffer exchange (d), SEC purification (e), RNA denaturing gel purification (f), RNA refolding (g), nanoDLS

high-throughput screening (h), cryo-EM grid preparation (i) and cryo-EM grid screening (j). The time required for each stage is indicated in blue. White scale bars, 20 nm. Black arrows indicate workflow direction and red arrows indicate iterative optimization direction.

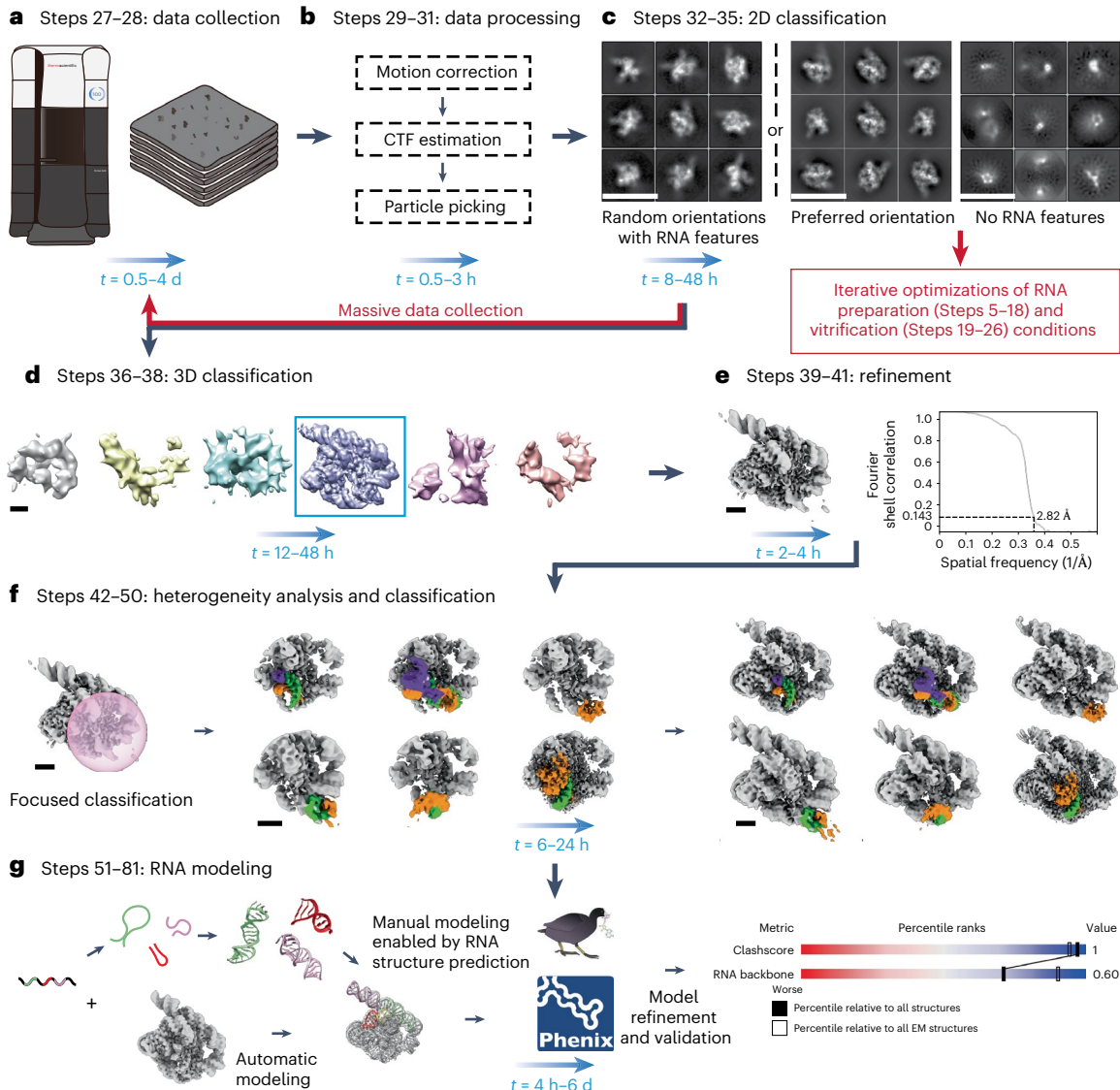


**Fig. 2 | Cryo-EM analysis and modeling of optimized RNA samples.** This figure relates to Steps 27–81. **a–g**, A schematic illustration showing the steps of cryo-EM data collection (**a**), data processing (**b**), 2D classification (**c**), 3D classification (**d**), 3D refinement (**e**), RNA heterogeneity analysis and focused classification (**f**) and

RNA modeling (**g**). The time required for each stage is indicated in blue. White scale bars, 20 nm; black scale bars, 2 nm. The images in **f** were adapted from ref. 14, Springer Nature Limited.

After IVT, the resulting RNA homogeneity can be quickly evaluated by the denaturing PAGE, whereas the folding status can be assessed by native PAGE (Step 7). Cotranscriptionally folded RNAs can be directly concentrated by buffer exchange (Step 8A), or purified by size exclusion chromatography (SEC), in which different conformations can be separated (Step 8B)<sup>42,43,53</sup>. However, if the IVT product is heterogeneous, conventional denaturing gel purification and RNA refolding under appropriate conditions will be required (Steps 8C–11). These steps are also useful in capturing particular RNA conformations such as misfolded states and intermediate states during substrate binding and catalysis. Aside from native PAGE screening of RNA refolding conditions (Step 12)<sup>34</sup>, we also describe steps for nanoDLS to screen for optimal IVT and RNA refolding conditions with higher throughput (Steps 13–18)<sup>41</sup>.

Purified RNAs are then vitrified and assessed under the cryo-electron microscope (Steps 19–26). Iterative optimizations of RNA preparation conditions (Steps 5–18) and vitrification

conditions (Steps 19–26) may be required to attain grids with an overall optimal ice thickness and uniform particle size and distribution, which are subjected to preliminary data collections of typically a few hundred movie stacks (Steps 27–28). Data processing can normally pause upon completion of two-dimensional (2D) classification for initial evaluation (Steps 29–35). A lack of RNA features indicates the need to optimize RNA preparation and/or vitrification conditions through iterations of Steps 5–22. The final optimized RNA samples are subjected to large-scale cryo-EM data collections by repeating and extending the collection time in Steps 27–28.

Most RNAs undergo conformational changes when performing their functions, which can now be more efficiently separated by recently developed 3D classification algorithms in addition to the standard cryo-EM data processing pipeline (Steps 36–50). It is common to obtain RNA cryo-EM maps at moderate resolution that hinder de novo modeling<sup>23</sup> (Table 1), which may be overcome by the latest automated RNA modeling algorithms combined with manual curations and refinements (Steps 51–81).

## Application of the protocol

Advances in sequencing methods allow the discovery of thousands of RNA families that have been deposited in the database of Rfam<sup>55</sup>. Among those RNAs expected to adopt 3D structures, however, only 136 RNA families have experimentally determined structures available in the PDB and Nucleic Acids Database<sup>56</sup>. As of July 2024, data from the PDB showed that the majority (94%) of protein-free RNA 3D structures were determined by X-ray crystallography and NMR. In principle, the current protocol that relies on cryo-EM is complementary to X-ray crystallography and NMR and should be applicable to RNAs of 70 nt or larger that form 3D structures<sup>57</sup>.

Cryo-EM is especially useful for large RNAs and ribonucleoproteins, making this protocol potentially applicable for functional lncRNAs<sup>58</sup>, especially those whose structures have already been investigated by other methods. For example, small-angle X-ray scattering (SAXS) has revealed the overall shapes of Bvht before and after binding to its protein partner CNBP<sup>59,60</sup>, HOTAIR and MEG3 have been visualized by atomic force microscopy (AFM) to form flexible elongated shapes<sup>61,62</sup>, the primary microRNA cluster miR-17/92, also known as oncomiR-1 (ref. 63), has been found to form a compact globular shape under negative staining electron microscopy<sup>64</sup> and 7SK noncoding RNA forms a core ribonucleoprotein with MePCE and Larp7 that could undergo conformational change between the ‘linear’ and ‘circular’ forms, as recently revealed by cryo-EM<sup>65</sup>. Additional cryo-EM analysis of either the full-length or isolated functional domains of these lncRNAs could provide mechanistic insights into their functions.

Many noncoding RNAs carry out their functions in the presence of other binding partners, which are mostly proteins and sometimes RNAs or small molecules. Studying the RNA-only structures enables elucidations of conformational changes that occur during binding and complex formation. For example, a viral tRNA-like structure of bromo mosaic virus was found to undergo substantial conformational change upon binding to the host tRNA synthetase<sup>15</sup>, the *Tetrahymena* group I intron could undergo large conformational changes during substrate binding and catalysis<sup>14,66</sup> and the SAM-IV riboswitch preformed the binding pocket for S-adenosyl methionine (SAM) binding<sup>67</sup>.

RNAs as drug targets are of particular interests to pharmaceutical industry given that RNAs transcribed from the human genome outnumber translated proteins by more than 50-fold<sup>68</sup>. A recent study discovered small molecules that regulate the dynamic conformational changes of Xist RepA<sup>69,70</sup>. Moreover, risdiplam that targets SMN2 pre-mRNA and corrects alternative splicing to treat spinal muscular atrophy was recently approved by the US Food and Drug Administration<sup>71,72</sup>. This protocol may help to elucidate the structure basis of RNA-targeted small molecule mode-of-action by cryo-EM in complementary to X-ray crystallography and NMR, and to promote structure-based RNA-targeted drug discovery.

## Comparison with other methods

### RNA preparation

The RNA preparation section of this protocol is generally applicable to all structure determination *in vitro*. IVT and RNA refolding conditions are often separately screened and optimized to obtain the most thermodynamically stable RNA conformations.

Native PAGE is widely accessible to assess different conditions in most laboratories. Acrylamide and bis-acrylamide polymerize into mesh-like gel matrix to separate RNAs adopting different conformations or forming complexes with different substrates, which lead to different electrophoretic mobility rates<sup>54,73</sup>. Migrations of RNA molecules are determined mostly by the dynamics of RNA conformation exchange and thus cannot be easily predicted by their physical properties.

To enhance the versatility of the current protocol, we include nanoDLS in the condition screening steps that provides information on polydispersity and hydrodynamic radius of folded RNAs with the option of analyzing different samples/conditions in parallel at a higher throughput<sup>41</sup>. Other methods such as analytical ultracentrifuge and capillary electrophoresis can also be used. Analytical ultracentrifuge measures the sedimentation velocity of RNA samples in solution to provide information of particle size, shape and diffusion<sup>74</sup>, while capillary electrophoresis can separate different RNA conformations and lengths with high sensitivity based on their migration rates through capillaries under an electric field<sup>75</sup>.

## Structure determination

Cryo-EM SPA requires a minimal amount of samples flash frozen in vitreous ice that preserve native conformations. The continuously advancing algorithms can better resolve RNA dynamics and conformational changes. Cryo-EM SPA is complementary to alternative structural biology methods such as X-ray crystallography and NMR that provide atomic RNA coordinates, and SAXS and AFM that provide low-resolution envelopes and shape information<sup>76</sup>.

X-ray crystallography: X-ray crystallography requires large sample quantities and the successful growth of RNA crystals that diffract to high resolution, which apparently has been challenging for numerous RNAs<sup>77,78</sup>. As a result, sequence alterations based on extensive sequence alignments, functional studies and biophysical/biochemical characterizations that minimally disrupt tertiary structures continue to play an essential role to optimize crystallization conditions, crystal packing and diffraction quality<sup>77</sup>. On the contrary, cryo-EM allows direct visualization and determination of structures of wild-type full-length RNAs<sup>23</sup>.

NMR: NMR is capable of resolving RNA structures and their dynamics at atomic level in biologically relevant conditions by measuring the chemical shifts of the resonance frequencies of the nuclear spin<sup>76,79,80</sup>. However, as RNA becomes larger, the spectral signals overlap and broaden and there is a loss of signal intensity, which become major limiting factors for RNA structure determination<sup>21,81</sup>. As a result, the average size of RNA structures determined by NMR is 30 nt (ref. 36). Nucleotide-specific labeling strategies developed to study larger RNAs have been successfully used on a few RNAs up to 155 nt (refs. 82,83). However, the required quantities are also large and determination of the overall fold of large RNAs is often challenging<sup>81</sup>.

SAXS and AFM: Small-angle scattering determines the average shapes of RNAs in solution from the scattering events generated by either a beam of X-ray or neutron. The obtained electron density maps by SAXS and distribution of the atoms in the nucleus by small-angle neutron scattering can have a resolution range from 1 to 25 nm (refs. 84,85). AFM scans a stationary sample with a cantilever and an ultrasonic tip that reacts with the sample in tapping or contact mode, causing the Piezo element to move. Both methods can assess RNA samples at nanometer resolution and provide information on the overall shapes of RNAs, but the high-resolution details cannot be obtained as opposed to other structural biology methods.

In situ structure determination: while the abovementioned methods determine biomolecular structures *in vitro*, the emerging *in situ* cryo-EM SPA and cryo-electron tomography aided by focused ion beam milling have allowed near-atomic structure determination of biomolecular complexes under native cellular environment<sup>86</sup>.

However, *in situ* structure determination is currently limited to large biomolecules and complexes (>1 MDa) with high abundance inside cells. Moreover, accessibility to automated focused ion beam milling instruments necessary for the robust production of high-quality lamellae remains limited<sup>87,88</sup>.

## Limitations of the protocol

The current protocol aims to provide optimal conditions for cryo-EM analysis of RNAs that form 3D structures to perform their functions, and successful application of the protocol can also resolve RNA conformational changes. However, each RNA will probably require separate optimization because optimal condition for one RNA may not work for another. Moreover, there are RNAs that perform their functions without forming specific structural entities, e.g., most coding regions of mRNAs<sup>89,90</sup>, which may not be suitable for this protocol.

Extensive studies have reported remarkable methods for native RNA expression and purification. Alternative methods, instruments and software are also available for cryo-EM sample preparation, data collection, data processing and RNA modeling. Our protocol uses the most widely accessible instruments and shares most of its steps with the approaches of other research groups worldwide who determine protein-free RNA cryo-EM structures (Table 1). Other options are also discussed in the ‘Experimental design section’, but it is not practical to present detailed steps for all possible alternatives.

The resulting RNA cryo-EM structures are often resolved at moderate resolutions, which can hinder de novo modeling. Recent advances in RNA modeling algorithms allow generation of all-atom RNA models using cryo-EM density as restraints<sup>26,27,30,31,91</sup>. However, individual nucleotides and detailed tertiary interactions cannot be resolved at such resolution.

## Experimental design

### Obtain RNA secondary structure in advance

Although this protocol will not focus on secondary structure probing, it is an essential set of information to have at hand for the following two reasons: (i) RNAs with well-defined secondary structures are more likely to fold into rigid and homogeneous 3D structures and (ii) accurate secondary structure information is useful to facilitate map interpretation and model building, especially for cryo-EM reconstructions at moderate resolution. Several remarkable reviews have summarized recent advances in probing RNA secondary structure, including high-throughput analyses using dimethyl sulfate, selective 2'-hydroxyl acylation analyzed by primer extension (SHAPE) or other reagents, as well as advanced methods probing individual base-pairing via mutational profiling, structure proximity via cross-linking and alternative RNA structures via both experimental and computational approaches<sup>18,43,92–95</sup>.

### RNA IVT and purification (Steps 1–9)

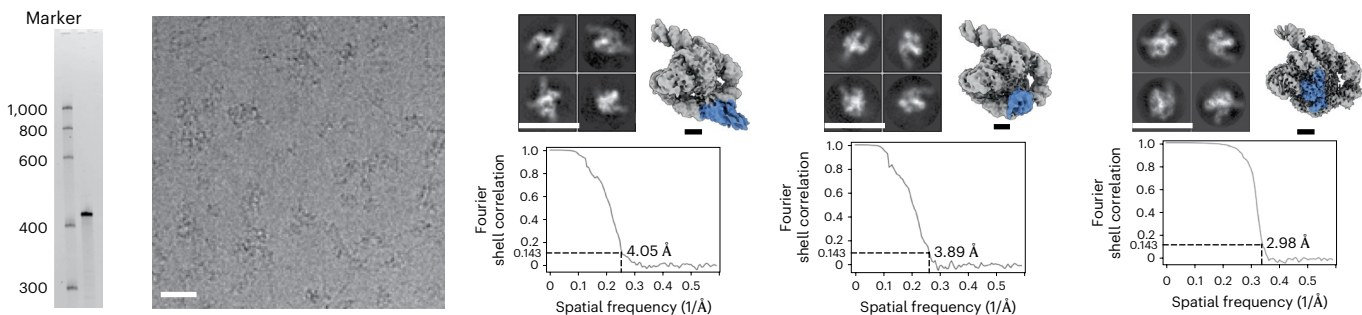
Linearized DNA templates are amplified with incorporations of hammerhead and hepatitis delta virus (HDV) ribozyme sequences at the 5' and 3' ends of the target RNA sequence for IVT product homogeneity<sup>49,96</sup>. In PCR reactions, 2'-methoxyl modified reverse primers can be alternatively used to ensure 3' end homogeneity<sup>50,97</sup> (Steps 1–4; Fig. 1a). The IVT products can be quickly checked by PAGE (Steps 5–7; Fig. 1b,c) and the cotranscriptionally folded RNAs can be purified after digestions of proteins and DNA templates<sup>42,43,53</sup> (Step 8A,B; Fig. 1d,e), which are ready for direct observations under cryo-EM. For example, the *Tetrahymena* group I intron and several RNA origami have been recently studied by cryo-EM directly after IVT and native purifications to reveal dynamics during RNA folding and catalysis<sup>14,33,98,99</sup> (Fig. 3a and Table 1).

In cases where the desired RNA conformation could not be obtained by cotranscriptionally folding (e.g., misfolded conformations)<sup>100,101</sup> or IVT generates too many byproducts mainly caused by early terminations, unwanted cleavage events and internal transcription initiations, large-scale purifications can be performed using denaturing PAGE followed by RNA refolding (Steps 8C–9; Fig. 1f). The low recovery rates by conventional gel soaking isolations are often ameliorated by electroelutions.

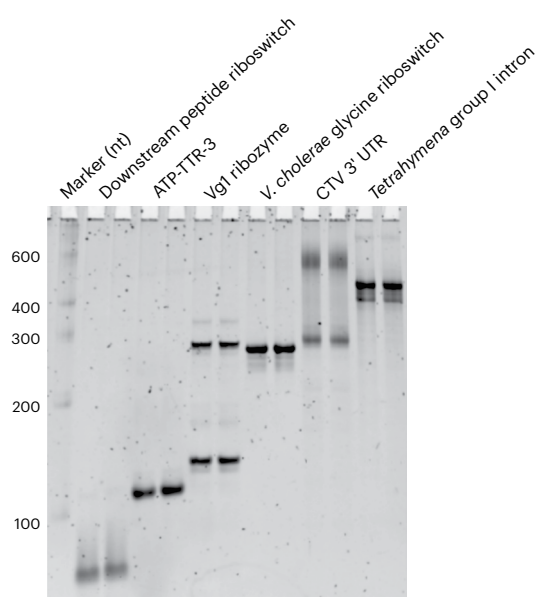
### RNA refolding condition screening (Steps 10–18)

Screening for refolding conditions includes initial screen of different heating/cooling strategies and buffer compositions, followed by expanded screening of pH ranges, ion concentrations and additives, aiming to obtain optimal refolding conditions in which RNAs fold into homogeneous conformations as examined by native PAGE (Steps 10–12; Fig. 1c,g and Tables 1 and 2). Although one band may not necessarily contain a single conformation<sup>102</sup>, multiple bands typically

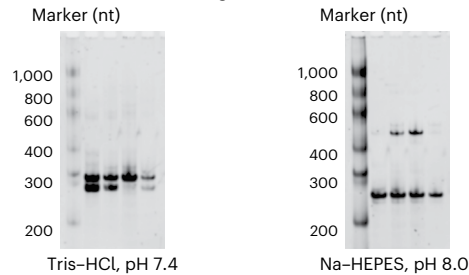
**a Cryo-EM 3D structures of cotranscriptionally folded *Tetrahymena* group I intron**



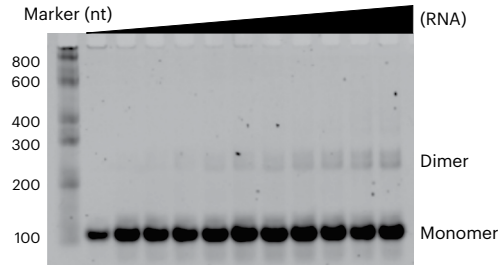
**b Different RNAs in the same refolding condition**



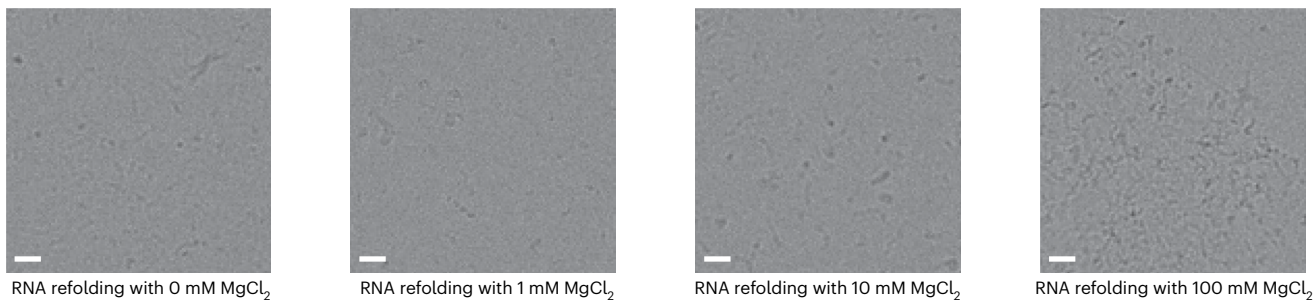
**c The CTV 3' UTR in different refolding conditions**



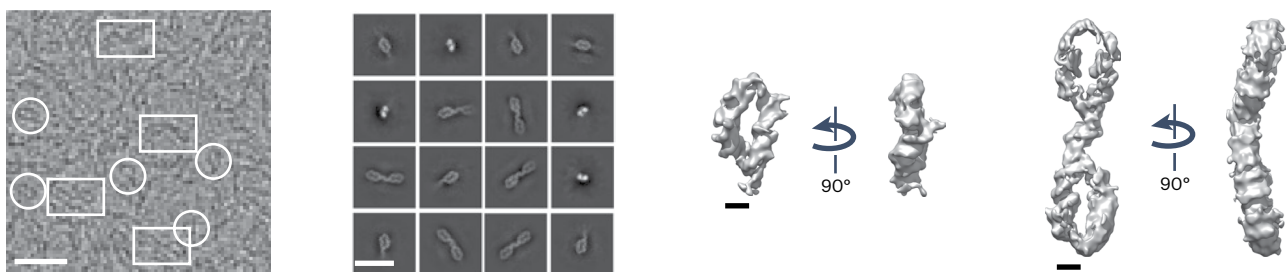
**d Increased ATP-TTR-3 oligomerizations with higher RNA concentrations**



**e High salt concentration induces ATP-TTR-3 aggregation**



**f ATP-TTR-3 monomeric and dimeric structures**



# Protocol

**Fig. 3 | Evaluations of different IVT and RNA folding conditions.** **a**, IVT of *Tetrahymena* group I intron under splicing inhibition condition reveals a single band in denaturing PAGE, while cryo-EM analysis of the cotranscriptionally folded RNA reveals three distinct conformations with the dynamic P1 helix (blue)<sup>14</sup>. **b–d**, Native PAGE of different RNAs folded under the same condition<sup>25,220,221</sup> (**b**), CTV 3' UTR folded under different conditions (**c**) and

ATP-TTR-3 oligomerization under increasing concentrations (**d**). **e**, ATP-TTR-3 particle distributions under different Mg<sup>2+</sup> concentrations visualized under cryo-EM. **f**, The ATP-TTR-3 can be solved in both monomer (white circles) and dimer (white boxes) in one specimen. White and black scale bars, 20 nm and 2 nm, respectively. The image in **a** was adapted from ref. 14, Springer Nature Limited.

correspond to multiple conformations. Smeared bands indicate RNAs with loosely organized structures or multiple dynamic conformations with the conformational exchange rate slower than electrophoretic mobility<sup>54</sup> (Fig. 3b).

While the majority of RNAs is denatured at 90 °C, GC-rich RNAs may require higher unfolding temperatures. Cooling strategies with different time periods, timepoints to add Mg<sup>2+</sup> ion and extended incubation times in different folding buffers will yield different states of the same RNA as shown in Fig. 3c. Increased RNA concentrations can induce oligomerizations of RNAs (Fig. 3d).

Relatively high RNA concentrations are often needed to have enough particles in the cryo-EM field of view, whereas oligomerization can be avoided by refolding at low RNA concentrations followed by centrifugation. While Mg<sup>2+</sup> is essential for proper RNA folding, a high Mg<sup>2+</sup> concentration may result in RNA oligomerizations and aggregations that lead to dramatically decreased monodispersed particles—lowering Mg<sup>2+</sup> concentration might ameliorate this problem (Fig. 3e and Extended Data Fig. 1). Oligomerization can also be beneficial (especially for smaller RNAs), because enlarged molecular size often helps particle picking and initial particle alignment (Fig. 3f).

NanoDLS measures the size of particles as well as their polydispersity by monitoring fluctuations in the intensity of scattered light as the particles undergo Brownian motion in solution. In case the existing IVT and RNA folding conditions could not yield homogeneous conformations, more variables such as different ions and additives can be systematically examined by nanoDLS at a higher throughput (Steps 13–18; Figs. 1h and 4). The optimized conditions can be used for SEC to further isolate distinct conformations and/or oligomeric states before subsequent vitrification and cryo-EM visualization<sup>44</sup>.

## RNA sample vitrification, cryo-EM visualization and data collection (Steps 19–28)

The optimal vitrified grid should have monodispersed particles randomly oriented in the thinnest ice possible, ideally just matching the largest dimension of the particle. An ice layer that is too thin could result in exclusion of the particles, particles with preferred orientations or ice breaking during imaging, whereas an ice layer that is too thick leads to multiple layers of particles and increased inelastic scattering that exacerbates the signal-to-noise ratio (SNR) and reconstruction resolution<sup>40,103–105</sup> (Steps 19–22; Fig. 5).

Major factors that affect vitrified sample quality include ice thickness, particle distribution, sample denaturation and particles adopting preferred orientation (Fig. 5). While the first two problems can be observed directly on cryo-EM micrographs (Figs. 1i,j and 5a–e), the latter two often require collection of a small test dataset and data processing until 2D classification and

**Table 2 | Refolding buffer and refolding condition list**

Refolding procedure A	Heat at 90 °C for 3 min, cool at room temperature for 10 min, add MgCl <sub>2</sub> , incubate at 50 °C for 20–30 min and at room temperature for 3–15 min
Refolding procedure B	Heat at 90 °C for 3 min, cool at room temperature for 10 min, add MgCl <sub>2</sub> , incubate at room temperature for 15 min
Refolding procedure C	Heat at 95 °C for 3 min, immediately insert the solution into ice and add MgCl <sub>2</sub>
Refolding procedure D	Heat at 80–90 °C for 1 min, add MgCl <sub>2</sub> and cool down at 23 °C for 15 min
Refolding procedure E	Heat at 95 °C for 3 min, reduce the temperature to 90 °C and keep for 30 s, decrease 1 °C per cycle and repeat 25 cycles to reach 65 °C, add MgCl <sub>2</sub> and keep at 65 °C for 30 s, decrease at 1 °C per cycle and repeat 45 cycles to reach 20 °C, hold at 4 °C
Refolding procedure F	Heat at 85 °C for 1 min, snap-cool on ice, add MgCl <sub>2</sub> and anneal from 70 °C to 50 °C for 6 min, then from 50 °C to 37 °C for 20 min, finally from 37 °C to 4 °C for 2 h
Refolding procedure G	Add MgCl <sub>2</sub> and incubate at room temperature for 15–30 min

# Protocol

Screening of different detergents in ATP-TTR-3 using nanoDLS (Steps 13–18) and cryo-EM (Steps 23–26)

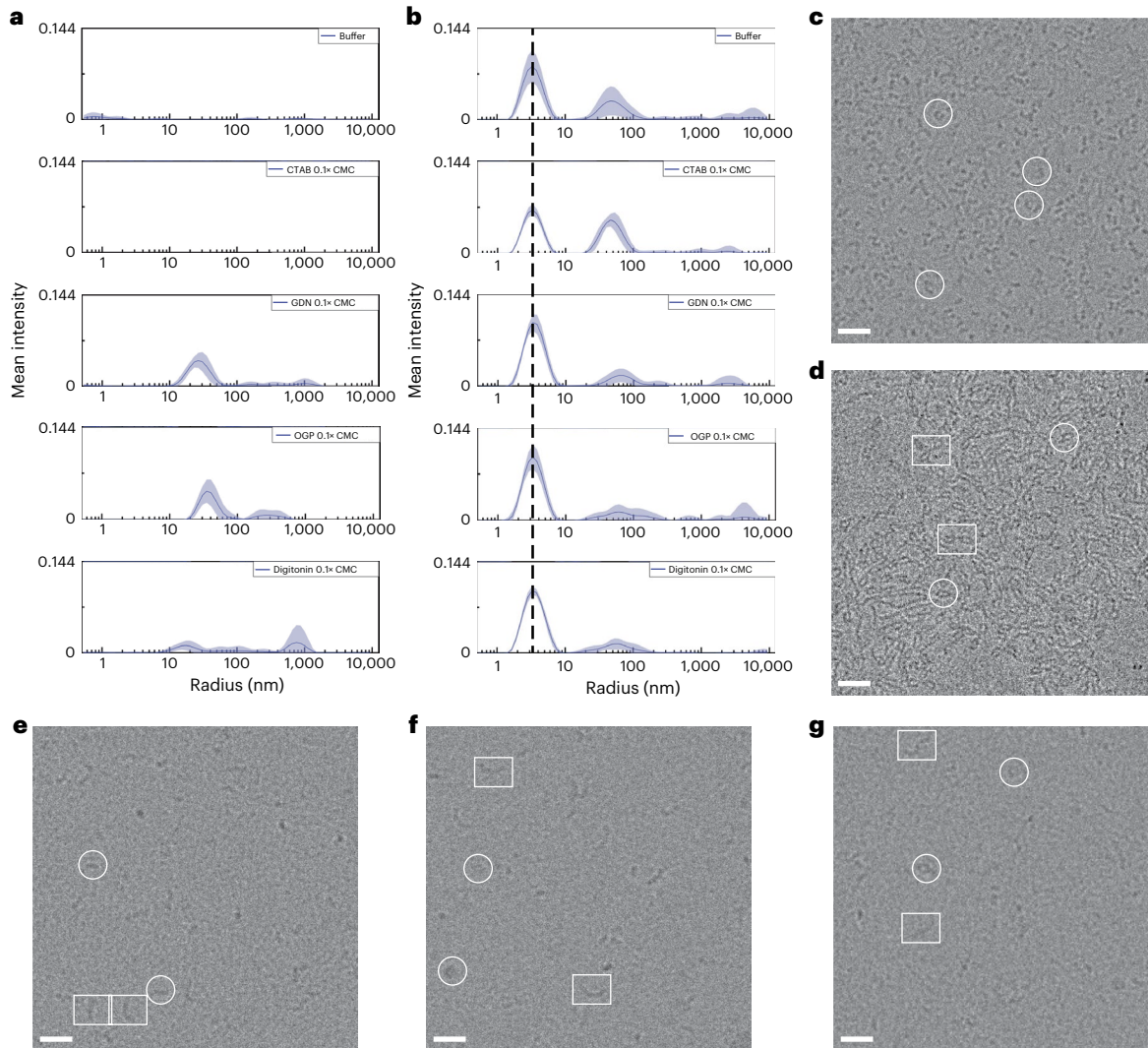


**Fig. 4 | Screening of different detergents in ATP-TTR-3 using nanoDLS and cryo-EM.** This figure relates to Steps 13–18 (for nanoDLS) and Steps 23–26 (for cryo-EM). **a**, The peak distribution of different detergents measured by nanoDLS. **b**, The peak distribution of ATP-TTR-3 with different detergents measured by nanoDLS. **c–g**, Cryo-EM micrographs of ATP-TTR-3 with RNA only

(c), hexadecyltrimethylammonium bromide (CTAB) (d), glyco-diosgenin (GDN) (e), octyl- $\beta$ -D-glucopyranoside (OGP) (f) and digitonin (g). The white circles indicate the ATP-TTR-3 monomer and white boxes indicate the ATP-TTR-3 dimer. White scale bars, 20 nm.

beyond (Figs. 2a–c and 5f,g). The addition of detergents to the samples as well as selection of different types of grids and support films (Tables 3–5), glow discharge/plasma cleaning devices and freezing apparatuses can be tested to circumvent the appearance of all the above-mentioned problems during sample vitrification.

Detergents added at concentrations notably below critical micelle concentration (CMC) have been previously shown to affect ice thickness and particle distribution<sup>106,107</sup> (Fig. 4c–g). Moreover, they can ameliorate preferred orientation and sample denaturation at the air–water interface<sup>106,108</sup>, which attracts and damages macromolecules during the process of plunge freezing<sup>109,110</sup>.

Various types of grids made of different grid and foil materials aside from the conventional copper grid with carbon foil have been suggested to minimize particle motion<sup>111–113</sup>, ice thickness, surface tension<sup>112</sup> and preferred orientation (Extended Data Fig. 2)<sup>113</sup>.

Adding support films can aid absorption of particles on the films and improve ice thickness and particle distribution. Meanwhile, the films can block air–water interfaces and absorb particles,

hence ameliorating preferred orientation and sample denaturation<sup>110</sup>. However, the most commonly used amorphous thin carbon film generates significant background noise that may not be suitable for small RNA samples and near-atomic resolution cryo-EM reconstruction<sup>114,115</sup>. Thinner support films such as graphene<sup>116–119</sup>, graphene oxide<sup>120,121</sup>, reduced graphene oxide<sup>122</sup>,

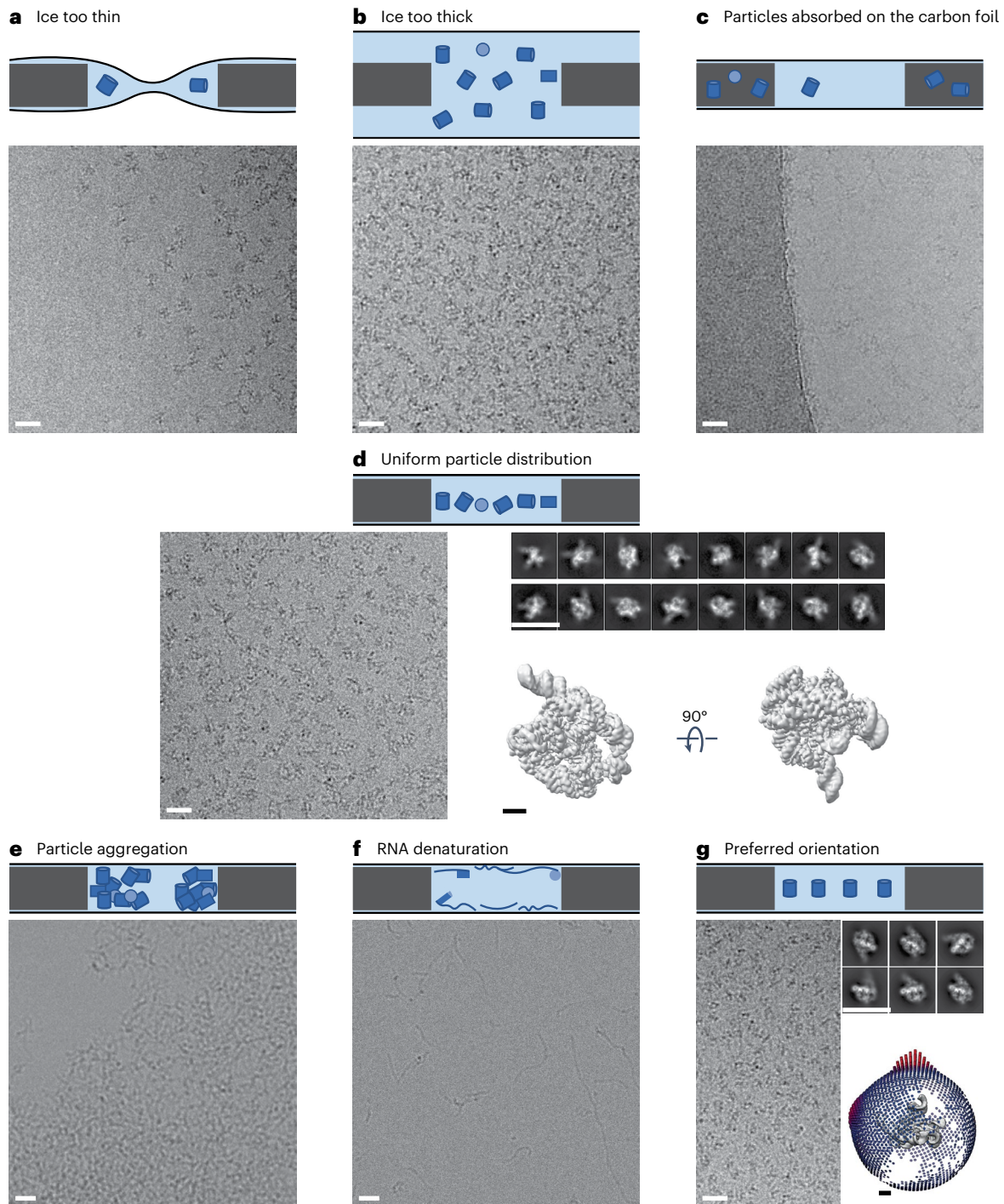


**Fig. 5 | Different sample freezing conditions of the *Tetrahymena* ribozyme visualized under cryo-EM.** **a**, Ice too thin. **b**, Ice too thick. **c**, RNA particles attaching to the carbon film of foil holes. **d**, Monodispersed RNA particles. **e**, RNA particle aggregation. **f**, RNA denaturation. **g**, The preferred orientation

as revealed by 2D averages and angular distributions (red columns show the preferred orientations). White and black scale bars, 20 nm and 2 nm, respectively. The image in **d** was adapted from ref. 14, Springer Nature Limited.

# Protocol

**Table 3 | Detergent list**

Type	Name	Catalog number
Ionic	Hexadecyltrimethylammonium bromide (CTAB)	Sigma-Aldrich, H6269
	Dodecyltrimethylammonium chloride (DTAC)	Sigma-Aldrich, 44242
Zwitterionic	CHAPS	Sigma-Aldrich, 75621-03-3
	CHAPSO	Sigma-Aldrich, 82473-24-3
Non-ionic	Octyl- $\beta$ -D-glucopyranoside (OGP)	Sigma-Aldrich, O8001
	Triton X-100	Solarbio, T8200
	Digitonin	MedChemExpress, HY-N4000
	Glyco-diosgenin (GDN)	MedChemExpress, HY-137179

2D crystals of streptavidin<sup>123,124</sup> and hydrophobin HFB<sup>125</sup> can be deposited on most types of grids to serve as alternatives. Lists of detergents, grids and support films are summarized in Tables 3–5.

Grids with or without support films are typically hydrophobic and require treatment with glow discharge or plasma cleaning devices. Devices generate residual air plasma are widely used (e.g., PELCO easiGlow and Tergeo-EM), mostly due to the low cost and simple operation, to remove surface contaminants and increase hydrophilicity that allow better spreading of the aqueous samples<sup>115</sup>. Alternative instruments can utilize specific combination of low-pressure gas mixtures such as argon–oxygen (e.g., Solarus)<sup>46</sup> or vaporized chemical substances such as pentylamine (GloQube)<sup>126</sup>. Caution should be taken for fragile support films such as graphene, as they can be damaged during the plasma cleaning process.

Vitrification preserves purified macromolecules under a near-native state by flash freezing a thin layer of solution to form amorphous ice<sup>127</sup>. Several manual and semi-automated freezing apparatuses that remove the excess aqueous samples by filter papers and plunging specimens into the cryogen (e.g., liquid ethane) are most commonly used, such as Vitrobot Mark IV (exemplified in this protocol), Leica EM GP2 and Gatan Cryoplunge 3. Alternative highly automated apparatuses have recently been developed to minimize manual handling and avoid

**Table 4 | Grid type list**

Brand	Mesh	Material	Type (hole diameter/hole distance in $\mu\text{m}$ )	Catalog number
Quantifoil	200	Cu	R1.2/1.3	Q250CR1.3
			R2/1	Q250CR1
			R2/2	Q250CR2
			R3.5/1	Q225CR35
		Au	R1.2/1.3	Q2100AR1.3
			R2/1	Q250AR1
	300	Cu	R1.2/1.3	Q350CR1.3
			R2/1	Q350CR1
		Au	R1.2/1.3	Q3100AR1.3
			R2/1	Q350AR1
			UltrAuFoil R1.2/1.3	Q350AR13A
Electron Microscopy Sciences	400	Cu	R1.2/1.3	Q450CR1.3
			R2/1	Q450CR1
		Au	R1.2/1.3	Q4100AR1.3
			R2/1	Q450AR1
	300	Au	C-flat R1.2/1.3	CF313-50-Au
			Au-flat R1.2/1.3	AUFT313-50
		Cu	C-flat R1.2/1.3	CF413-50
			C-flat R1.2/1.3	CF413-50-Au
Nanodim	300	Au	ANTcryo R1.2/1.3	M01-Au300-1.2/1.3

**Table 5 | Support film list**

Material	References
Graphene	116–118,216
Graphene oxide	120–122,217,218
Ultrathin carbon	114
2D crystals of streptavidin and hydrophobin HFBI	123–125
Holey ceramic	219

filter paper blotting using inkjet dispensing<sup>128</sup>, spraying<sup>129–131</sup>, pin printing<sup>132</sup>, microcapillary writing<sup>133</sup> or tube suction<sup>134</sup>.

The vitrified grids are loaded into the microscope for cryo-EM visualization (Steps 23–26; Fig. 1j). Proper ice thickness is essential to obtain high-resolution cryo-EM data; however, all the above-mentioned vitrification methods produce variable ice thickness even within individual holes of the same square on the grid<sup>135</sup> (Extended Data Fig. 3). It is thus critical to screen for areas with optimal ice thickness before semi-automated data collection can be performed (Steps 27–28; Fig. 2a). Methods commonly used to measure ice thickness include tomography<sup>105</sup>, additional imaging techniques coupled with machine/deep learning<sup>136–139</sup> and on-the-fly methods using energy filter or objective aperture<sup>135,140–143</sup>, some of which can be integrated in the most commonly used automated data collection schemes such as E Pluribus Unum (EPU)<sup>142</sup>, SerialEM<sup>144</sup> and Leginon<sup>145</sup>.

### Data processing to resolve RNA heterogeneity (Steps 29–50)

Recent development of automated on-the-fly data processing software has allowed instantaneous assessment of cryo-EM SPA data quality with minimal user/human input that can maximize instrument efficiency and productivity<sup>146</sup>. Extensive data processing is normally carried out afterward so that flexible regions, dynamic conformational changes and compositional heterogeneity of the specimen associated to functions may be resolved with improved resolution. In addition to the standard data processing pipeline<sup>147</sup> (Steps 29–41; Fig. 2b–e), integration of deep learning algorithms has facilitated improved picking of particles with low contrast<sup>148–155</sup> (Fig. 6) and classification of continuous conformations that could project motion pathways related to functions<sup>156–162</sup>. These features are useful to resolve RNA dynamics and heterogeneity (Fig. 7). The data processing protocol is exemplified using commonly used software suites EMAN2<sup>163</sup>, Relion<sup>164</sup> and cryoSPARC<sup>165</sup> (Steps 42–50; Fig. 2f), whereas the processing time of Relion and cryoSPARC using the indicated computational resources on the *Tetrahymena* group I intron data is summarized in Table 6.

### RNA modeling into cryo-EM density (Steps 51–81)

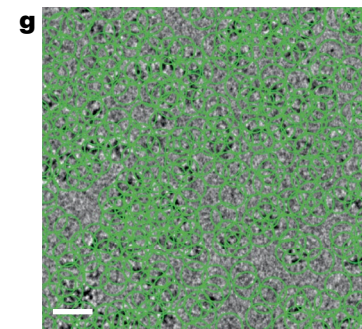
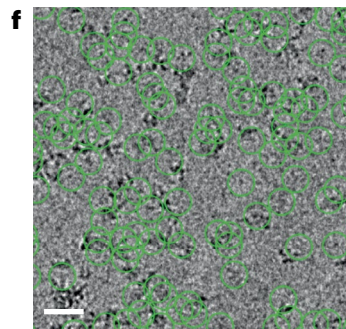
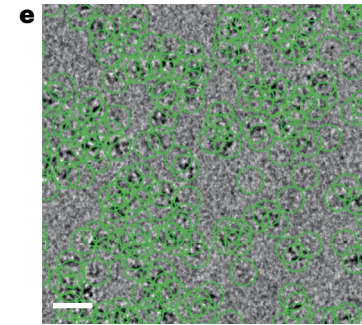
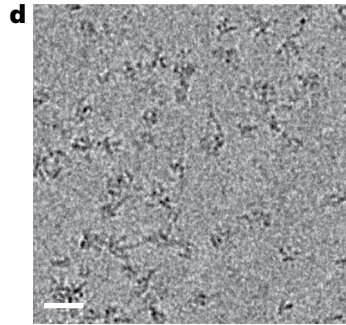
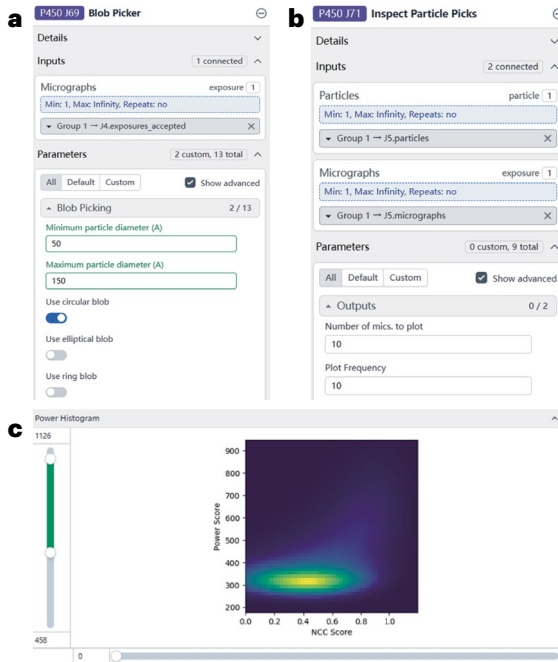
Interpretation of cryo-EM density into atomic models has been traditionally labor intensive and requires expertise and extensive experience<sup>166,167</sup>. Models are generally built with confidence when the cryo-EM reconstruction reaches 3 Å resolution or better, whereas the level of confidence reduces as the resolution degrades close to 4 Å or worse, often resulting in more errors in the models<sup>168,169</sup>.

Although some RNA cryo-EM structures have achieved the overall resolution of 3 Å and better, flexible regions in these structures were often resolved at worse resolution. Moreover, most RNAs remained in the moderate resolution range<sup>23</sup> (Table 1). Although several methods have been developed for automated RNA modeling into cryo-EM density<sup>25,26,30,91,170</sup>, intensive manual interventions coupled with RNA structure predictions and subsequent refinements are still routinely required<sup>171–174</sup>.

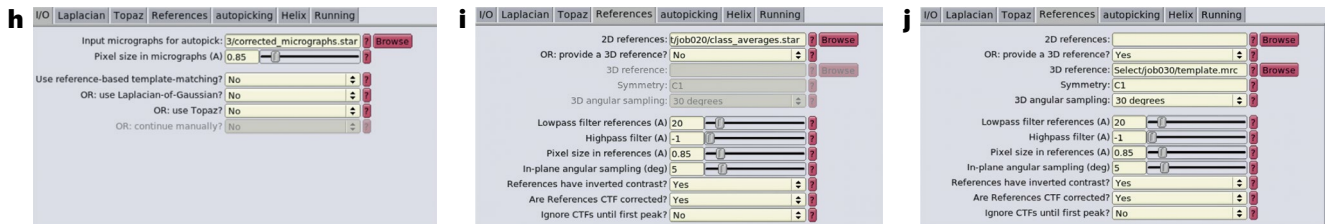
Here, we present a general protocol that starts with docking of the homologous models (Steps 51–59; Fig. 8), followed by manual curations and de novo modeling (Steps 60–69; Fig. 9), which can be assisted by structure prediction and automated modeling algorithms (Steps 70–71). The final models are subjected to refinements and validations (Steps 72–81; Fig. 10), then deposited into the public databases.

# Protocol

## Blob picker in cryoSPARC (Step 31A)



## Reference-based template matching in Relion (Step 31B)



## Reference-based CNN particle picking in EMAN2 (Step 31C)

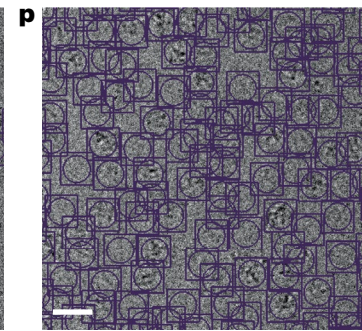
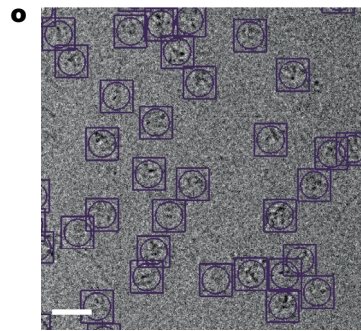
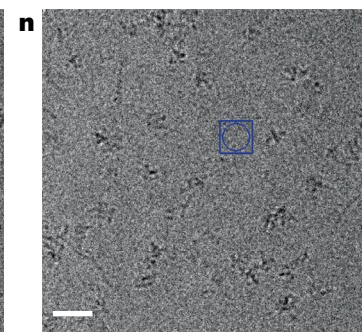
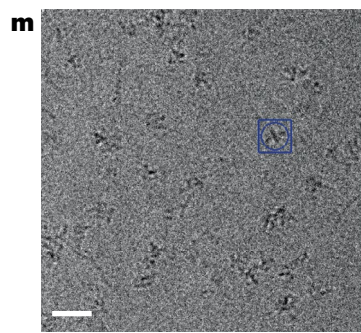


**Fig. 6 | Different methods for cryo-EM SPA particle picking.** This figure relates to Step 31. **a**, GUI of ‘Blob Picker’ job in cryoSPARC. **b**, GUI of ‘Inspect Particles Picks’ in cryoSPARC. **c**, GUI of ‘Power Histogram’ in ‘Inspect Particles Picks’ where the threshold values can be changed to adjust particle picking results. **d**, Representative micrograph. **e–g**, Particle picking results of the proper threshold (**e**), a too-narrow threshold range (**f**) and a too-wide threshold range (**g**) (Step 31A).

**h**, GUI of ‘Reference-based template matching’ in Relion. **i**, GUI of ‘2D references’ import. **j**, GUI of ‘3D references’ import (Step 31B). **k**, GUI of EMAN2 project manager. **l**, GUI of ‘Interactive Particle Picking’. **m**, Representative good reference. **n**, Representative background reference. **o,p**, Number of particles picked under high (**o**) and low (**p**) threshold values (Step 31C). White scale bars, 20 nm.

## Materials

### Biological materials

- The plasmid consists of a vector with the target RNA sequence. Usually this is downstream of a T7 promoter sequence and upstream of a single restriction endonuclease cleavage site. In addition, hammerhead and HDV ribozymes can be added at the 5' and 3' ends of the target RNA sequence to obtain a homogeneous RNA product. In this protocol, we use the pUC19 vector with resistance to ampicillin, which can be commercially synthesized by Integrated DNA Technologies, Sangon Biotech and other sources. The sequences of *Tetrahymena* group I intron, citrus tristeza virus (CTV) 3' untranslated region (UTR), *Vibrio cholerae* glycine riboswitch, Vg1 ribozyme, downstream peptide riboswitch and ATP-TTR-3 with hammerhead and HDV ribozymes at the 5' and 3' ends, the corresponding forward and reverse primers of two target RNAs are summarized in Table 7

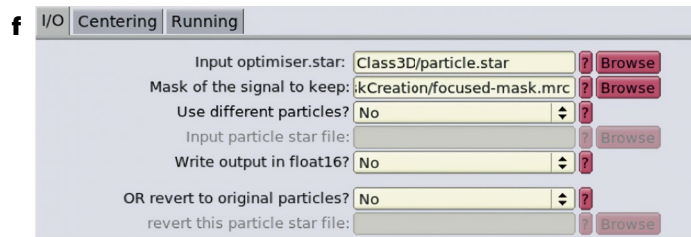
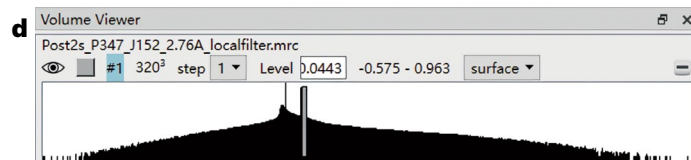
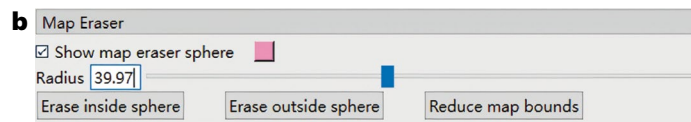
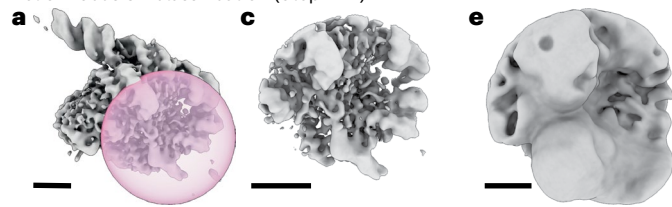
### Reagents

**▲ CRITICAL** All experimental procedures should be performed under RNase-free conditions. Wearing masks and treat the experiment area with RNase inhibitor can help avoid RNase contaminations of the reagents.

- 2× Phanta max master mix (Dye plus) (Vazyme, cat. no. P252-03)
- Acetic acid (Sangon Biotech, cat. no. A501931)  
**▲ CAUTION** This reagent is flammable. Avoid contact as it may cause severe skin burns and eye damage.
- Acrylamide/bis-acrylamide (Acryl/Bis) 30% solution (29:1) (Sangon Biotech, cat. no. B546017-0500)  
**▲ CAUTION** This reagent is toxic when swallowed. Long-term contact is harmful to the skin and organs and may cause cancer. Avoid mouth and skin contact.
- Agar (Sigma-Aldrich, cat. no. A1296)
- Agarose (Sangon Biotech, cat. no. A620014)
- Ammonium persulfate (APS; MACKLIN, cat. no. A6295)  
**▲ CAUTION** This reagent is toxic if swallowed and harmful to the eyes and skin if contacted.
- Ampicillin sodium salt (Sigma-Aldrich, cat. no. A0166)
- Boric acid (Sangon Biotech, cat. no. A610044)
- Bromophenol blue (Sangon Biotech, cat. no. A602230)  
**▲ CAUTION** This reagent is harmful to the eyes and skin if contacted or inhaled, and should be used in a well-ventilated environment.
- Coomassie brilliant blue G-250 (Sangon Biotech, cat. no. A100615)
- D2000 (Tiangen, cat. no. 4992949)
- Diethyl pyrocarbonate (DEPC; Sigma-Aldrich, cat. no. D5758)  
**▲ CAUTION** This reagent is harmful to the eyes, respiratory system and skin if swallowed or contacted. It should be used in fume hoods.
- Dithiothreitol (DTT; Thermo Fisher Scientific, cat. no. R0861)  
**▲ CAUTION** This reagent can irritate skin, eyes and respiratory tract if contacted.
- DNA marker I (Tiangen, cat. no. 4992935)
- DNA marker III (Tiangen, cat. no. 4992939)
- DNase I (RNase-free) (New England BioLabs, cat. no. M0303L)

# Protocol

## Relion focus 3D classification (Step 42A)



## CryoSPARC 3DVA and display (Step 42B)

**j** P450 J73 3D Variability

Inputs 2 connected

Particle stacks particle [1]

Min: 1, Max: Infinity, Repeats: no

Group 1 → J16.particles

Mask mask [1]

Min: 1, Max: 1, Repeats: no

Group 1 → J16.mask

Parameters 1 custom, 16 total

All Default Custom  Show advanced

Particle preprocessing 0 / 3

Window dataset (real-space)

Window inner radius 0.85

Window outer radius 0.99

3D Variability 1 / 11

Number of modes to solve 3

Symmetry C1

Only use this many particles Not set

Filter resolution (A) 4

**k** P450 J74 3D Variability Display

Inputs 2 connected

Particle stacks particle [1]

Min: 1, Max: Infinity, Repeats: no

Group 1 → J18.particles

Components volume [1]

Min: 1, Max: 1, Repeats: no

Group 1 → J18.volume

Parameters 2 custom, 22 total

All Default Custom  Show advanced

Particle preprocessing 0 / 3

Window dataset (real-space)

Window inner radius 0.85

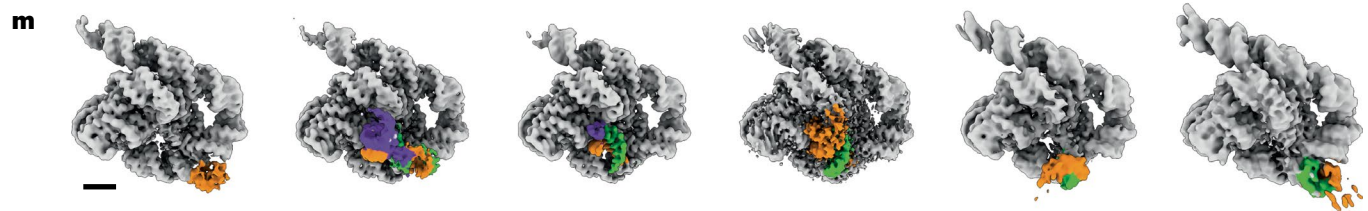
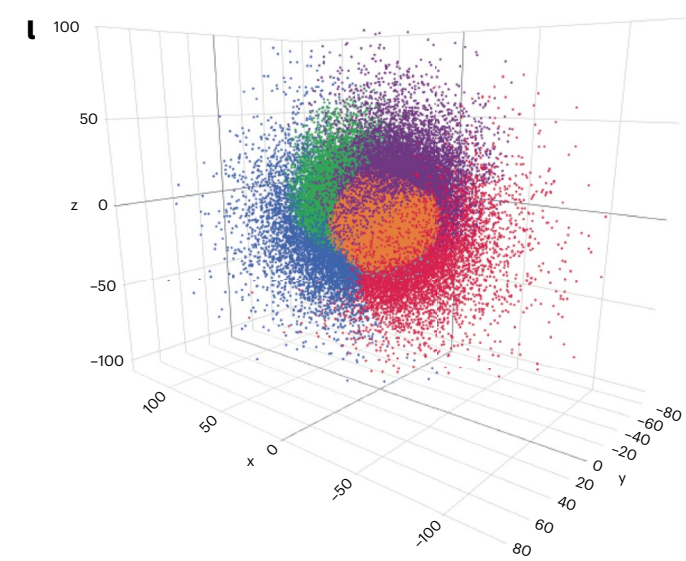
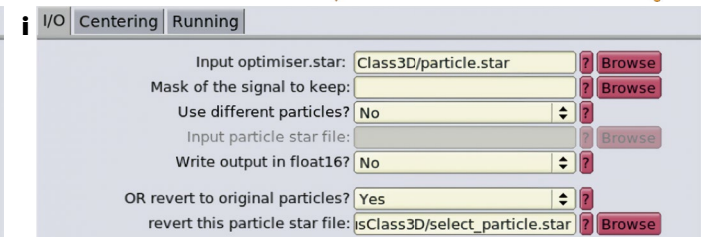
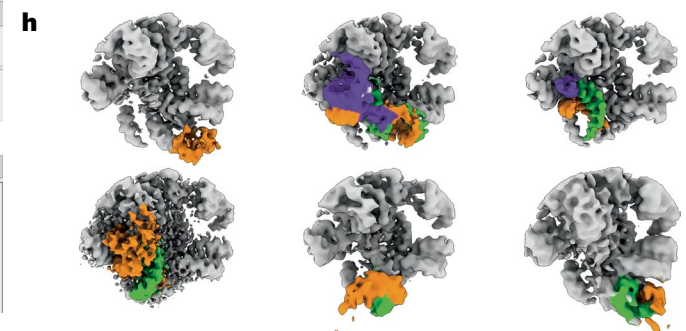
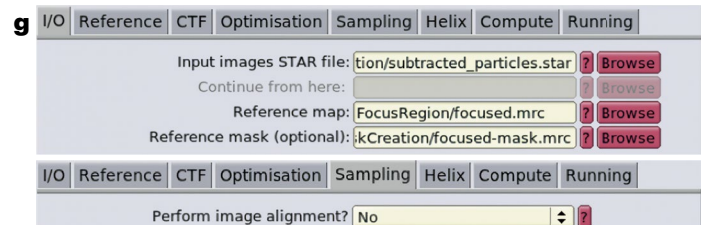
Window outer radius 0.99

3D Variability Output 2 / 17

Output mode cluster

Number of frames/clusters 6

Min/Max Range Percentile (%) 3



# Protocol

**Fig. 7 | Cryo-EM workflow to reveal RNA heterogeneity in Relion and cryoSPARC.** This figure relates to Step 42. **a**, A pink sphere covering the focused flexible region in the RNA cryo-EM map. **b**, ‘Map Eraser’ GUI to adjust the ‘Radius’ of the pink sphere region to be erased from the cryo-EM map. **c**, The focused flexible region extracted from the cryo-EM map using volume subtraction. **d**, GUI showing the threshold ‘Level’ to generate a mask of the focused region. **e**, The generated mask of the focused region. **f–i, m**, The workflow of focused

3D classification including ‘particle subtraction’ (**f**), focused classification without particle alignment (**g**), visualization of classification result (**h**) and revert subtracted particles to original particles (**i**) for 3D refinement and visualization (**m**) (Step 42A). **j**, GUI of 3DVA job in cryoSPARC. **k**, GUI of 3DVA Display in cryoSPARC (Step 42B). **l**, 3D visualization of clustered particles. Black scale bar, 2 nm. The image in **m** was adapted from ref. 14, Springer Nature Limited.

- *Escherichia coli* DH5 $\alpha$  competent cells (TIANGEN, cat. no. CB101)
- Ethylenediaminetetraacetic acid (EDTA) disodium salt (Sangon Biotech, cat. no. A610185)  
▲ CAUTION This reagent is toxic if swallowed and harmful to the eyes, respiratory system and skin if contacted. It should be used in fume hoods.
- Ethane gas  
▲ CAUTION Ethane is a flammable gas that can explode when mixed with air. No open flame is allowed in the sample preparation room. All valves of the ethane gas tank must be closed after use.
- Ethanol absolute (Sangon Biotech, cat. no. A500737)  
▲ CAUTION Flammable and absorbs moisture after prolonged storage.
- E.Z.N.A. gel extraction kit (Omega Bio-tek, cat. no. D2500-02)
- E.Z.N.A. plasmid DNA mini kit I (Omega Bio-tek, cat. no. D6943-02)
- FastDigest EcoRI (Thermo Fisher Scientific, cat. no. FD0275)
- FastDigest HindIII (Thermo Fisher Scientific, cat. no. FD0504)
- FastDigest NdeI (Thermo Fisher Scientific, cat. no. FD0583)
- Glycerol (Sangon Biotech, cat. no. A501745)
- HEPES, free acid (Sangon Biotech, cat. no. A600264)
- HiScribe T7 high yield RNA synthesis kit (New England BioLabs, cat. no. E2040S)
- Hydrochloric acid (HCl; Aladdin, cat. no. H399890)  
▲ CAUTION This reagent is harmful to the respiratory system and skin if inhaled or contacted. It should be used in fume hoods.
- Isopropanol (Sangon Biotech, cat. no. A507048)  
▲ CAUTION This reagent is highly flammable. It can lead to serious eye damage and may result in dizziness if contacted or inhaled.

**Table 6 | Data processing using Relion and cryoSPARC**

Stage	Relion 4.0	CryoSPARC 4.4.1
	Timing (h)	
Motion correction	1.3	1
CTF estimation	4	1.2
Particle picking	4	0.6
Particle extraction	1.6	0.2
2D classification	46	2.6
Initial model creation	3	1
3D classification	4	1.6
Refinement (each class)	1	0.3
Heterogeneity determination	3	1.6
Refinement	0.3	0.3
CTF refinement	0.2	0.2
Polish/reference-based motion correction	3	9.5
Final refinement	0.3	0.2
Local resolution estimation	0.1	0.1

Timing is calculated using a dataset of 5,185 movie stacks with 1,600,000 initial particles (256 pixels) processed on a workstation with a 40 core Intel CPU and 8 Nvidia RTX2080Ti GPUs or equivalent.

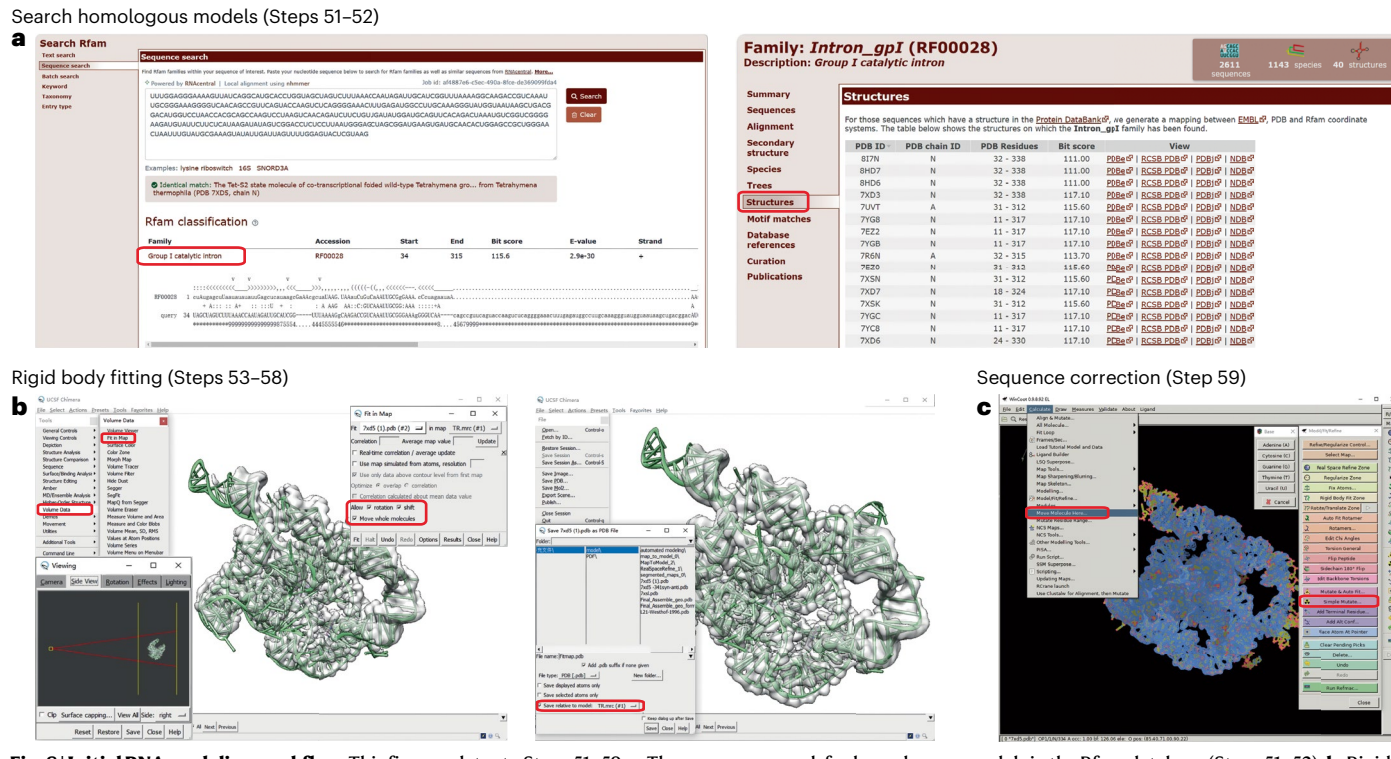


**Fig. 8 | Initial RNA modeling workflow.** This figure relates to Steps 51–59. **a**, The sequence search for homologous models in the Rfam database (Steps 51–52). **b**, Rigid body fitting of the model into the cryo-EM map in Chimera (Steps 53–58). **c**, Sequence correction in Coot (Step 59).

- Lauryl maltose neopentyl glycol (LMNG; MedChemExpress, cat. no. HY-138193)
- Liquid nitrogen  
▲ **CAUTION** Ensure adequate ventilation to avoid asphyxiation. This reagent can cause frostbite after extended contact.
- Magnesium chloride hexahydrate ( $MgCl_2 \cdot 6H_2O$ ; Sangon Biotech, cat. no. A610328)
- Milli-Q water (ultrapure water,  $18.2\text{ M}\Omega/\text{cm}$  at  $25^\circ\text{C}$ )
- *N,N,N,N-Tetramethylethylenediamine* (TEMED; MACKLIN, cat. no. T6023)  
▲ **CAUTION** This reagent may cause serious damage to the eyes, skin and organs if contacted or swallowed. It should be used in a well-ventilated environment.
- Nucleotide triphosphate (NTP) set solution (Sangon Biotech, cat. no. B600059)
- Phusion green hot start II high-fidelity PCR master mix (Thermo Fisher Scientific, cat. no. F566L)
- Potassium chloride (KCl; Sangon Biotech, cat. no. A501159)
- Potassium hydroxide (KOH; Sangon Biotech, cat. no. A610441)  
▲ **CAUTION** This reagent is harmful to the eyes and skin if swallowed or contacted.
- Prometheus High-Sensitivity Capillaries (NanoTemper Technologies, cat. no. PR-C006)
- Proteinase K (Thermo Fisher Scientific, cat. no. EO0491)
- Pyrophosphatase, inorganic (Thermo Fisher Scientific, cat. no. EF0221)
- RiboLock RNase inhibitor (Thermo Fisher Scientific, cat. no. EO0384)
- RiboRuler low range RNA ladder, rtu (Thermo Fisher Scientific, cat. no. SM1833)
- RNaseZap RNase decontamination solution (Invitrogen, cat. no. AM9782)
- Sodium acetate anhydride (Sangon Biotech, cat. no. A500827)
- Sodium chloride (NaCl; Sangon Biotech, cat. no. A501218)
- Sodium hydroxide (NaOH; Sangon Biotech, cat. no. A100583)  
▲ **CAUTION** This reagent may cause eye damage and severe skin burns if contacted.

## RNA structure prediction (Step 61)

**a**

SimRNAweb2.0

Model your RNA

Job Title: Job Name: [placeholder] E-mail: email@example.com [placeholder]

Input for Stimulation

Basic Inputs

Input: Sequence: [placeholder] Secondary Structure: [placeholder] Hard secondary structure restricts: [placeholder]

Advanced Options [button]

What do you want to predict? [dropdown: RNA, RNA-DNA]

Left: [button], Right: [button]

FARFAR2

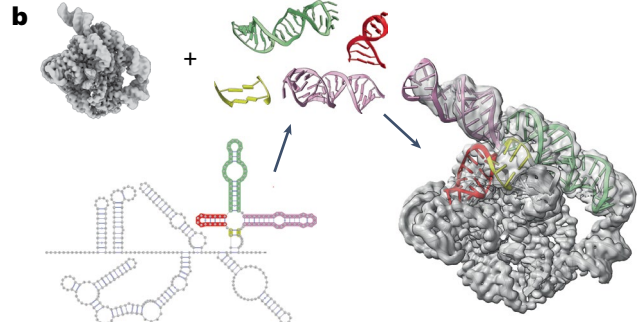
Welcome to ROSIE

Submit a new FARFAR2 job

RNA Composer

Welcome to RNAComposer, a fully automated RNA structure modeling server.

## Manual de novo model building (Steps 62–66)



## Manual inspection of every single residue in Coot (Steps 67–69)

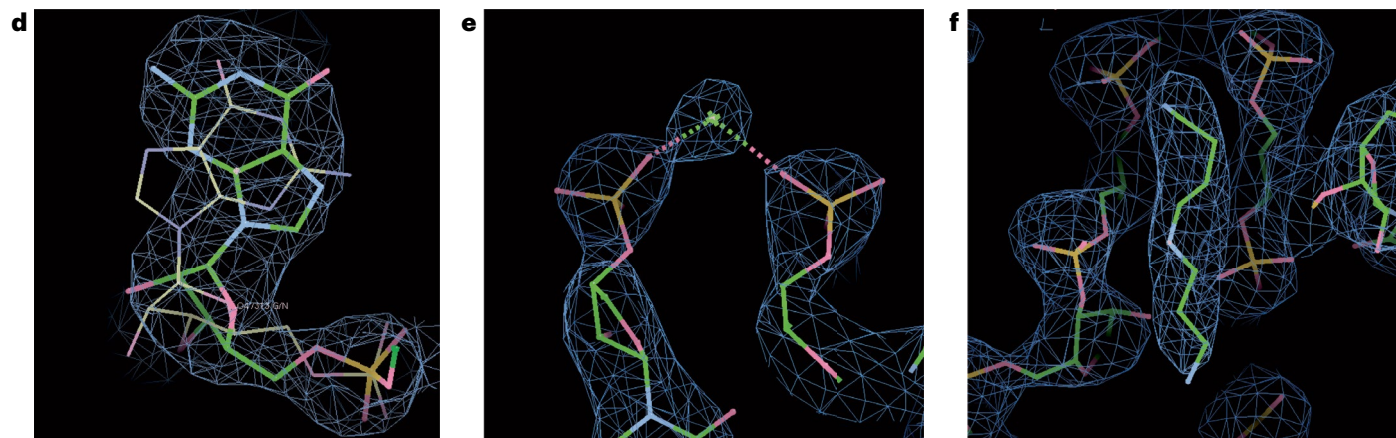
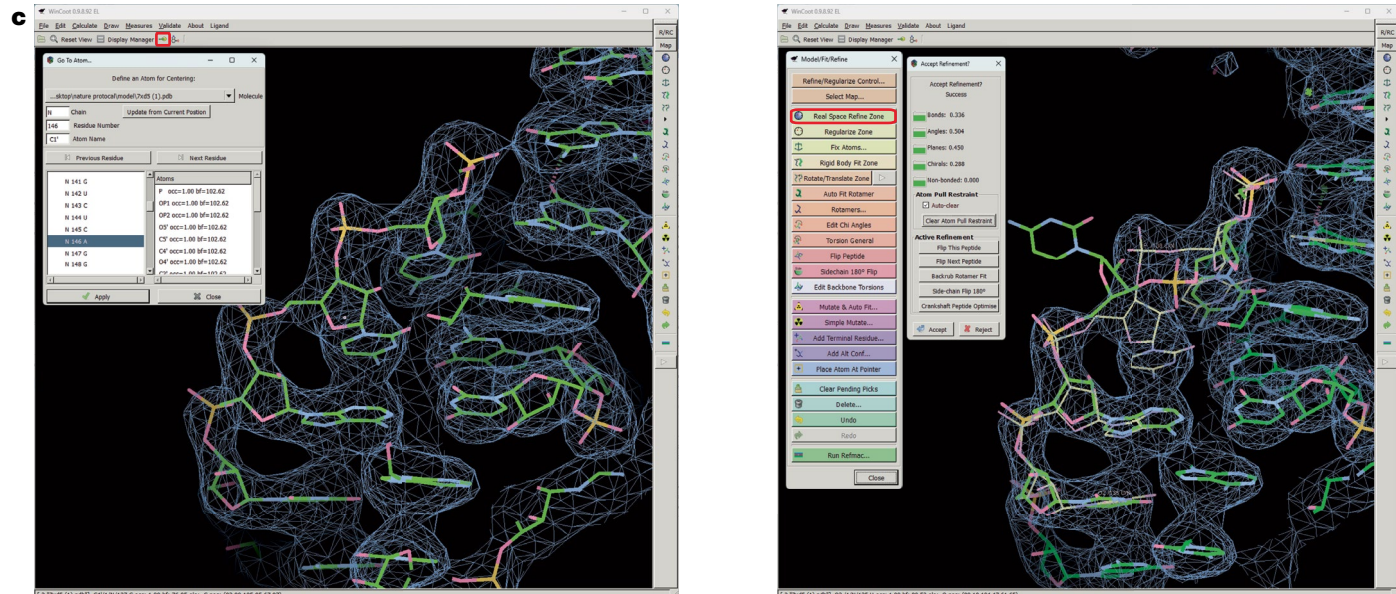


**Fig. 9 | Manual RNA modeling and inspection.** This figure relates to Steps 61–69. **a**, Representative RNA structure prediction methods and websites (Step 61). **b**, Manual de novo RNA modeling assisted by structure prediction. A four-way junction (consisting of red, green, pink and yellow stems) was chosen as the starting point for the de novo RNA modeling and each stem was separately

predicted using software such as RNAComposer based on secondary structures and fitted into the cryo-EM density map in Chimera (Steps 62–66). **c**, Manual inspection and correction of each residue in Coot. **d**, Comparison of *syn* and *anti* conformations of the N-glycosidic bond. **e**, Metal ion coordination with phosphate oxygens. **f**, Spermidine in the cryo-EM density (Steps 67–69).

# Protocol

## Model refinement in Phenix (Steps 72–79)

**a**

**b**

**c**

**d**

**e**

## MolProbity validation (Step 80)

**f**

**Analysis output: all-atom contacts and geometry for 7xd5FH.pdb**

**Duke Biochemistry**  
Duke University School of Medicine

**Summary statistics**

All-Atom Contacts	Clashscore, all atoms: 0.61	100 <sup>th</sup> percentile: (N=136, 2.84 Å ± 0.25 Å)
Nucleic Acid Geometry	Bad bonds: 0 / 9718 (0.0%)	Goal: 0%
Additional validations	Bad angles: 0 / 15138 (0.0%)	Goal: <0.1%
Charal volume outliers: 0 / 2030 (0.0%)		
Waters with clashes: 0 / 0 (0.0%)		

In two column results, the left column gives the raw count, right column gives the percentage.  
A green percentile is the best among structures of comparable resolution; a red percentile is the worst. For clashscore the comparative set of structures was selected in 2004, for MolProbity score in 2009.  
Key to table colors and cutoffs here.

**Multi-criterion visualizations**

- Multi-criterion kinemage
- Multi-criterion chart
- UnDowser

View in KING | View in NGL | Download (2.8 Mb)

**Single-criterion visualizations**

- Clash list (503 bytes): View
- Charal volume report (790 bytes): View

Continue >

**Fig. 10 | Refinement and validation of the RNA model.** This figure relates to Steps 72–81. **a**, Refinement settings in Phenix.real\_space\_refine. **b**, Automated detection of the secondary structures via ‘Find Secondary Structure’ button in ‘Selection Editor’ and the output.eff file (left and middle). Open the.eff file in text editor and manually correct the RNA secondary structure restraints (right).

## RCSB-PDB validation (Step 81)

**g**

**Download validation reports**

The status of the validation calculation is: **finished**

NOTE: Preliminary validation report produced by the OneDep Deposition System is not a proof of deposition and should not be submitted to journals. More information about the types of wwPDB validation reports can be found [here](#).

**Validation report:**

- D\_1300049533\_val-report-full\_P1.pdf|V10 (Wed Jul 24 14:34:28 2024)

**XML file:**

- D\_1300049533\_val-data\_P1.xml|V10 (Wed Jul 24 14:34:28 2024)

**Validation mmCIF file:**

- D\_1300049533\_val-data\_P1.cif|V10 (Wed Jul 24 14:34:28 2024)

**Overall quality at a glance:**

Metric	Percentile Ranks	Value
Clashscore	Worse	1
RNA backbone	Percentile relative to all structures	0.44
	Percentile relative to all EM structures	

**c**, Load the complete.eff file in Phenix and refine the model. **d**, Check the validation report and open the refined model in Coot. **e**, Curate model violations using the ‘Regularize Zone’ in Coot (Steps 72–79). **f**, MolProbity validation (Step 80). **g**, Validation in the Research Collaboratory for Structural Bioinformatics Protein Data Bank (RCSB-PDB; Step 81).

- Spermidine (Lablead, cat. no. S0266)
 

⚠ CAUTION This reagent may cause eye damage and severe skin burns if contacted.
- SYBR Gold (Invitrogen, cat. no. S11494)
- T7 RNA polymerase (in-house prepared; it can also be obtained commercially from various suppliers, e.g., New England Biolabs, cat. no. M0251S)

# Protocol

**Table 7 | Sequences and primers of RNA**

Name	Sequence
Tetrahymena group I intron	5'-GGGUAAAACGGCGGGAGUAACUAUGACUCUAAAUGCAAUUUACCUUUGGAGGGAAAGUUAUCA GGCAUGCACCUGGUAGCUAGCUUUAAAACCAAUAGAUUGCAUCGGUUAAAAGGAAGACCGGUAAAUG CCGGAAAGGGGUCAACAGCGGUUCAGUACCAAGUCUCAGGGAAACUUUGAGAUGGCCUUGCAAAGGGU AUGGUAAAAGCUGACGGACAUGGUCCUACCCACGCAGCCAAGUCCUAGUCAACAGAACUUCUGUUGAU AUGGAUGCAGUUACAGACUAAUGUCGGUCGGGAAGAUGUAUUCUUCUCAUAAGAUUAUGUCGGACCU CUCCUAAAUGGGACCUAGCGGAUGAAGUGAUGCCACACUGGACCGCUGGGAAACUAAUJUGUAUGCGAAA GUAAUUGAUUAGGUAGUACUGUAAGGUAGCCAAAUGGCCUUCGUCAUCUAAU-3'
Tetrahymena group I intron forward primer	5'-AAGCTTAAATCGACTCACTATAGGTAAACGGCGGGAGTAAC-3'
Tetrahymena group I intron reverse primer	5'-i2OMeA//i2OMeA//TTAGATGACGAGGCATTGGCTAC-3'
<b>Hammerhead ribozyme–ATP-TTR-3–HDV ribozyme</b>	5'- <b>GGGUACCGGAUGCUGACGAGUCUCUGAGAUGAGACGAAACUCUUCGCAAGAAGAGUCCAUCCG GUAUCCCCGGCAUAGGCAUGGAUCAGCUAAGGAACUGUAAUCGGGCAACGACUAGGAA CUAGUCGUUGGGAAAGAACUCCGCAUAAUCGGGAGUUCUUGAGCGGGAGAUCCAUGCCUAAGUCGC GCCGCCAUGGGUCCCAGCCCUCCUCGCUUGCGCCGGGUGGGCAACAUUCGAGGGGACCGUCCC CUCGGUAUGGCAGAUGGGAC-3'</b>
Hammerhead ribozyme forward primer	5'-TAATACGACTCACTATAGGTAAACGGATGCTG-3'
HDV ribozyme reverse primer	5'-GTCCTTACCGCATTACCGA-3'
CTV 3' UTR	5'-UUGAAGUGGACGGAUAAGUUCUCGCGGAACUUUGUGUUGGUAAAAGACCCUUAUGAUGGUGA UAAUACUACUAGACAAUACCGGAUGGGUAAGUCUUAAAUAUGAUCGAGGGAAAAUACCGUUAUCCU CGUUGGUCAAGCUCCACAGAGUGGUAGUGGUCAAGUGAGGCUUAACGUAGCGUGAACCAAAGAA GUUCUCCUAGAGUGUGUUGUUUACCAACACACUGUCCUAUGGGGGCCAACAUAGGUCCA-3'
General forward primer	5'-AACTGAGATACTACAGCGTGA-3'
CTV 3' UTR reverse primer	5'-i2OMeU//i2OMeG/GACCTATGTTGGCCCCCCCATA-3'
<i>V. cholerae</i> glycine riboswitch	5'-GGUCCGUUGAAGACUGCAGGAGAGUGGUUGGUAAAACUUCGAGCCAAUAACCCGCC GAAGAAGUAAAUCUUCUAGGUGCAUUAUCUAGGCAACGAAUAAGCGAGGACUGUAGU UGGAGGAACCUCUGGAGAGAACCGUUAUACGGUCGCGGAAGGAGCAAGCUCUGCGCAUAUGCAGAGU GAAACUCUCAGGCAAAGGACAGAGGA-3'
<i>V. cholerae</i> glycine riboswitch forward primer	5'-TTCTAATACGACTCACTATAGGTCCGTTGAAGACTGCAGGAGAGTGTTGT-3'
<i>V. cholerae</i> glycine riboswitch reverse primer	5'-i2OMeU//i2OMeC/CTCTGCTTTGCTGAGAGTTTC-3'
Vg1 ribozyme	5'-GAUGUUGUAAAUAUAUAUCUUAAGAAGAACAUUGGUUAACCUUGACUUUUCUAAAUCUAAA UAGAUGAGGUGCUUGCACAUUCACUGCACAGAGGCUGAACUUAUGAAAUAUAUAUAUA-3'
Vg1 ribozyme forward primer	5'-TAATACGACTCACTATAGGGATTTGTTAATAATAATCTTAGAAGAACATGG-3'
Vg1 ribozyme reverse primer	5'-i2OMeU//i2OMeA/ATATTTTTTATTTCATATTGGAGGATTACGC-3'
Downstream peptide riboswitch	5'-GGCUCACGUUACCUUCGUUUUACGCGAGGCGCAGUUCGACUCAGGCCAUGGAACGGGACUGAG-3'
Downstream peptide riboswitch forward primer	5'-TTCTAATACGACTCACTATAGGCTCACCTGTTTCAGCGAGGCGCA-3'
Downstream peptide riboswitch reverse primer	5'-i2OMeC//i2OMeU/CAGTCCCCGTTCCATGGCCTGAGTCGAAGTCGCCTCGCTGAAA-3'

- Trizma base (Sigma-Aldrich, cat. no. T6066)
  - Ultra GelRed (Vazyme, cat. no. GR501-01)
  - Urea (Sangon Biotech, cat. no. A600148)
  - Xylene cyanol FF (Sangon Biotech, cat. no. A630005)
- ▲ **CAUTION** This reagent is harmful to the eyes, skin and respiratory system if inhaled and contacted.

## Equipment

- 0.22 µm sterile filter units (Sorfa Life Science, cat. no. 622110)
- AKTA pure micro (Cytiva, cat.no. 29302479)
- Amicon Ultra-0.5 centrifugal filter unit of 3 kDa (Merck Millipore, cat. nos. UFC500396), 10 kDa (UFC501096), 30 kDa (UFC503096), 50 kDa (UFC505096) and 100 kDa (UFC510096)
- Amicon Ultra-15 centrifugal filter unit of 3 kDa (Merck Millipore, cat. nos. UFC900324), 10 kDa (UFC901024), 30 kDa (UFC903024), 50 kDa (UFC905024) and 100 kDa (UFC910024)
- Analytical balance ME204 (Mettler-Toledo, model no. ME204)
- Autoclave (STIK, cat. no. IMJ-78A)
- Autogrid alignment tool (Thermo Fisher Scientific, cat. no. 943290997641)

- Autogrid assembly station (Thermo Fisher Scientific, cat. no. 1130697)
- Autogrid container (Thermo Fisher Scientific, cat. no. 1084591)
- Autogrid tweezers (Thermo Fisher Scientific, cat. no. 943290997631)
- Capsule (Thermo Fisher Scientific, cat. no. 943290997591)
- Cassette (Thermo Fisher Scientific, cat. no. 1020863)
- Cassette tweezers (Thermo Fisher Scientific, cat. no. 943290997651)
- C-clip (Thermo Fisher Scientific, cat. no. 1036171)
- C-clip insertion tool (Thermo Fisher Scientific, cat. no. 943290997571)
- C-clip ring (Thermo Fisher Scientific, cat. no. 1036173)
- Centrifuge 5425 R (Eppendorf, model no. 5425 R; rotor no. FA-24×2- PTFE)
- Centrifuge 5910 Ri (Eppendorf, model no. 5910 Ri; rotor no. FA- 6×250)
- Centrifuge tube of 1.5 mL (NEST, cat. nos. 615601), 2.0 mL (620611), 15 mL (601001) and 50 mL (602002)
- Cryo-EM grid storage puck system (Baishu Photoelectric Technology)
- Cryo grid boxes (Ted Pella, cat. nos. 160-40 and 160-42W)
- Dewar (4 L; Worthington, model no. 4LDB)
- Digital rocker (Thermo Fisher Scientific, cat. no. 88882002)
- DYCZ-24A electrophoresis cell (Liuyi, model no. DYCZ-24A)
- EZee mini-centrifuge (Scilogex, cat. no. D1008)
- Falcon 3EC direct electron detector (Thermo Fisher Scientific, model no. 1125167)
- FiveEasy plus pH meter (Mettler Toledo, cat. no. FP20-Std-Kit)
- Gel Doc XR+ system with image lab software (Bio-Rad, cat. no. 1708195) with XcitaBlue conversion screen (Bio-Rad, cat. no. 1708182)
- Glacios 2 cryo-transmission electron microscope (Cryo-TEM) (Thermo Fisher Scientific, model no. 1275283)
  - ▲ **CRITICAL** We used the Talos Arctica Cryo-TEM, which is no longer available. The product listed above is an appropriate substitute.
- Grid container tool (Thermo Fisher Scientific, cat. no. 943290997671)
- Horizontal electrophoresis apparatus (Liuyi, cat. no. 122-3146)
- K3 Direct detection camera equipped with a Gatan imaging filter (GIF) continuum K3 system (Gatan)
  - ▲ **CRITICAL** We used the Gatan K2 direct electron detective camera equipped with a Bioquantum energy filter, which is no longer available. The product listed above is an appropriate substitute.
- Krios G4 cryo-TEM (Thermo Fisher Scientific, model no. 1402974)
  - ▲ **CRITICAL** We used the Titan Krios G3i cryo-TEM, which is no longer available. The product listed above is an appropriate substitute.
- Leica EM cryo tool drying (Leica, model no. 613704)
- Loading station (Thermo Fisher Scientific, cat. no. 1402293)
- Milli-Q direct water purification system (Milli-Q, cat. no. ZR0Q016WW)
- Mini-PROTEAN Tetra cell and PowerPac HC power supply (Bio-Rad, cat. no. 1658027)
- NanoDrop One<sup>c</sup> (Thermo Fisher Scientific, cat. no. 840-317500)
- PELCO easiGlow glow discharge cleaning system (Ted Pella, cat. no. 91000S-230)
- Portable UV analyzer (Hangzhou Qiwei instrument, model no. WFH- 204BS)
- Precision balance (Mettler-Toledo, model no. ME3002T/A00)
- Prometheus Panta (NanoTemper Technologies GmbH, cat. no. PR-013)
- SCI-RS digital see-saw rocker (Scilogex, cat. no. 833131019999)
- Superdex 75 increase 10/300 (Cytiva, cat. nos. 29148721), 5/150 (29148722), 3.2/300 (29148723)
- Superdex 200 increase 10/300 (Cytiva, cat. nos. 28990944), 5/150 (28990945), 3.2/300 (28990946)
- Tweezers for EM grids (Ted Pella, cat. nos. 47000-600, 47000-500, 5081)
- Vacuum freeze dryer (Biocool, cat. no. FD-1C-50)
- Vitrobot Mark IV system (Thermo Fisher Scientific)
- Vortex mixers (Scilogex, cat. no. 821200059999)

## Software

- Auto-DRRAFTER ([https://www.rosettacommons.org/docs/latest/application\\_documentation/rna/auto-drrafter#manually-setting-up-an-auto-drrafter-run](https://www.rosettacommons.org/docs/latest/application_documentation/rna/auto-drrafter#manually-setting-up-an-auto-drrafter-run))
- Bio-Rad Image Lab 6.1 software (<https://www.bio-rad.com/en-us/product/image-lab-software?ID=KRE6P5E8Z>)
- Chimera 1.16 (<https://www.cgl.ucsf.edu/chimera/download.html>; <https://www.rbvi.ucsf.edu/chimera/tutorials.html>)
- ChimeraX 1.7.1 (<https://www.cgl.ucsf.edu/chimerax>; <https://www.cgl.ucsf.edu/chimerax/tutorials.html>)
- Coot 0.9.8 (<https://www2.mrc-lmb.cam.ac.uk/personal/pemsley/coot/>; <https://www2.mrc-lmb.cam.ac.uk/personal/pemsley/coot/web/tutorial>)
- CryoREAD v10.1 (<https://github.com/kiharalab/CryoREAD>; <https://kiharalab.org/emsuites/cryoread.php>)
- CryoSPARC 4.4.1 (<https://cryosparc.com/>; <https://guide.cryosparc.com/>)
- CTFFIND 4 ([https://grigoriefflab.umassmed.edu/ctffind4](https://grigoriefflab.umassmed.edu/ctf_estimation_ctffind_ctftilt));  
<https://grigoriefflab.umassmed.edu/ctffind4>)
- EMAN 2.31 (<https://blakebcm.edu/emanwiki/EMAN2/Install/BinaryInstallAnaconda/2.31>)
- EMRNA v1.5 (<http://huanglab.phys.hust.edu.cn/EMRNA/>)
- EPU 2.9.1 (Thermo Fisher Scientific)
- ERRASER ([https://phenix-online.org/version\\_docs/dev-2840/reference/eraser.html](https://phenix-online.org/version_docs/dev-2840/reference/eraser.html))
- FARFAR2 (<https://rosie.rosettacommons.org/farf2>)
- M2seq (<https://github.com/ribokit/M2seq>)
- MotionCor2 v1.1 (<https://emcore.ucsf.edu/ucsf-software>; <https://emcore.ucsf.edu/useful-protocols>)
- OriginPro 2023 (<https://www.originlab.com/>)
- Phenix.real\_space\_refine 1.20 (<https://phenix-online.org/download>; [https://phenix-online.org/workshops\\_tutorials](https://phenix-online.org/workshops_tutorials))
- PR.Panta Analysis v1.4.4 (NanoTemper Technologies GmbH, cat. no. PR-S071)
- PR.Panta Control v1.4.4 (NanoTemper Technologies GmbH, cat. no. PR-S061)
- QRNAS (<http://genesilico.pl/software/stand-alone/qrnas>)
- Relion 4.0 (<https://github.com/3dem/relion/tree/ver4.0>)
- Rosetta 3.12 ([https://www.rosettacommons.org/docs/latest/build\\_documentation/Build-Documentation](https://www.rosettacommons.org/docs/latest/build_documentation/Build-Documentation))
- Sherpa 1.12.3 (Thermo Fisher Scientific)
- SimRNA 3.2 (<https://genesilico.pl/software/stand-alone/simrna>)
- SimRNAsweb 2.0 (<https://genesilico.pl/SimRNAsweb>)

## Reagent setup

▲ **CRITICAL** All the solutions and buffers used for RNA are prepared with DEPC- treated water to avoid RNase contamination.

### Agarose, 1% (wt/vol) solution in 1× TAE buffer

Weigh 0.50 g agarose and dissolve in a total volume of 50 mL of 1× TAE buffer. Heat the agarose solution in the microwave until the agarose is completely melted, take it out and shake to mix. Add 5 µL Ultra GelRed solution and mix well. This solution must be prepared fresh before use.

### Ampicillin, 100 mg/mL

Dissolve 5.0 g ampicillin in sterile water to reach a final volume of 50 mL. This solution can be prepared in advance and stored in 1 mL aliquots at -20 °C for years.

### DEPC-treated water

Add 1 mL DEPC to Milli-Q water and adjust to a total volume of 1 L. Incubate and mix at room temperature (20–25 °C) for 3 h before autoclaving. This solution can be prepared in advance and stored at 4 °C for 1 year.

# Protocol

## DTT, 1 M solution

Dissolve 7.7 g DTT in DEPC-treated water to reach a final volume of 50 mL, then filter through a 0.22 µm disposable sterile filter after the solids have completely dissolved. This solution can be prepared in advance and stored in 1 mL aliquots at –20 °C for years.

## EDTA, pH 8.0, 0.5 M solution

Weigh 93 g Na<sub>2</sub>EDTA 2H<sub>2</sub>O, dissolve in 300 mL of DEPC-treated water, and adjust the pH to 8.0 by adding NaOH. Adjust the volume to 500 mL with DEPC-treated water and filter the solution through a 0.22 µm filter paper using a vacuum pump after the solids have completely dissolved. This solution can be prepared in advance and stored at room temperature for months. The EDTA disodium salt will not fully dissolve until the pH of the solution is adjusted to 8.0 by adding NaOH.

## Elution buffer

This solution is composed of 30 mM NaOAc, pH 5.2, and 1 mM EDTA, pH 8.0, in DEPC-treated water. Mix 500 µL of 3 M NaOAc, pH 5.2, and 100 µL of 0.50 M EDTA, pH 8.0, in DEPC-treated water to reach a final volume of 50 mL and filter through a 0.22 µm disposable sterile filter. This solution must be prepared fresh before use.

## KCl, 4 M solution

Weigh 15 g KCl and dissolve in a total volume of 50 mL DEPC-treated water and filter through a 0.22 µm disposable sterile filter after the solids have completely dissolved. The solution can be prepared in advance and stored at 4 °C for months.

## LB medium

LB medium is 1.0% (wt/vol) tryptone, 0.50% (wt/vol) yeast extract and 1.0% (wt/vol) NaCl in ddH<sub>2</sub>O. Weigh 10 g tryptone, 5.0 g yeast extract and 10 g NaCl in 800 mL ddH<sub>2</sub>O. After complete dissolution, add NaOH to adjust the pH to 7.0, add ddH<sub>2</sub>O to 1 L, aliquot, autoclave and store at room temperature for weeks.

## MgCl<sub>2</sub>, 1 M solution

Dissolve 10 g MgCl<sub>2</sub> 6H<sub>2</sub>O in DEPC-treated water to reach a final volume of 50 mL and filter through a 0.22 µm disposable sterile filter after the solids have completely dissolved. The solution can be prepared in advance and stored at 4 °C for months.

## NaOAc solution, pH 5.2, 3 M solution

Weigh 123 g sodium acetate and dissolve in 200 mL of DEPC-treated water. After complete dissolution, add acetic acid to adjust the pH to 5.2, add DEPC-treated water to 500 mL and filter through a 0.22 µm filter paper using a vacuum pump. The solution can be prepared in advance and stored at room temperature for months.

## Refolding buffer (10x)

This solution is composed of 0.1 M Tris–HCl, pH 7.4, and 1 M KCl in DEPC-treated water. Mix 1 mL of 1 M Tris–HCl, pH 7.4, and 2.5 mL of 4 M KCl, in a total volume of 10 mL DEPC-treated water and filter through a 0.22 µm disposable sterile filter. This solution can be prepared in advance and stored in 1 mL aliquots at –20 °C for years.

## RNA native loading buffer (2×)

This solution is composed of 20% (vol/vol) 5× THE buffer, 10% (vol/vol) glycerol, 0.10% (wt/vol) bromophenol blue, 0.10% (wt/vol) xylene cyanol FF in DEPC-treated water. Weigh 0.050 g bromophenol blue and 0.050 g xylene cyanol FF, dissolve them in 5 mL of glycerol, add 10 mL of 5× THE buffer and add DEPC-treated water to make a total volume of 50 mL. This solution can be prepared in advance and stored at room temperature for months.

# Protocol

## Tris-acetate-EDTA (TAE) buffer (50×)

TAE buffer is composed of 2 M Tris-acetate and 100 mM EDTA in Milli-Q H<sub>2</sub>O. Dissolve 242 g Trizma base, 37 g Na<sub>2</sub>EDTA 2H<sub>2</sub>O in Milli-Q water to reach a final volume of 1 L and filter through a 0.22 µm filter paper using a vacuum pump. The solution can be prepared in advance and stored at room temperature for months.

## TBE urea loading buffer (2×)

This solution is composed of 7 M urea, 10% (vol/vol) of 10× TBE buffer, 10% (vol/vol) glycerol, 0.10% (wt/vol) bromophenol blue and 0.10% (wt/vol) xylene cyanol FF in DEPC-treated water. Weigh 21 g urea and dissolve in 5 mL of glycerol. Add 5 mL of 10× TBE buffer and DEPC-treated water to promote complete dissolution of urea. Add 0.050 g bromophenol blue and 0.050 g xylene cyanol FF to this solution and add DEPC-treated water to a total volume of 50 mL. This solution can be prepared in advance and stored at room temperature for months.

## Transcription buffer (10×)

Transcription buffer (10×) is composed of 400 mM Tris-HCl pH 7.9, 200 mM MgCl<sub>2</sub>, 20 mM spermidine and 0.10% (vol/vol) Triton X-100. Weigh 0.15 g spermidine and measure 50 µL of 100% Triton X-100, 20 mL of 1 M Tris-HCl pH 7.9, 10 mL of 1 M MgCl<sub>2</sub>, dissolve in a total volume of 50 mL DEPC-treated water, and filter through a 0.22 µm disposable sterile filter after the solids have completely dissolved. This solution can be prepared in advance and stored at -20 °C for months.

## Tris-borate-EDTA (TBE) buffer (10×)

TBE buffer (10×) is composed of 890 mM Trizma base, 890 mM boric acid and 20 mM EDTA. Dissolve 108 g Trizma base, 7.4 g Na<sub>2</sub>EDTA 2H<sub>2</sub>O, 55 g boric acid in Milli-Q water to reach a final volume of 1 L and filter the TBE buffer through a 0.22 µm filter paper using a vacuum pump. This solution can be prepared in advance and stored at room temperature for months.

## Tris-HCl, pH 7.4, 7.9, 8.0 and 8.1, 1 M solution

Weigh 61 g Trizma base, dissolve in 450 mL of DEPC-treated water and adjust the pH to 7.4, 7.9, 8.0 and 8.1 by adding HCl. Adjust the volume to 500 mL with DEPC-treated water and filter this solution through a 0.22 µm filter paper using a vacuum pump after the solids have completely dissolved. These solutions can be prepared in advance and stored at room temperature for months.

## Tris-HEPES-EDTA (THE) buffer (5×)

THE buffer (5×) is composed of 165 mM Trizma base, 329 mM HEPES and 0.5 mM EDTA. Weigh 40 g Trizma base, 157 g HEPES, add 2 mL of 0.5 M EDTA, pH 8.0, in Milli-Q water to reach a final volume of 2 L and filter this solution through a 0.22 µm filter paper using a vacuum pump. This solution can be prepared in advance and stored at room temperature for months.

## 10% (wt/vol) APS solution

Dissolve 1.0 g APS in DEPC-treated water to reach a final volume of 10 mL and filter through a 0.22 µm disposable sterile filter after the solids have completely dissolved. This solution can be stored at 4 °C for ~6 months.

## Native PAGE solution

Native PAGE solutions are composed of 5.0%, 6.0%, 8.0% or 10% (vol/vol) Acryl/Bis solution (29:1), 20% (vol/vol) 5× THE buffer or 10% (vol/vol) 10× refolding buffer, MgCl<sub>2</sub> with the same final concentration as RNA refolding condition, 1.0% (vol/vol) APS solution and 1.0 % (vol/vol) TEMED in DEPC-treated water. Add MgCl<sub>2</sub> with the same final concentration as RNA refolding condition, measure 1.2 mL, 1.4 mL, 1.9 mL or 2.3 mL of Acryl/Bis 30% solution (29:1), 1,400 µL of 5× THE buffer or 700 µL of 10× refolding buffer in DEPC-treated water to reach a final volume of 7 mL. Then add 70 µL of APS buffer, 7.0 µL of TEMED and mix the solution well. This solution must be used immediately after preparation.

# Protocol

## Denaturing PAGE solution

Denaturing PAGE solutions are composed of 5.0%, 6.0%, 8.0% or 10% (vol/vol) Acryl/Bis solution (29:1), 7 M urea, 10% (vol/vol) 10× TBE buffer, 1.0% (vol/vol) APS solution, 1.0‰ (vol/vol) TEMED. Weigh 210 g urea, measure 83 mL, 100 mL, 133 mL or 167 mL of 30% Acryl/Bis solution (29:1), 50 mL of 10× TBE buffer in DEPC-treated water to reach a final volume of 500 mL. These solutions can be prepared in advance and stored at 4 °C for ~2 weeks. Measure ~50 mL of solution, add 500 µL of 10% APS solution and 50 µL of TEMED and mix the solution well. This solution must be used immediately after preparation.

## Procedure

### Linearized DNA template preparation

#### ● TIMING 7 h–2 d

1. Obtain large-scale linearized DNA templates either by PCR (option A) or enzymatic digestion (option B).
  - (A) **PCR**
    - (i) Mix 400 ng plasmid in Step 1, 500 µL of 2× Phanta max master mix, 40 µL of forward and reverse primers in DEPC-treated water to a total volume of 1 mL.  
▲ **Critical STEP** High-fidelity DNA polymerase and 2'-O-methylated reverse primers can be used to improve 3' end homogeneity.
    - (ii) Perform the PCR reaction according to the manufacturer's instructions.
    - (iii) Mix 1 µL of the PCR product with 1 µL of 10× DNA loading buffer, load 1 µL onto 1% (wt/vol) natural agarose gel containing 1:10,000 (vol/vol) Ultra GelRed solution (5 µL for a 50 mL agarose gel), with 1 µL of marker D2000.
    - (iv) Run the gel at 140 V for 30 min and visualize in a Gel Doc to examine the PCR result.
  - (B) **Enzymatic digestion reaction**
    - (i) Transform commercial DH5α competent cells following the manufacturer's instruction.
    - (ii) Extract the plasmid following the instructions of the commercial plasmid DNA mini kit I.
    - (iii) Linearize the DNA templates by digesting the plasmids following the instructions of the commercial restriction enzymes.
  2. Mix the DNA templates with an equal volume of chloroform/isoamyl alcohol (24:1 vol/vol), centrifuge at 14,000g for 1 min at 4 °C and carefully separate the upper water-soluble phase into a new tube. Repeat the extraction of DNA templates by chloroform/isoamyl alcohol one more time for optimal separation.
  3. Add an equal volume of isopropanol and a tenth volume of 3 M NaOAc pH 5.2, flash-freeze in liquid nitrogen, and centrifuge at 14,000g for 45 min at 4 °C.
  4. Carefully aspirate the supernatant and wash the precipitate with 70% (vol/vol) ethanol twice. Air dry until no ethanol remains, then dissolve the DNA templates in 50 µL DEPC-treated water. Measure the DNA concentration for future use.

■ **PAUSE POINT** Linearized DNA template can be stored at –20 °C for months.

## IVT

#### ● TIMING 7 h

▲ **Critical** It is strongly recommended to understand the RNA functions to optimize IVT conditions and to better interpret the IVT results. For example, self-cleaved and self-spliced ribozymes may undergo catalytic reactions during IVT and generate additional catalysis products; the IVT conditions of riboswitches may include the corresponding ligands to stabilize one conformation over another.

5. Perform IVT. For our in-house prepared T7 RNAP we follow the substeps below. If commercial T7 RNAPs are used, follow the manufacturer's instructions.

# Protocol

- Mix 30 µg linearized DNA template from Step 4, 30 µL of 100 mM NTPs, 100 µL of 10× transcription buffer, 10 µL of 1 M DTT, 60 µL of 7.5 U/µL T7 RNA polymerase, 5 µL of 40 U/µL RNase inhibitor and 10 µL of 0.1 U/µL pyrophosphatase with DEPC-treated water to give a total reaction volume of 1 mL.
- Incubate the mixture at 37 °C for 1–3 h.
- Add DNase I to digest DNA templates at 37 °C for 15 min.
- Measure the concentration of the IVT product for future use.
- Repeat the above substeps with different conditions (Table 1) if the IVT result is not satisfactory after assessment in Step 7. Additional conditions can also be screened following Steps 13–18.

◆ **TROUBLESHOOTING**

6. (Optional) Remove the hammerhead or HDV ribozyme sequences in IVT products by adjusting MgCl<sub>2</sub> concentration to 40 mM, followed by three rounds of thermal cycling (1 min at 72 °C, 5 min at 65 °C and 10 min at 37 °C per round).
7. To examine the homogeneity of IVT products by denaturing PAGE follow option A, whereas to examine the folding status by native PAGE follow option B.
  - (A) **Denaturing PAGE**
    - (i) Mix 10 ng IVT mixture with 2× TBE urea loading buffer to a final 2 µL of 1× solution and incubate at 95 °C for 3 min.
    - (ii) Load samples onto a denaturing 7 M urea 29:1 Acryl/Bis gel and run the gel at 300 V.

▲ **Critical Step** The concentration of Acryl/Bis solution (29:1) and the electrophoresis time depend on the size of RNAs. For RNAs less than 200 nt, an 8% gel is run for 1–2.5 h; for RNAs 200–500 nt, a 6% gel is run for 2–3.5 h; for RNAs larger than 500 nt, a 5% gel is run for 3–4.5 h. An increase of the bis-acrylamide ratio to 19:1 results in decreased pore sizes that favor separations of smaller RNAs.
    - (iii) Stain the gel with SYBR Gold and visualize in a Gel Doc.
  - (B) **Native PAGE**
    - (i) Mix 10 ng IVT mixture with 2× native TBE loading buffer to a final 2 µL of 1× solution.
    - (ii) Load samples onto a nondenaturing 29:1 Acryl/Bis gel, run the gel at 140 V. The entire process should be carried out at 4 °C to prevent overheating that leads to RNA denaturation.

▲ **Critical Step** For RNAs less than 200 nt, an 8% gel is run for 0.6–1.5 h; for RNAs 200–500 nt, a 6% gel is run for 0.8–2 h; for RNAs larger than 500 nt, a 5% gel is run for 1–2.5 h.
    - (iii) Stain the gel with SYBR Gold and visualize in a Gel Doc.

## RNA purification

● **TIMING 1 h–1 d**

8. IVT products with a clean target band in denaturing PAGE, which also fold into one major conformation shown as one major band in native PAGE, can be subjected to buffer exchange; follow option A as a quick purification. Otherwise, follow option B for SEC purification to separate different conformations under nondenaturing conditions, or follow option C for denaturing purification to purify RNAs that require subsequent refolding processes.
  - (A) **Buffer exchange**
    - (i) Add 50 µL of proteinase K (0.6 U/µL) to 1 mL of the IVT product (Steps 5–6) and incubate at 37 °C for 30 min to digest proteins and centrifuge at 14,000g for 5 min at 4 °C.
    - (ii) Transfer the supernatant to the concentrator column to exchange with 1× IVT buffer at 12,000g for 15 min at 4 °C. Repeat until the concentration of flow through determined by OD 260/280 is less than 20 ng/µL.

▲ **Critical Step** Choose the concentrator columns with appropriate cutoffs that are normally 1/3 of the RNA molecular weights. Cutoffs that are too small will extend the concentration time, whereas cutoffs that are too large will result in loss of RNAs.

# Protocol

(iii) Transfer the concentrated sample to a new 1.5 mL tube, measure and label the RNA concentration.

(iv) Repeat Step 7 to check the homogeneity and folding status of the concentrated IVT product.

(v) Store on ice until required.

**(B) SEC purification**

▲ **CRITICAL** We use the AKTA micro pure instrument equipped with a Superdex increase 3.2/300 column for analytical purpose; however, different columns should be used for preparation/other purposes. In general, the entire process should be carried out at 4 °C.

(i) Wash the column with corresponding buffers to equilibrate, and set the flow rate to 0.3 mL/min and detection absorbance at 260 nm.

(ii) Choose the appropriate collection method: the peak fractionation collection method enables accurate separation of close-by conformation peaks; the fixed-volume collection method is useful for one major peak or well-separated multiple peaks.

(iii) Inject the IVT product from Steps 5–6.

(iv) Repeat Step 7B to assess the fractions of interest and combine fractions of the same conformation and concentrate as described in Step 8A if necessary.

(v) Store samples on ice until required.

**(C) Denaturing purification**

(i) Take the concentrated IVT product from Step 8A(i) to repeat Step 7A for large-scale denaturing PAGE purification.

(ii) To isolate RNA, either:

- Cut the target band using a hand-held UV lamp, then crush the gel into slurry in a 50 mL tube and add elution buffer to incubate overnight. Filter the mixture through a 0.22 µm filter.

Alternatively for electroelution:

- Transfer the gel to an electroelution apparatus chamber and run at 100 V for 2–12 h in 1× TBE buffer and transfer the solution containing the target RNA to a new 1.5 mL tube.

(iii) Concentrate the RNA sample by precipitation as described in Steps 3–4 or a concentrator column as described in Step 8A if necessary.

(iv) Measure the concentration and store on ice until required.

◆ **TROUBLESHOOTING**

9. Following denaturing purification (Step 8C), assess the quality of purified RNA as described in Step 7. RNA aliquots can be lyophilized for long-term storage. If following buffer exchange (Step 8A) or SEC purification (Step 8B), proceed directly to Step 20.

■ **PAUSE POINT** Lyophilized RNA can be stored at –80 °C for 1–2 years.

## Condition screening and RNA refolding

● **TIMING** 2–5 h

▲ **CRITICAL** Following denaturing purification (Step 8C), RNAs require refolding. Refolding conditions can be screened by native PAGE (Steps 10–12) or the alternative method of nanoDLS at a higher throughput if more variables need to be extensively screened (Steps 13–18). If following buffer exchange (Step 8A) or SEC purification (Step 8B), proceed directly to Step 20.

▲ **CRITICAL** It is extremely important to understand RNA functions so that conditions used to perform RNA functions can be primarily tested for refolding.

10. To screen RNA refolding conditions by PAGE, set up the screening by mixing 100 ng RNA, 1 µL of 10× refolding buffer (Table 1) and DEPC-treated water to give a total reaction volume of 9 µL for each screening condition.

11. Prepare stock solutions of the corresponding MgCl<sub>2</sub> concentrations (Table 1), then add 1 µL MgCl<sub>2</sub> solution to each condition following the cooling strategies (Table 2).

12. Repeat Step 7B to assess RNA refolding conditions by native PAGE (Fig. 3b–d and Extended Data Fig. 1). If the tested conditions are not optimal and more variables need to be extensively screened, repeat Steps 10–12 or follow Steps 13–18 to screen with nanoDLS at a higher throughput.

13. Follow Step 11 and adjust the volumes to obtain 20 µL folded RNAs in each screening condition, followed by centrifugation at 15,000g for 15 min at 4 °C.  
▲ **CRITICAL STEP** To obtain ideal results from nanoDLS, final RNA concentrations should vary from 100 to 500 ng/µL and meet nanoDLS parameters: scattering intensity above  $10^6$  counts per second (cts/s) and SNR above 120 for the Prometheus Panta instrument.
14. Load 10 µL of the solution into the capillary. Two capillaries for each condition.
15. Place capillaries on the Prometheus Panta tray (NanoTemper Technologies).
16. Run Prometheus Panta size analysis in high-sensitivity mode.  
◆ **TROUBLESHOOTING**
17. Analyze data with Prometheus Panta Analysis software: observe differences in intensity distribution profiles, rH and PDI (Fig. 4). If suitable folding conditions have been identified, proceed to Step 19, otherwise repeat Steps 12–17.
18. (Optional) For stack intensity profiles, export raw size analysis data with Panta Control software and perform analysis and plotting with Origin software.  
◆ **TROUBLESHOOTING**

## Sample vitrification and cryo-EM data collection

### ● TIMING 0.5–4 d

19. Repeat Steps 10–11 to prepare the desired amount of RNA samples in the optimal conditions for vitrification and cryo-EM analysis. RNA samples can be temporarily stored on ice.
20. Set the chamber temperature and relative humidity of the Mark IV Vitrobot to 4 °C and 100%, respectively. Assemble filter papers in the chamber and cryogen container for vitrification.  
▲ **CRITICAL STEP** The relative humidity in the sample preparation room is recommended to be lower than 30% to avoid severe ice contaminations.
21. Select the appropriate types of grids (Tables 1 and 4) and perform glow discharge<sup>47</sup>. Copper grids are primarily used in the screening stage. Supporting films can be used when the final concentration is lower than 1 µM (or 0.1 µg/µL) and the RNA is larger than 100 kDa (300 nt). Refer to the ‘Experimental design’ section for further discussion.  
▲ **CRITICAL STEP** Grids without supporting films are normally glow discharged for 40–120 s, whereas grids with supporting films are glow discharged for much shorter amount of time, typically less than 10 s, depending on the sturdiness of the films. Some extremely fragile films are not recommended for glow discharge.
22. Load the grids onto the Vitrobot and add 2–3 µL of samples on the grids, blot the grids with filter papers and inject into the cryogen (e.g., liquid ethane). Transfer the grids to precooled grid boxes in liquid nitrogen. Clip autogrids for future use<sup>48</sup>.  
▲ **CRITICAL STEP** Grids without supporting films are typically blotted for 2–3 s, whereas grids with supporting films are usually set to wait for 30–60 s before blotting for 1–2 s to allow particle accumulation on the films. Several variables such as blot time, blot force, wait and drain time can be tuned to obtain optimal ice thickness<sup>47,115</sup> (Fig. 5).  
■ **PAUSE POINT** The frozen grids and autogrids can be stored in liquid nitrogen for years.  
◆ **TROUBLESHOOTING**
23. Load autogrids into the precooled cassette, transfer the cassette into the NanoCab filled with liquid nitrogen, then dock the cassette onto the microscope. Check that the microscope is ready for imaging<sup>48,175</sup>.
24. Open EPU and select the Atlas mode to obtain an overview of the ice distribution on the grid. Move the sample stage to the square of interest and acquire an image in the GridSquare mode. Find the eucentric height and move the stage to the holes with proper ice in the Hole/EucentricHeight mode. Collect cryo-EM images in data acquisition mode<sup>48</sup> (Extended Data Fig. 3).
25. If the grid is suboptimal and not suitable for data collection, unload this grid and repeat Step 24 to screen the next one.
26. After completion of screening all the autogrids, if the ice thickness is not optimal (Fig. 5a,b), repeat Steps 20–25 to screen for variables in grids, glow discharge time and Vitrobot parameters until optimal ice thickness is obtained. If RNA sample status is not ideal for

# Protocol

- data collection (e.g., low concentration, aggregation, denaturation) (Fig. 5c,e–f), repeat Steps 10–19 to screen for variables in IVT and RNA folding until optimal micrographs are observed ready for data collection (Fig. 5d).
27. Activate ‘Ice Filter’ in EPU to allow selection of holes based on ice thickness as determined by the image intensity.
- ▲ **CRITICAL STEP** The ice thickness can also be quantitatively measured by on-the-fly methods such as Measure Ice integrated in EPU<sup>142</sup>.
28. Set up automatic data collection following the EPU scheme, check the microscope and camera settings to ensure smooth data collection<sup>48</sup>. Preliminary data collection normally takes only a few hours, whereas large-scale data collection for optimized sample can take several days.
- Multiple exposures can be set up to increase data collection throughput (Extended Data Fig. 3e)
  - The stage can be tilted to collect data on grids with particles that have preferred orientations<sup>176</sup> (Fig. 5g)
  - The direct electron detective cameras are normally set to counting mode for data collection. For K2 and K3 cameras (Gatan), super-resolution mode can be selected to increase sampling frequency of the micrographs<sup>177</sup>; however, the micrographs are substantially larger in size compared with those collected in counting mode
  - Set up the automatic data transfer to the data processing cluster or external hard drives to avoid overfilling the local storage

## Data processing

### ● TIMING 1–6 d

▲ **CRITICAL** The data processing pipeline is modular and each step has multiple options that are interchangeable. The following steps are exemplified in Relion.

29. Import all movie stacks and perform ‘Motion correction’ using MotionCor2 with ‘Number of patches X, Y’ set to ‘5, 5’ and ‘Other MotionCor2 arguments’ set to ‘-Iter 10’. The dose per frame is provided accordingly and the rest parameters remain default<sup>178</sup>.

▲ **CRITICAL STEP** For relatively small RNAs or sparse particle distribution, ‘Number of patches X, Y’ can be set to ‘3, 3’. MotionCor2 is also integrated in cryoSPARC, and other movie alignment methods in Relion<sup>164</sup>, cryoSPARC<sup>165</sup>, Warp<sup>179</sup>, EMAN2<sup>151</sup> or cisTEM<sup>180</sup> could also be used to evaluate motions in full frames or local patches.

30. Perform the ‘contrast transfer function (CTF) estimation’ using CTFFIND4 in default setting, except the ‘Amount of astigmatism’ is set to 1,000 Å<sup>181</sup>. Micrographs with thon rings extended beyond 6 Å are visually examined and selected.

▲ **CRITICAL STEP** For tilted data, the latest CTFFIND5 (ref. 182) (integrated in cisTEM) and alternative methods such as Gctf<sup>183</sup> (integrated in Relion) or patch CTF (integrated in cryoSPARC) could be used.

31. Numerous automated particle picking algorithms have been developed that utilize template-free picking such as Gaussian blobs<sup>184,185</sup>, reference-based template matching<sup>186–190</sup> and reference-based convolutional neural network (CNN) (Fig. 6)<sup>148–155,191</sup>, which can be interchangeably tested for optimized result. Here, we describe the use of Blob picker in cryoSPARC (option A; Fig. 6a–g), reference-based template matching in Relion (option B; Fig. 6h–j) and reference-based CNN particle picking in EMAN2 (option C; Fig. 6k–p).

#### (A) Blob picker in cryoSPARC

- Start a new ‘Blob Picker’ job and import micrographs from Step 30 (Fig. 6a).
- Check ‘Show advanced’ and set the expected minimum and maximum particle diameter. For *Tetrahymena* group I intron this value is set to 50 and 150 Å.
- Turn on ‘Circular blob’ and run the job, keeping the remaining parameters at their default settings (Fig. 6a).
- After the ‘Blob Picker’ job is completed, start a new ‘Inspect Particle Picks’ job. Import micrographs and particles from ‘Blob Picker’, keep parameters as default and adjust the ‘Power Histogram’ to visually check the particle picking result for each micrograph (Fig. 6b–g).

# Protocol

- 
- (v) Click ‘Done Picking’ when satisfied with the result.
    - ▲ **CRITICAL STEP** Too few picked particles will lead to a loss of effective particles that may affect reconstruction resolution (Fig. 6f), whereas too many picked particles result in extended data processing time (Fig. 6g).
  - (B) **Reference-based template matching in Relion**
    - ▲ **CRITICAL** 2D references can be generated as described later in Steps 32–35 or as projections of 3D reconstructions from the same dataset as described later in Steps 36–40. Alternatively, previous 2D classification results and 3D references can be used.
    - (i) Import micrographs from Step 30 and set the corresponding ‘Pixel size in micrographs’ (Fig. 6h).
    - (ii) Import 2D references and set the ‘Lowpass filter references’ to 20 Å and ‘Pixel size in references’ accordingly (Fig. 6i).
    - (iii) Alternatively 2D references can be generated from a 3D reference. Select ‘Yes’ in ‘OR: provide a 3D reference?’ to import a 3D reference. Provide the ‘Symmetry’, ‘3D angular sampling’ and ‘Pixel size in references’ accordingly. Keep the remaining parameters as default (Fig. 6j).
    - (iv) Click ‘Run’ to execute the job with graphics processing unit (GPU) acceleration.
  - (C) **Reference-based CNN particle picking in EMAN2**
    - (i) Navigate to ‘Particles > Interactive Particle Picking’ in the graphical user interface (GUI) and import micrographs from Step 30. Enter ‘boxsize’ and ‘ptclsiz’ values interactively determined from the micrographs. For *Tetrahymena* group I intron these values are set to 256 and 200, respectively. Fill the rest parameters as shown in Fig. 6k.
    - (ii) Manually select 15–20 reference images for both good and background references (Fig. 6l–n).
      - ▲ **CRITICAL STEP** References should be selected from different micrographs with various defocus values.
    - (iii) Train the CNN model with ‘Threshold1’ value set to 2 (Fig. 6l).
    - (iv) Click ‘Autobox’ on individual micrographs to examine the particle picking results (Fig. 6l).
      - ▲ **CRITICAL STEP** Adjust the value of ‘Threshold1’ and click ‘Autobox’ to view the result interactively (Fig. 6o,p).
    - (v) When satisfied with the particle picking result, click ‘Autobox All’.
- ◆ **TROUBLESHOOTING**
- 32. ‘Particle extraction’ is performed with imported micrographs from Step 30 and ‘input coordinates’ generated by any option from Step 31. Set the appropriate ‘particle box size’ (256 pixels for *Tetrahymena* group I intron) and rescale by fourfold to 64 pixels to accelerate 2D and 3D classifications.
  - 33. The rescaled particles are subjected to ‘2D classification’. Set the ‘Number of classes’ to 200, ‘Use EM algorithm’ to ‘Yes’, ‘Number of EM iterations’ to 50, ‘Use VDAM algorithm’ to ‘No’, ‘Mask diameter’ to 200 Å and ‘Limit resolution E-step’ to 10–20 Å, while other parameters remain default or consistent with previous steps.
  - 34. Visually examine the classification result in ‘Subset selection’ and discard classes that are not desired RNA particles and those with no obvious RNA features (Fig. 2c).
  - 35. Repeat Steps 33–34 for two to three times until most unwanted particles are discarded. The resulting ‘class\_averages.star’ file can be imported into Step 31B(ii) as 2D references. If no RNA features are observed, terminate data processing and repeat Steps 10–34 until the 2D classification results reveal RNA features.
  - 36. Import particles from Step 35 and generate ‘3D initial models’ with ‘Number of classes’ set to 6 while other parameters remain default or consistent with previous steps.
- ▲ **CRITICAL STEP** This is equivalent to the ‘Ab-Initio Reconstruction’ job in cryoSPARC. A subset of particles can be used for faster reconstruction.

37. Perform '3D classification' by importing all particles from Step 35 and one 'Reference map' from Step 36. Set 'Number of classes' to 6 and 'Limit resolution E-step' to 8–12 Å, while other parameters remain default or consistent with previous steps.

▲ **CRITICAL STEP** This step is equivalent to '3D Classification' in cryoSPARC. Multiple initial models can also be supplied in this step, analogous to 'Heterogeneous Refinement' in cryoSPARC. Homologous models and predicted models can be converted into cryo-EM density maps and used as initial models after applying low-pass filters of 40–60 Å to the maps, which can be set in 'Initial low-pass filter'.

◆ **TROUBLESHOOTING**

38. Repeat Step 34 to select particles from desired classes, then repeat Step 32 to extract particles without rescaling.
39. Conduct preliminary '3D auto-refine' by importing selected particles from Step 38 and one 'Reference map' from Step 37.

▲ **CRITICAL STEP** Import 'Reference mask' from this step and set 'Use solvent-flattened FSCs' to 'Yes' for improved reconstructions of particles with low molecular weights and SNRs.

40. Perform map sharpening in 'Post-processing' by importing 'One of the 2 unfiltered half-maps' and 'Solvent mask' from Step 39. The resulting 'template.mrc' file can be imported into 31B(iii) to generate 2D references.

▲ **CRITICAL STEP** This is equivalent to 'Homogeneous Refinement' in cryoSPARC, whereas 'Local Refinement' and 'Non-Uniform Refinement' are also available for comparisons<sup>192</sup>.

41. Visualize the resulting cryo-EM maps in Chimera<sup>193</sup>. Note that the cryo-EM maps may have inverted handedness (i.e., left-handed double helices) that need to be flipped to generate a new map using the following command line.

```
vop zflip #0  
#0 denotes the cryo-EM map ID in Chimera.
```

42. Most RNAs contain flexible regions that may be poorly resolved in the preliminary refinements. Repeat Steps 37–41 iteratively to obtain better resolved density of the flexible regions. Alternatively, several methods can be applied to sort out RNA flexibility as described below (Fig. 7). Follow option A for focused 3D classification (Fig. 7a–i) and option B for 3D variability analysis (3DVA; Fig. 7j–l).

(A) **Focused 3D classification in Relion**

- (i) Repeat Step 41 to open the cryo-EM map in Chimera with ID #0.
- (ii) Select 'Tools -> Volume Data -> Volume Eraser' to create a sphere.
- (iii) Manually move the sphere and adjust the 'Radius' to encompass the flexible regions of interest (Fig. 7a,b).
- (iv) Click 'Erase' to create a new density map containing density outside of the sphere designated as #1.
- (v) Subtract the new map #1 from the original map #0 to generate the focused sphere region #2 using the following command (Fig. 7c).
- (vi) vop #0 subtract #1
- (vii) In 'Volume Viewer', adjust the threshold 'Level' so that the density is continuous (Fig. 7d), record the number in the threshold 'Level' and navigate to 'File -> Save map as...' to save the focused map.
- (viii) Import the focused '3D map' and input the recorded number from Step 42A(vi) in 'Initial binarization threshold' of 'Mask creation' in Relion to generate a mask (Fig. 7e).
- (ix) Navigate to 'Particle subtraction' and fill 'input optimiser.star' from Step 40 and 'Mask of the signal to keep' from Step 42A(vii) while other parameters remain default (Fig. 7f).
- (x) Repeat Step 37 by importing the subtracted particles from Step 42A(viii), 'Reference map' from Step 42A(vi) and 'Reference mask' from Step 42A(vii). Set 'Perform image alignment' in the 'Sampling' tab to 'No' (Fig. 7g).

# Protocol

- 
- (xi) Repeat Step 41 to examine the focused classification result, then repeat Step 34 to select the desired classes (Fig. 7h).
  - (xii) Return to ‘Particle subtraction’, set ‘revert to original particles’ to ‘Yes’ and import the selected particles from Step 42A(x) to obtain original particles for subsequent 3D refinements (Fig. 7i).
- (B) **3DVA in cryoSPARC**
- (i) Create a new 3DVA job and input the ‘Particle Stacks’ from Step 39 and ‘Mask’ from Step 40. Set the ‘Filter resolution’ to 4 Å while other parameters remain default (Fig. 7j).
  - (ii) Create a new ‘3DVA Display’ job and input the ‘Particle Stacks’ and ‘Components’ from Step 42B(i). Set the ‘Output mode’ to ‘cluster’ and ‘Number of frames/clusters’ to 6 to obtain particles from each cluster (Fig. 7k).
  - (iii) Visualize particles from each cluster in different colors (Fig. 7l).
43. Repeat Steps 39–41 for particles from selected classes and provide the corresponding ‘Reference mask’ to obtain the final structures that better resolve RNA heterogeneity (Fig. 7m).
- ▲ **Critical step** Recent developments of ‘3D multi-body’ in Relion<sup>162</sup> and ‘3DFlex’ in cryoSPARC<sup>157</sup> allow the continuous motions of multiple flexible regions to be captured. These regions may need to be independently separated by the users and each region may have lower molecular weight limits to have sufficient SNR for the best performance of the algorithms.
44. Import ‘CTF refinement’, ‘Particles’ and ‘Postprocess STAR file’ from Step 43 to first ‘estimate (anisotropic) magnification’.
45. Import ‘Particles’ from Step 44 in ‘CTF refinement’ to ‘Perform CTF parameter fitting’. Set ‘Fit defocus’ and ‘Fit B-factor’ to ‘Per-particle’, ‘Fit astigmatism’ to ‘Per-micrograph’, ‘Estimate beamtilt’ and ‘Also estimate trefoil’ to ‘Yes’.
46. Import ‘Micrographs’ from Step 29, ‘Particles’ from Step 44 and ‘Postprocess STAR file’ from Step 43 in ‘Bayesian polishing’. Set ‘Train optimal parameters’ to ‘Yes’ and ‘Perform particle polishing’ to ‘No’ while the other parameters remain default.
47. In ‘Bayesian polishing’, import the ‘Optimized parameter file’ from Step 46 and set ‘Train optimal parameters’ to ‘No’ and ‘Perform particle polishing’ to ‘Yes’ while the other parameters remain default.
- ▲ **Critical step** In cryoSPARC, particles from Step 43 can be subjected to new jobs of ‘Global CTF Refinement’ and ‘Reference Based Motion Correction’ for analogous processing of the particles.
48. Repeat Steps 39–41 to obtain the final structures from polished particles.
49. Analyze ‘Local resolution’ of the final maps by providing the required input files and ‘User-provided B-factor’ from Step 48, and the corresponding ‘Calibrated pixel size’. Set ‘Use Relion’ to ‘Yes’ and import the ‘MTF of the detector (STAR file)’ from the corresponding detector manufacturer.
50. Coloring the local resolution density map from Step 49 in Chimera for presentation.
  - Open ‘relion\_locres\_filtered.mrc’ in Chimera
  - Select ‘Tools -> Volume Data -> Surface color’
  - Select ‘Surface color’ mode to ‘by volume data value’ and import volume file ‘relion\_locres.mrc’
  - Select ‘Options’ to modify parameters. Select ‘Set’ to set the full range of surface values with corresponding resolution. Select ‘Reverse’ to adjust the color–resolution relationship
  - Select ‘Color’ to generate a local resolution colored map

## RNA modeling

### ● TIMING 4 h–6 d

▲ **Critical** The time required for RNA modeling may vary substantially depending on availability of homologous structures and other information such as secondary structure accuracy, RNA structure complexity, computational resources and user expertise and experiences. This section assumes the users have basic knowledge and experience with

commonly used modeling software such as Chimera, Coot and Phenix. Complete information and resources for software download, installation and user manuals can be found in the ‘Software’ section.

## Docking homologous models

51. Search the RNA sequence for homologous models at Rfam sequence search page <https://rfam.org/search#tabview=tab1> (Fig. 8a)<sup>55</sup>. First, input the RNA sequence to search.
52. Navigate to the discovered Rfam family and click on the ‘Structures’ tab on the left side to explore the result (Fig. 8a). Download models through the provided links. If no homologous model is found, proceed to Step 60 for the manual curations and de novo modeling stage.
53. Open the homologous model and cryo-EM density map in Chimera, then manually fit the model into the density map so that most parts of the model are inside the density (Fig. 8b).  
▲ **CRITICAL STEP** Ensure that the model and map are superimposed in all three dimensions by opening ‘Tools -> Viewing Controls -> Side Views’.
54. Open ‘Favorites -> Command Line’ and perform rigid-body fitting using the following command:

```
fitmap #1#0  
#1 denotes the model and #0 denotes the density map.
```

55. (Optional) Repeat Steps 53–54 until most parts of the models fit into the density maps.
56. To manually select regions in each model that remain outside the density, navigate to ‘Tools -> Volume Data -> Fit in Map’ and fit ‘selected atoms’ in the designated ‘map’ (Fig. 8b).  
▲ **CRITICAL STEP** To ensure that the unselected regions of the model that already fit in the density are not moved, open ‘Options’ in the ‘Fit in Map’ module and unselect the ‘Move whole molecules’ option.
57. (Optional) Navigate to ‘Tools -> Movement -> Movement Mouse Model -> Move selection’ to manually rotate and shift the selected regions of the model into the density, then repeat Step 56.
58. Navigate to ‘File -> Save PDB’, check ‘save relative to model’ and select designated density map to save the fitted model (Fig. 8b).  
▲ **CRITICAL STEP** It is important to ensure the model remains fitted into the density map when opened in other software.
59. Open the model and map from Step 58 in Coot, navigate to ‘Calculate -> Model/Fit/Refine -> Simple Mutate...’ to generate the correct RNA sequence (Fig. 8c). In case the corrected model is complete and fits extremely well into the cryo-EM density, continue directly to the model refinements and validations stage starting from Step 72.

## Manual curations and de novo modeling assisted by RNA structure prediction

60. Open the model from Step 59 in Chimera. In case the models are incomplete or segmented, contain improper RNA folds or fit poorly to the cryo-EM density, manually select and remove all improper regions by navigating ‘Actions -> Atoms/Bonds -> delete’.
61. Predict the missing regions using software or online web servers such as SimRNA<sup>29,194</sup>, FARFAR2<sup>195</sup> or RNAComposer<sup>174</sup>. Provide sequences and secondary structures as inputs (Fig. 9a).  
▲ **CRITICAL STEP** If the predicted models contain disrupted sequence, e.g., an internal stem, a terminal tetraloop sequence such as GAAA can be inserted in between for structure prediction and subsequently removed from the generated model as described in Step 60.
62. Repeat Steps 54–57 to fit all missing regions of the model into the cryo-EM density based on the RNA sequence and secondary structure (Fig. 9b).  
▲ **CRITICAL STEP** In extreme cases where most or all regions are improperly modeled, manual de novo modeling is challenging and time consuming. A practical starting point is to identify a multiway junction in the secondary structure and correlate it with the density map (Fig. 9b). The adjacent stems can be separately predicted and fitted into the density. The accuracy of the secondary structure crucially affects the de novo modeling time.

## ◆ TROUBLESHOOTING

- 
63. Open all saved models and the density map in Coot. Change residue numbers according to the sequence in 'Edit -> Renumber residues...'.
  64. Merge all segments in 'Edit -> Merge molecules....'.
  65. Change all segments to the same chain ID in 'Edit -> Change chain IDs...'.
  66. Navigate to 'Calculate -> Model/Fit/Refine -> Add Terminal Residue...' to add missing residues to ensure the full-length sequence is modeled.
  67. Inspect each residue sequentially in the complete RNA model to ensure proper fit into the density by navigating 'Go To Atom... -> Next Residue'. Residues outside the density can be activated in 'Calculate -> Model/Fit/Refine -> Real Space Refine Zone' (Fig. 9c), then manually adjust to reposition inside the density.  
▲ **CRITICAL STEP** Examine the N-glycosidic bond of each nucleotide to ensure they are mostly in the more stable *anti* conformation. The less stable *syn* conformation is occasionally observed and needs to be validated by high-resolution density (Fig. 9d).
  - ◆ **TROUBLESHOOTING**
  68. When the resolution is close to or better than 3 Å, metal ions are resolved and can be added in the extra densities, especially those in close proximity to phosphate oxygens (Fig. 9e). Larger extra density may be attributed to small molecules added during IVT or RNA refolding, such as spermidine (Fig. 9f).
  69. Save the entire model after inspection for subsequent refinement.

## Automatic and semi-automatic modeling

70. Models can be automatically generated if homologous models are not available. Several automatic and semi-automatic modeling tools exist that utilize RNA sequences and secondary structures as inputs to generate atomic coordinates from cryo-EM density maps at subnanometer to near-atomic resolutions. Import RNA sequences, cryo-EM density maps and secondary structures: for phenix.map\_to\_model follow Option A, for ModelAngelo<sup>31</sup> follow Option B, for CryoREAD<sup>26</sup> follow Option C and for EMRNA<sup>30</sup> follow Option D. Alternatively, auto-DRRAFTER<sup>25</sup> can be used. For auto-DRRAFTER, interested readers are referred to a detailed protocol as previously described<sup>27</sup>.  
▲ **CRITICAL** GUIs are available for phenix.map\_to\_model in Phenix and ModelAngelo in Relion5 (ref. 196), whereas running CryoREAD and EMRNA require command lines. It remains challenging to directly use the automatically generated RNA models without manual curations, especially for those cryo-EM density maps with flexible regions of poor local resolutions. Additional information and advanced options of the automated modeling software could be found on their websites as described in the 'Software' section.

### (A) Phenix.map\_to\_model

- (i) Navigate to 'Model building -> Map to Model' to open GUI of 'Map to Model' in Phenix.
- (ii) Import the map and sequence into the software and fill the 'High-resolution limit' that is derived from the cryo-EM map.
- (iii) (Optional) Import a starting model. If a starting model is provided, the accuracy and speed of model building will be increased.
- (iv) Click 'Run' to execute the job and an output file will be generated as 'map\_to\_model.pdb'.

### (B) ModelAngelo

- (i) Navigate to 'Relion 5.0 -> ModelAngelo building'.
- (ii) Import 'B-factor sharpened map' from Step 40, 'FASTA sequence for protein' and 'FASTA sequence for RNA' as input.  
▲ **CRITICAL STEP** The current version of ModelAngelo requires a protein sequence as mandatory input, even if no protein is present in the structure.
- (iii) (Optional) Provide RNA secondary structure information in the dot-bracket format as an additional input file.
- (iv) Set 'Perform HMMer search' as 'No'.
- (v) Click 'Run' to execute the job with GPU acceleration.

# Protocol

## (C) CryoREAD

- Install CryoREAD to local from GitHub: <https://github.com/kiharalab/CryoREAD>.
- Execute the following command to detect the possible location of phosphates, sugars and bases based on a deep neural network.

```
python3 main.py --mode=0 -F=Path/example.mrc -M=Path/Output_
model --contour=0.5 --gpu=0 --batch_size=4 --prediction_only
```

- Open the predicted results in Chimera to check the locations of phosphates, sugars and bases.
- Execute the following command to build the model without an RNA sequence.

```
python3 main.py --mode=0 -F=Path/example.mrc -M= Path/Output_
model --contour=0.5 --gpu=0 --batch_size=4 --resolution=3 --no_
seqinfo -refine
```

- Alternatively, execute the following command to build the model with RNA sequence.

```
python3 main.py --mode=0 -F=Path/example.mrc -M= Path/Output_
model -P=Path/example.fasta --contour=0.5 --gpu=0 --batch_size=4
--resolution=3 --no_seqinfo -refine.resolution=3 .
```

- Repeat Step 70C(iii) to visualize the models.

## (D) EMRNA

- Install EMRNA to local from the following website: <http://huanglab.phys.hust.edu.cn/EMRNA/>.
- (Optional) Prepare the RNA secondary structure in the dot-bracket format as an additional input file.
- Execute the following command to build models.

```
Path/EMRNA.sh input_map.mrc input_seq.fasta input_ss.txt out_dir
-contour 0.5 -g 0 -b 40 -ncpu 4
```

71. Examine the RNA models generated from Step 70 in Chimera. Repeat Steps 60–69 if the models exhibit incomplete or segmented, contain improper RNA folds or fit poorly to the cryo-EM density.

## Model refinements and validations

- Open the Phenix GUI and select ‘phenix.real\_space\_refine’<sup>197</sup>. Import the density map and the model from Step 69 or 71, enter the resolution of the cryo-EM map.
- In the Refinement Settings tab, check ‘morphing’ and uncheck ‘nqh\_flips’ and ‘Ramachandran restraints’ while other parameters remain default. Set ‘target bonds rmsd’ to 0.002 and ‘target angles rmsd’ to 0.2 (Fig. 10a).
- Click on ‘Select Atoms -> Find Secondary Structures’ to generate the secondary structure text.eff file. Open this file in the text editor and repeat Step 67 to manually incorporate the missing base-pairing and stacking information into the file (Fig. 10b).  
▲ CRITICAL STEP The accuracy and completeness of the.eff file is essential for model refinement, especially in the flexible regions with low-resolution densities. Saenger class information is required for each base pair<sup>198</sup>.
- Load the.eff file from Step 71 in the real-space refinement window (Fig. 10c).
- Click ‘Run’ to initiate the refinement process.
- Review the validation summary page and display model problems by navigating to ‘Open in Coot’ (Fig. 10d).

78. Activate the problematic residues in 'Calculate -> Model/Fit/Refine -> Real Space Refine Zone' or 'Calculate -> Model/Fit/Refine -> Regularization Zone' and manually adjust until all parameters are within the criteria (Fig. 10e).
79. Repeat Steps 72–78 until all outlier residues are fixed with the cross-correlation score between model and map as high as possible and clash score as low as possible.
- ▲ **CRITICAL STEP** A correlation coefficient value between the model and map ( $CC_{mask}$ ) above 0.75 and a clashscore below 5 are generally acceptable. The RNA model can be further refined and regularized by software such as ERRASER<sup>199</sup> and QRNAS<sup>173</sup>.
80. Navigate to <http://molprobity.biochem.duke.edu/> for Molprobity validation. Upload the coordinate file and follow instruction to add hydrogens. Execute the 'Analyze all-atom contacts and geometry' function. Repeat Step 78 until no major issues remain in the model (Fig. 10f).
81. Navigate to <https://validate-rscb-2.wwpdb.org/validservice> and upload the cryo-EM maps and the refined models from Step 78 following the instruction for validation. Repeat Steps 77–78 until no major issues remain in the validation report (Fig. 10g).

## Troubleshooting

Troubleshooting advice can be found in Table 8.

**Table 8 | Troubleshooting table**

Step	Problems	Possible reasons	Solutions
5	No product or low yield of RNA	Vector sequence or transcription conditions are not optimized	Ensure that the transcription vector possesses two Gs immediately downstream of the T7 promoter before the target RNA sequence  Further screening of transcription conditions including transcription buffers, MgCl <sub>2</sub> concentrations, T7 RNA polymerase constructs and concentrations, DNA templates and incubation times
5, 8	RNA degradation	DEPC-treated water, buffers, concentrator column, electroelution apparatus chamber and the environment may be contaminated by RNase	Reprepare the DEPC-treated water and stock buffers  Rinse the concentrator column and electroelution chamber three times with DEPC-treated water and corresponding buffers before use  Spray RNaseZap on laboratory bench surfaces and all instruments before carrying out the experiments
16	Visible peak in the buffer reference	The concentration of the detergent in the buffer potentially exceeds CMC	Check the CMC values for the detergent used and adjust the concentrations of detergent in the screening buffer  If no detergent was used, filter the buffer with a 0.2 µm filter membrane
	Suboptimal DLS signal	RNA concentration too high or too low	For Prometheus Panta detector, increase RNA concentration if counts/s drop below 10 <sup>6</sup> ; decrease RNA concentration or attenuate laser power if counts/s are above 10 <sup>9</sup>  If another DLS system is used, please check the instrument specification for the limit of detection
18	Heterogeneous sample	Impurities (RNA aggregates, degradations, or misfolded RNAs) are present in the sample	If multiple peaks are detected with the nanoDLS software, it might be beneficial to repurify the sample or adjust buffer conditions following the results from the buffer screening to reduce polydispersity index of the sample
22	Crystalline ice on the grids	Increased grid temperature leads to melting of vitreous ice	Ensure all transfer tools that touch the frozen grids after vitrification are precooled and handle grids rapidly under a nitrogen vapor environment
31	Suboptimal particle picking results	References are not properly selected owing to low contrast and SNR of the micrographs	Micrographs can be denoised using algorithms such as Topaz to aid reference selection  2D averages with explicit RNA features can also be used as templates to improve particle picking
37	Suboptimal 3D classification results	Initial models may be improper	Initial models can be generated from this and previous datasets, homologous and predicted models. Multiple models can be supplied as initial models for 3D classification  Alternatively, the same model can be low-pass filtered to different extents and supplied as multiple initial models
62	Residue numbers are misaligned after manually placing stems into the density	Stems are not placed in the right positions or the secondary structure used is incorrect	Try all possible combinations to place each stem until the right solution is reached  Perform secondary structure probing to improve accuracy, enabling more efficient RNA modeling

**Table 6 (continued) | Troubleshooting table**

Step	Problems	Possible reasons	Solutions
67	Residues in the merged model cannot be connected	Models predicted in RNA composer lack phosphate groups at the 5' end	Delete the nucleotide lacking the phosphate group and replace with the correct nucleotide in Coot

## Timing

The time required may vary considerably for each individual RNA.

Steps 1–4, linear DNA template preparation: 7 h–2 d

Steps 5–6, RNA IVT: 1–4 h

Step 7, PAGE analyses: 1–3 h

Steps 8–9, RNA purification: 1 h–1 d

Steps 10–12, RNA refolding and PAGE analyses: 1.5–4 h

Steps 13–18, nanoDLS high-throughput screening: 1–2 h

Steps 19–22, cryo-EM grid preparation: 0.5–3 h

Steps 23–26, grid screening: 0.5–3 h

Steps 27–28, data collection: 0.5–4 d, depending on the microscope and camera setup and the data size.

Steps 29–50, data processing: 1–6 d, depending on the data size, software and computational resources, as well as the number of steps carried out in data processing (Table 6).

Steps 51–81, RNA modeling: 4 h–6 d, depending on the presence of homologous models, cryo-EM map resolution and quality, secondary structure accuracy, size and complexity of the RNA molecules. The time is calculated based on a workstation with an 8-core Intel CPU and a Nvidia RTX2080Ti GPU or equivalent. The time required for de novo manual model building and refinement also heavily depend on user's expertise and experiences.

## Anticipated results

This protocol produces tens of nmol of target RNAs with homogeneous 5' and 3' ends that cotranscriptionally fold after IVT and can be purified by SEC that are directly ready for cryo-EM analysis (Fig. 3a). These RNAs can also undergo denaturing purification followed by RNA refolding. Optimal IVT and refolding conditions can be obtained initially by iterative screening of primary variables in these conditions using native PAGE (Fig. 3b–f and Extended Data Fig. 1). Additional variables may be extensively screened by high-throughput nanoDLS for further optimizations (Fig. 4).

Subsequently, optimal vitrification conditions of the properly folded RNAs are obtained by iterative optimizations of variables for grid types, glow discharging and vitrification apparatus. This is evaluated by cryo-EM visualization, preliminary data collection and processing to eventually reach the decision of large-scale data collection and processing to obtain RNA cryo-EM structures at moderate to near-atomic resolutions (Fig. 5). The resulting optimized conditions may be directly used for other RNAs of similar sizes or functions (e.g., ribozyme, riboswitch) or serve as starting points for optimizations of other RNAs.

Data processing is expected to resolve dynamic conformational changes and flexibility of RNAs associated to their functions at optimal resolutions, using the recently developed algorithms integrated in the most commonly used data processing suites (Figs. 6 and 7). RNA modeling that combines RNA structure prediction and automated and semi-automated modeling algorithms with manual curations enables generation of RNA atomic coordinates into the cryo-EM density maps at moderate to near-atomic resolution (Figs. 8–10). Successful application of the protocol will eventually yield all-atom RNA models to elucidate their functions and dynamics on a molecular level, and provide structural basis for applications such as RNA-targeted small molecule design.

**Data availability**

The data presented in this protocol were generated as part of refs. 14,25. The cryo-EM map of dimeric ATP-TTR-3 is deposited in the Electron Microscopy Data Bank with the accession code **EMD-37072**. All other data are available upon reasonable request from the corresponding author. Source data are provided with this paper.

Received: 4 August 2023; Accepted: 12 September 2024;

Published online: 15 November 2024

**References**

- Statello, L., Guo, C. J., Chen, L. L. & Huarte, M. Gene regulation by long non-coding RNAs and its biological functions. *Nat. Rev. Mol. Cell Biol.* **22**, 96–118 (2021).
- Cech, T. R. & Steitz, J. A. The noncoding RNA revolution—trashing old rules to forge new ones. *Cell* **157**, 77–94 (2014).
- Atkins, J. F., Gesteland, R. F. & Cech, T. *RNA Worlds: From Life's Origins to Diversity in Gene Regulation* (Cold Spring Harbor, 2011).
- Butcher, S. E. & Pyle, A. M. The molecular interactions that stabilize RNA tertiary structure: RNA motifs, patterns, and networks. *Acc. Chem. Res.* **44**, 1302–1311 (2011).
- Narlikar, G. J. & Herschlag, D. Mechanistic aspects of enzymatic catalysis: lessons from comparison of RNA and protein enzymes. *Annu. Rev. Biochem.* **66**, 19–59 (1997).
- Doherty, E. A. & Doudna, J. A. Ribozyme structures and mechanisms. *Annu. Rev. Biophys.* **30**, 457–475 (2001).
- Cech, T. R. Ribozymes, the first 20 years. *Biochem. Soc. Trans.* **30**, 1162–1166 (2002).
- Sherwood, A. V. & Henkin, T. M. Riboswitch-mediated gene regulation: novel RNA architectures dictate gene expression responses. *Annu. Rev. Microbiol.* **70**, 361–374 (2016).
- Roth, A. & Breaker, R. R. The structural and functional diversity of metabolite-binding riboswitches. *Annu. Rev. Biochem.* **78**, 305–334 (2009).
- Yang, Y., Harris, K. A., Widner, D. L. & Breaker, R. R. Structure of a bacterial OapB protein with its OLE RNA target gives insights into the architecture of the OLE ribonucleoprotein complex. *Proc. Natl. Acad. Sci. USA* **118**, e2020393118 (2021).
- Jaafar, Z. A. & Kieft, J. S. Viral RNA structure-based strategies to manipulate translation. *Nat. Rev. Microbiol.* **17**, 110–123 (2019).
- Mattick, J. S. et al. Long non-coding RNAs: definitions, functions, challenges and recommendations. *Nat. Rev. Mol. Cell Biol.* **24**, 430–447 (2023).
- Ding, J. et al. Visualizing RNA conformational and architectural heterogeneity in solution. *Nat. Commun.* **14**, 714 (2023).
- Luo, B. et al. Cryo-EM reveals dynamics of Tetrahymena group I intron self-splicing. *Nat. Catal.* **6**, 298–309 (2023).
- Bonilla, S. L., Sherlock, M. E., MacFadden, A. & Kieft, J. S. A viral RNA hijacks host machinery using dynamic conformational changes of a tRNA-like structure. *Science* **374**, 955–960 (2021).
- Ganser, L. R., Kelly, M. L., Herschlag, D. & Al-Hashimi, H. M. The roles of structural dynamics in the cellular functions of RNAs. *Nat. Rev. Mol. Cell Biol.* **20**, 474–489 (2019).
- Dethoff, E. A., Chugh, J., Mustoe, A. M. & Al-Hashimi, H. M. Functional complexity and regulation through RNA dynamics. *Nature* **482**, 322–330 (2012).
- Spitale, R. C. & Incarnato, D. Probing the dynamic RNA structurome and its functions. *Nat. Rev. Genet.* **24**, 178–196 (2023).
- Zhang, J. & Ferré-D'Amare, A. R. New molecular engineering approaches for crystallographic studies of large RNAs. *Curr. Opin. Struct. Biol.* **26**, 9–15 (2014).
- Spitale, R. C. & Wedekind, J. E. Exploring ribozyme conformational changes with X-ray crystallography. *Methods* **49**, 87–100 (2009).
- Zhang, H. & Keane, S. C. Advances that facilitate the study of large RNA structure and dynamics by nuclear magnetic resonance spectroscopy. *Wiley Interdiscip. Rev. RNA* **10**, e1541 (2019).
- Barnwal, R. P., Yang, F. & Varani, G. Applications of NMR to structure determination of RNAs large and small. *Arch. Biochem. Biophys.* **628**, 42–56 (2017).
- Ma, H., Jia, X., Zhang, K. & Su, Z. Cryo-EM advances in RNA structure determination. *Signal Transduct. Target Ther.* **7**, 58 (2022).
- Zhang, K. et al. Cryo-EM and antisense targeting of the 28-kDa frameshift stimulation element from the SARS-CoV-2 RNA genome. *Nat. Struct. Mol. Biol.* **28**, 747–754 (2021).
- Kappel, K. et al. Accelerated cryo-EM-guided determination of three-dimensional RNA-only structures. *Nat. Methods* **17**, 699–707 (2020).
- Wang, X., Terashi, G. & Kihara, D. CryoREAD: de novo structure modeling for nucleic acids in cryo-EM maps using deep learning. *Nat. Methods* **20**, 1739–1747 (2023).
- Ma, H. et al. Auto-DRRAFTER: automated RNA modeling based on cryo-EM density. *Methods Mol. Biol.* **2568**, 193–211 (2023).
- Biesiada, M., Purzycka, K. J., Szachniuk, M., Blazewicz, J. & Adamiak, R. W. in *RNA Structure Determination: Methods and Protocols* (eds Turner, D. H. & Mathews, D. H.) 199–215 (Humana, 2016).
- Boniecki, M. J. et al. SimRNA: a coarse-grained method for RNA folding simulations and 3D structure prediction. *Nucleic Acids Res.* **44**, e63 (2016).
- Li, T. et al. All-atom RNA structure determination from cryo-EM maps. *Nat. Biotechnol.* <https://doi.org/10.1038/s41587-024-02149-8> (2024).
- Jamali, K. et al. Automated model building and protein identification in cryo-EM maps. *Nature* **628**, 450–457 (2024).
- Liu, D., Thélot, F. A., Piccirilli, J. A., Liao, M. & Yin, P. Sub-3-Å cryo-EM structure of RNA enabled by engineered homomeric self-assembly. *Nat. Methods* **19**, 576–585 (2022).
- Sampedro Vallina, N., McRae, E. K. S., Hansen, B. K., Boussebayle, A. & Andersen, E. S. RNA origami scaffolds facilitate cryo-EM characterization of a Broccoli-Pepper aptamer FRET pair. *Nucleic Acids Res.* **51**, 4613–4624 (2023).
- Zhang, C. et al. Analysis of discrete local variability and structural covariance in macromolecular assemblies using cryo-EM and focused classification. *Ultramicroscopy* **203**, 170–180 (2019).
- Langeberg, C. J. & Kieft, J. S. A generalizable scaffold-based approach for structure determination of RNAs by cryo-EM. *Nucleic Acids Res.* **51**, e100 (2023).
- Berman, H. M. et al. The Protein Data Bank. *Nucleic Acids Res.* **28**, 235–242 (2000).
- The wwPDB Consortium. EMDB—the Electron Microscopy Data Bank. *Nucleic Acids Res.* **52**, D456–D465 (2024).
- Kretsch, R. C. et al. RNA target highlights in CASP15: evaluation of predicted models by structure providers. *Proteins* **91**, 1600–1615 (2023).
- Miao, Z. et al. RNA-Puzzles round IV: 3D structure predictions of four ribozymes and two aptamers. *RNA* **26**, 982–995 (2020).
- Weissenberger, G., Henderikx, R. J. M. & Peters, P. J. Understanding the invisible hands of sample preparation for cryo-EM. *Nat. Methods* **18**, 463–471 (2021).
- Stetefeld, J., McKenna, S. A. & Patel, T. R. Dynamic light scattering: a practical guide and applications in biomedical sciences. *Biophys. Rev.* **8**, 409–427 (2016).
- Batey, R. T. Advances in methods for native expression and purification of RNA for structural studies. *Curr. Opin. Struct. Biol.* **26**, 1–8 (2014).
- Chillón, I. et al. in *Methods in Enzymology* (eds Woodson, S. A. & Allain, F. H. T.) 3–37 (Academic, 2015).
- Uroda, T. et al. Visualizing the functional 3D shape and topography of long noncoding RNAs by single-particle atomic force microscopy and in-solution hydrodynamic techniques. *Nat. Protoc.* **15**, 2107–2139 (2020).
- Li, S., Zhang, K. & Chiu, W. in *RNA Structure and Dynamics* (eds Ding, J., Stagno, J. R. & Wang, Y.-X.) 179–192 (Humana, 2023).
- Passmore, L. A. & Russo, C. J. in *Methods in Enzymology* (ed. Crowther, R. A.) 51–86 (Academic, 2016).
- Wang, Y. et al. Cryo-EM analysis of Ebola virus nucleocapsid-like assembly. *STAR Protoc.* **3**, 101030 (2022).
- Thompson, R. F., Iadanza, M. G., Hesketh, E. L., Rawson, S. & Ranson, N. A. Collection, pre-processing and on-the-fly analysis of data for high-resolution, single-particle cryo-electron microscopy. *Nat. Protoc.* **14**, 100–118 (2019).
- Schürer, H., Lang, K., Schuster, J. & Mörl, M. A universal method to produce in vitro transcripts with homogeneous 3' ends. *Nucleic Acids Res.* **30**, e56 (2002).
- Kao, C., Zheng, M. & Rüdisser, S. A simple and efficient method to reduce nontemplated nucleotide addition at the 3' terminus of RNAs transcribed by T7 RNA polymerase. *RNA* **5**, 1268–1272 (1999).
- Benoit, C. in *RNA Processing: A Practical Approach* (eds Higgins, S. J. & Hames, B. D.) 1–29 (Oxford Univ. Press, 1994).
- Guillerez, J., Lopez, P. J., Proux, F., Launay, H. & Dreyfus, M. A mutation in T7 RNA polymerase that facilitates promoter clearance. *Proc. Natl. Acad. Sci. USA* **102**, 5958–5963 (2005).
- Kim, I., McKenna, S. A., Viani Puglisi, E. & Puglisi, J. D. Rapid purification of RNAs using fast performance liquid chromatography (FPLC). *RNA* **13**, 289–294 (2007).

54. Woodson, S. A. & Koculi, E. Analysis of RNA folding by native polyacrylamide gel electrophoresis. *Methods Enzymol.* **469**, 189–208 (2009).
55. Kalvari, I. et al. Rfam 14: expanded coverage of metagenomic, viral and microRNA families. *Nucleic Acids Res.* **49**, D192–D200 (2021).
56. Berman, H. M. et al. The nucleic acid database. A comprehensive relational database of three-dimensional structures of nucleic acids. *Biophys. J.* **63**, 751–759 (1992).
57. Biela, A. et al. The diverse structural modes of tRNA binding and recognition. *J. Biol. Chem.* **299**, 104966 (2023).
58. Hombach, S. & Kretz, M. Non-coding RNAs: classification, biology and functioning. *Adv. Exp. Med. Biol.* **937**, 3–17 (2016).
59. Klattenhoff, C. A. et al. Braveheart, a long noncoding RNA required for cardiovascular lineage commitment. *Cell* **152**, 570–583 (2013).
60. Kim, D. N. et al. Zinc-finger protein CNBP alters the 3-D structure of lncRNA Braveheart in solution. *Nat. Commun.* **11**, 148 (2020).
61. Uroda, T. et al. Conserved pseudoknots in lncRNA MEG3 are essential for stimulation of the p53 pathway. *Mol. Cell* **75**, 982–995 (2019).
62. Spokoini-Stern, R. et al. Visualizing the structure and motion of the long noncoding RNA HOTAIR. *RNA* **26**, 629–636 (2020).
63. Mogilyansky, E. & Rigoutsos, I. The miR-17/92 cluster: a comprehensive update on its genomics, genetics, functions and increasingly important and numerous roles in health and disease. *Cell Death Differ.* **20**, 1603–1614 (2013).
64. Chaulk, S. G. et al. Role of pri-miRNA tertiary structure in miR-17–92 miRNA biogenesis. *RNA Biol.* **8**, 1105–1114 (2011).
65. Yang, Y. et al. Structural basis of RNA conformational switching in the transcriptional regulator 7SK RNP. *Mol. Cell* **82**, 1724–1736 (2022).
66. Su, Z. et al. Cryo-EM structures of full-length Tetrahymena ribozyme at 3.1 Å resolution. *Nature* **596**, 603–607 (2021).
67. Zhang, K. et al. Cryo-EM structure of a 40 kDa SAM-IV riboswitch RNA at 3.7 Å resolution. *Nat. Commun.* **10**, 5511 (2019).
68. Warner, K. D., Hajdin, C. E. & Weeks, K. M. Principles for targeting RNA with drug-like small molecules. *Nat. Rev. Drug Discov.* **17**, 547–558 (2018).
69. Liu, F., Somarowthu, S. & Pyle, A. M. Visualizing the secondary and tertiary architectural domains of lncRNA RepA. *Nat. Chem. Biol.* **13**, 282–289 (2017).
70. Aguilar, R. et al. Targeting Xist with compounds that disrupt RNA structure and X inactivation. *Nature* **604**, 160–166 (2022).
71. Ratni, H. et al. Discovery of risdiplam, a selective survival of motor neuron-2 (SMN2) gene splicing modifier for the treatment of spinal muscular atrophy (SMA). *J. Med. Chem.* **61**, 6501–6517 (2018).
72. Campagne, S. et al. Structural basis of a small molecule targeting RNA for a specific splicing correction. *Nat. Chem. Biol.* **15**, 1191–1198 (2019).
73. Petrov, A., Tsa, A. & Puglisi, J. D. in *Methods in Enzymology* (ed. Lorsch, J.) 301–313 (Academic, 2013).
74. Edwards, G. B., Muthurajan, U. M., Bowerman, S. & Luger, K. Analytical ultracentrifugation (AUC): an overview of the application of fluorescence and absorbance AUC to the study of biological macromolecules. *Curr. Protoc. Mol. Biol.* **133**, e131 (2020).
75. Wei, B., Goyon, A. & Zhang, K. Analysis of therapeutic nucleic acids by capillary electrophoresis. *J. Pharm. Biomed. Anal.* **219**, 114928 (2022).
76. Li, B., Cao, Y., Westhof, E. & Miao, Z. Advances in RNA 3D structure modeling using experimental data. *Front. Genet.* **11**, 574485 (2020).
77. Reyes, F. E., Garst, A. D. & Batey, R. T. Strategies in RNA crystallography. *Methods Enzymol.* **469**, 119–139 (2009).
78. Golden, B. L. Preparation and crystallization of RNA. *Methods Mol. Biol.* **363**, 239–257 (2007).
79. Marušić, M., Schlagnitzweit, J. & Petzold, K. RNA dynamics by NMR spectroscopy. *ChemBiochem* **20**, 2685–2710 (2019).
80. Getz, M., Sun, X., Casiano-Negróni, A., Zhang, Q. & Al-Hashimi, H. M. NMR studies of RNA dynamics and structural plasticity using NMR residual dipolar couplings. *Biopolymers* **86**, 384–402 (2007).
81. Kotar, A., Foley, H. N., Baughman, K. M. & Keane, S. C. Advanced approaches for elucidating structures of large RNAs using NMR spectroscopy and complementary methods. *Methods* **183**, 93–107 (2020).
82. Keane, S. C. et al. NMR detection of intermolecular interaction sites in the dimeric 5'-leader of the HIV-1 genome. *Proc. Natl. Acad. Sci. USA* **113**, 13033–13038 (2016).
83. Keane, S. C. et al. RNA structure. Structure of the HIV-1 RNA packaging signal. *Science* **348**, 917–921 (2015).
84. Koch, M. H. J., Vachette, P. & Svergun, D. I. Small-angle scattering: a view on the properties, structures and structural changes of biological macromolecules in solution. *Q. Rev. Biophys.* **36**, 147–227 (2003).
85. Byron, O. & Gilbert, R. J. C. Neutron scattering: good news for biotechnology. *Curr. Opin. Biotechnol.* **11**, 72–80 (2000).
86. Nogales, E. & Mahamid, J. Bridging structural and cell biology with cryo-electron microscopy. *Nature* **628**, 47–56 (2024).
87. Tacke, S. et al. A streamlined workflow for automated cryo focused ion beam milling. *J. Struct. Biol.* **213**, 107743 (2021).
88. Zachs, T. et al. Fully automated, sequential focused ion beam milling for cryo-electron tomography. *eLife* **9**, e52286 (2020).
89. Wan, Y., Kertesz, M., Spitaler, R. C., Segal, E. & Chang, H. Y. Understanding the transcriptome through RNA structure. *Nat. Rev. Genet.* **12**, 641–655 (2011).
90. Cruz, J. A. & Westhof, E. The dynamic landscapes of RNA architecture. *Cell* **136**, 604–609 (2009).
91. Nakamura, A. et al. Fast and automated protein–DNA/RNA macromolecular complex modeling from cryo-EM maps. *Brief. Bioinform.* **24**, bbac632 (2023).
92. Zhang, J., Fei, Y., Sun, L. & Zhang, Q. C. Advances and opportunities in RNA structure experimental determination and computational modeling. *Nat. Methods* **19**, 1193–1207 (2022).
93. Deng, J. et al. RNA structure determination: from 2D to 3D. *Fundam. Res.* **3**, 727–737 (2023).
94. Wayment-Steele, H. K. et al. RNA secondary structure packages evaluated and improved by high-throughput experiments. *Nat. Methods* **19**, 1234–1242 (2022).
95. Turner, D. H. & Mathews, D. H. (eds) *RNA Structure Determination: Methods and Protocols* (Humana, 2016).
96. Walker, S. C., Avis, J. M. & Conn, G. L. General plasmids for producing RNA in vitro transcripts with homogeneous ends. *Nucleic Acids Res.* **31**, e82 (2003).
97. Kao, C., Rüdisser, S. & Zheng, M. A simple and efficient method to transcribe RNAs with reduced 3' heterogeneity. *Methods* **23**, 201–205 (2001).
98. McRae, E. K. S. et al. Structure, folding and flexibility of co-transcriptional RNA origami. *Nat. Nanotechnol.* **18**, 808–817 (2023).
99. Sampedro Vallina, N., McRae, E. K. S., Geary, C. & Andersen, E. S. An RNA paranemic crossover triangle as a 3D module for cotranscriptional nanoassembly. *Small* **19**, e2204651 (2023).
100. Bonilla, S. L., Vicens, Q. & Kieft, J. S. Cryo-EM reveals an entangled kinetic trap in the folding of a catalytic RNA. *Sci. Adv.* **8**, eabq4144 (2022).
101. Li, S. et al. Topological crossing in the misfolded Tetrahymena ribozyme resolved by cryo-EM. *Proc. Natl. Acad. Sci. USA* **119**, e2209146119 (2022).
102. Irobaliava, R. N. et al. Structural diversity of supercoiled DNA. *Nat. Commun.* **6**, 8440 (2015).
103. Wu, S., Armacé, J. P. & Cheng, Y. Single-particle cryo-EM data acquisition by using direct electron detection camera. *Microscopy* **65**, 35–41 (2016).
104. Baxter, W. T., Grassucci, R. A., Gao, H. & Frank, J. Determination of signal-to-noise ratios and spectral SNRs in cryo-EM low-dose imaging of molecules. *J. Struct. Biol.* **166**, 126–132 (2009).
105. Noble, A. J. et al. Routine single particle CryoEM sample and grid characterization by tomography. *eLife* **7**, e34257 (2018).
106. Ognjenović, J., Grisshammer, R. & Subramaniam, S. Frontiers in cryo electron microscopy of complex macromolecular assemblies. *Annu. Rev. Biomed. Eng.* **21**, 395–415 (2019).
107. Drulyte, I. et al. Approaches to altering particle distributions in cryo-electron microscopy sample preparation. *Acta Crystallogr. D* **74**, 560–571 (2018).
108. Li, B., Zhu, D., Shi, H. & Zhang, X. Effect of charge on protein preferred orientation at the air–water interface in cryo-electron microscopy. *J. Struct. Biol.* **213**, 107783 (2021).
109. Glaeser, R. M. & Han, B. G. Opinion: hazards faced by macromolecules when confined to thin aqueous films. *Biophys. Rep.* **3**, 1–7 (2017).
110. Glaeser, R. M. Proteins, interfaces, and cryo-EM grids. *Curr. Opin. Colloid Interface Sci.* **34**, 1–8 (2018).
111. Russo, C. J. & Passmore, L. A. Electron microscopy: ultrastable gold substrates for electron cryomicroscopy. *Science* **346**, 1377–1380 (2014).
112. Naydenova, K., Jia, P. & Russo, C. J. Cryo-EM with sub-1 Å specimen movement. *Science* **370**, 223–226 (2020).
113. Huang, X. et al. Amorphous nickel titanium alloy film: a new choice for cryo electron microscopy sample preparation. *Prog. Biophys. Mol. Biol.* **156**, 3–13 (2020).
114. Williams, R. C. & Glaeser, R. M. Ultrathin carbon support films for electron microscopy. *Science* **175**, 1000–1001 (1972).
115. Grassucci, R. A., Taylor, D. J. & Frank, J. Preparation of macromolecular complexes for cryo-electron microscopy. *Nat. Protoc.* **2**, 3239–3246 (2007).
116. Pantelic, R. S., Meyer, J. C., Kaiser, U. & Stahlberg, H. The application of graphene as a sample support in transmission electron microscopy. *Solid State Commun.* **152**, 1375–1382 (2012).
117. Russo, C. J. & Passmore, L. A. Controlling protein adsorption on graphene for cryo-EM using low-energy hydrogen plasmas. *Nat. Methods* **11**, 649–652 (2014).
118. Han, Y. et al. High-yield monolayer graphene grids for near-atomic resolution cryoelectron microscopy. *Proc. Natl. Acad. Sci. USA* **117**, 1009–1014 (2020).
119. Xu, J. et al. Graphene sandwich-based biological specimen preparation for cryo-EM analysis. *Proc. Natl. Acad. Sci. USA* **121**, e2309384121 (2024).
120. Pantelic, R. S., Meyer, J. C., Kaiser, U., Baumeister, W. & Plitzko, J. M. Graphene oxide: a substrate for optimizing preparations of frozen-hydrated samples. *J. Struct. Biol.* **170**, 152–156 (2010).
121. Palovcak, E. et al. A simple and robust procedure for preparing graphene-oxide cryo-EM grids. *J. Struct. Biol.* **204**, 80–84 (2018).
122. Liu, N. et al. Reduced graphene oxide membrane as supporting film for high-resolution cryo-EM. *Biophys. Rep.* **7**, 227–238 (2021).
123. Wang, L., Ounjai, P. & Sigworth, F. J. Streptavidin crystals as nanostructured supports and image-calibration references for cryo-EM data collection. *J. Struct. Biol.* **164**, 190–198 (2008).
124. Han, B. G., Watson, Z., Cate, J. H. D. & Glaeser, R. M. Monolayer-crystal streptavidin support films provide an internal standard of cryo-EM image quality. *J. Struct. Biol.* **200**, 307–313 (2017).

125. Fan, H. et al. A cryo-electron microscopy support film formed by 2D crystals of hydrophobin HFBI. *Nat. Commun.* **12**, 7257 (2021).
126. da Fonseca, P. C. & Morris, E. P. Cryo-EM reveals the conformation of a substrate analogue in the human 20S proteasome core. *Nat. Commun.* **6**, 7573 (2015).
127. Dubochet, J. et al. Cryo-electron microscopy of vitrified specimens. *Q. Rev. Biophys.* **21**, 129–228 (1988).
128. Dandey, V. P. et al. Spotiton: new features and applications. *J. Struct. Biol.* **202**, 161–169 (2018).
129. Feng, X. et al. A fast and effective microfluidic spraying-plunging method for high-resolution single-particle cryo-EM. *Structure* **25**, 663–670.e663 (2017).
130. Rubinstein, J. L. et al. Shake-it-off: a simple ultrasonic cryo-EM specimen-preparation device. *Acta Crystallogr. D* **75**, 1063–1070 (2019).
131. Ashtiani, D. et al. Delivery of femtolitre droplets using surface acoustic wave based atomisation for cryo-EM grid preparation. *J. Struct. Biol.* **203**, 94–101 (2018).
132. Ravelli, R. B. G. et al. Cryo-EM structures from sub-nl volumes using pin-printing and jet vitrification. *Nat. Commun.* **11**, 2563 (2020).
133. Schmidli, C. et al. Microfluidic protein isolation and sample preparation for high-resolution cryo-EM. *Proc. Natl. Acad. Sci. USA* **116**, 15007–15012 (2019).
134. Koning, R. I. et al. Automated vitrification of cryo-EM samples with controllable sample thickness using suction and real-time optical inspection. *Nat. Commun.* **13**, 2985 (2022).
135. Rice, W. J. et al. Routine determination of ice thickness for cryo-EM grids. *J. Struct. Biol.* **204**, 38–44 (2018).
136. Hohle, M. M. et al. Ice thickness monitoring for cryo-EM grids by interferometry imaging. *Sci. Rep.* **12**, 15330 (2022).
137. Vargas, J. et al. Foil-hole and data image quality assessment in 3DEM: towards high-throughput image acquisition in the electron microscope. *J. Struct. Biol.* **196**, 515–524 (2016).
138. Last, M. G. F., Voortman, L. M. & Sharp, T. H. Measuring cryo-TEM sample thickness using reflected light microscopy and machine learning. *J. Struct. Biol.* **215**, 107965 (2023).
139. Yokoyama, Y. et al. Development of a deep learning-based method to identify “good” regions of a cryo-electron microscopy grid. *Biophys. Rev.* **12**, 349–354 (2020).
140. Angert, I., Burmester, C., Dinges, C., Rose, H. & Schröder, R. R. Elastic and inelastic scattering cross-sections of amorphous layers of carbon and vitrified ice. *Ultramicroscopy* **63**, 181–192 (1996).
141. Feja, B. & Abeij, U. Determination of the inelastic mean free path of electrons in vitrified ice layers for on-line thickness measurements by zero-loss imaging. *J. Microsc.* **193**, 15–19 (1999).
142. Brown, H. G. & Hanssen, E. MeasureIce: accessible on-the-fly measurement of ice thickness in cryo-electron microscopy. *Commun. Biol.* **5**, 817 (2022).
143. Rheinberger, J., Oostergetel, G., Resch, G. P. & Paulino, C. Optimized cryo-EM data-acquisition workflow by sample-thickness determination. *Acta Crystallogr. D* **77**, 565–571 (2021).
144. Mastronarde, D. N. Automated electron microscope tomography using robust prediction of specimen movements. *J. Struct. Biol.* **152**, 36–51 (2005).
145. Carragher, B. et al. Leginon: an automated system for acquisition of images from vitreous ice specimens. *J. Struct. Biol.* **132**, 33–45 (2000).
146. Mendez, J. H., Chua, E. Y. D., Paraan, M., Potter, C. S. & Carragher, B. Automated pipelines for rapid evaluation during cryo-EM data acquisition. *Curr. Opin. Struct. Biol.* **83**, 102729 (2023).
147. Vilas, J. L., Carazo, J. M. & Sorzano, C. O. S. Emerging themes in cryoEM—single particle analysis image processing. *Chem. Rev.* **122**, 13915–13951 (2022).
148. Bepler, T., Kelley, K., Noble, A. J. & Berger, B. Topaz-Denoise: general deep denoising models for cryoEM and cryoET. *Nat. Commun.* **11**, 5208 (2020).
149. Bepler, T. et al. Positive-unlabeled convolutional neural networks for particle picking in cryo-electron micrographs. *Nat. Methods* **16**, 1153–1160 (2019).
150. Tegunov, D., Xue, L., Dienemann, C., Cramer, P. & Mahamid, J. Multi-particle cryo-EM refinement with M visualizes ribosome-antibiotic complex at 3.5 Å in cells. *Nat. Methods* **18**, 186–193 (2021).
151. Chen, M. et al. Convolutional neural networks for automated annotation of cellular cryo-electron tomograms. *Nat. Methods* **14**, 983–985 (2017).
152. Wagner, T. et al. SPHIRE-crYOLO is a fast and accurate fully automated particle picker for cryo-EM. *Commun. Biol.* **2**, 218 (2019).
153. Al-Azzawi, A. et al. DeepCryoPicker: fully automated deep neural network for single protein particle picking in cryo-EM. *BMC Bioinformatics* **21**, 509 (2020).
154. Nguyen, N. P., Ersøy, I., Gotberg, J., Bunyak, F. & White, T. A. DRPnet: automated particle picking in cryo-electron micrographs using deep regression. *BMC Bioinformatics* **22**, 55 (2021).
155. Zhang, J. et al. PIXER: an automated particle-selection method based on segmentation using a deep neural network. *BMC Bioinformatics* **20**, 41 (2019).
156. Punjani, A. & Fleet, D. J. 3D variability analysis: resolving continuous flexibility and discrete heterogeneity from single particle cryo-EM. *J. Struct. Biol.* **213**, 107702 (2021).
157. Punjani, A. & Fleet, D. J. 3DFlex: determining structure and motion of flexible proteins from cryo-EM. *Nat. Methods* **20**, 860–870 (2023).
158. Zhong, E. D., Bepler, T., Berger, B. & Davis, J. H. CryoDRGN: reconstruction of heterogeneous cryo-EM structures using neural networks. *Nat. Methods* **18**, 176–185 (2021).
159. Dashti, A. et al. Retrieving functional pathways of biomolecules from single-particle snapshots. *Nat. Commun.* **11**, 4734 (2020).
160. Chen, M. & Ludtke, S. J. Deep learning-based mixed-dimensional Gaussian mixture model for characterizing variability in cryo-EM. *Nat. Methods* **18**, 930–936 (2021).
161. Chen, M., Schmid, M. F. & Chiu, W. Improving resolution and resolvability of single-particle cryoEM structures using Gaussian mixture models. *Nat. Methods* **21**, 37–40 (2024).
162. Nakane, T., Kimanis, D., Lindahl, E. & Scheres, S. H. W. Characterisation of molecular motions in cryo-EM single-particle data by multi-body refinement in RELION. *eLife* **7**, e36861 (2018).
163. Tang, G. et al. EMAN2: an extensible image processing suite for electron microscopy. *J. Struct. Biol.* **157**, 38–46 (2007).
164. Zivanov, J. et al. A Bayesian approach to single-particle electron cryo-tomography in RELION-4.0. *eLife* **11**, e83724 (2022).
165. Punjani, A., Rubinstein, J. L., Fleet, D. J. & Brubaker, M. A. cryoSPARC: algorithms for rapid unsupervised cryo-EM structure determination. *Nat. Methods* **14**, 290–296 (2017).
166. Emsley, P., Lohkamp, B., Scott, W. G. & Cowtan, K. Features and development of Coot. *Acta Crystallogr. D* **66**, 486–501 (2010).
167. Terwilliger, T. C. et al. Iterative model building, structure refinement and density modification with the PHENIX AutoBuild wizard. *Acta Crystallogr. D* **64**, 61–69 (2008).
168. Terashi, G., Wang, X., Maddhuri Venkata Subramanya, S. R., Tesmer, J. J. G. & Kihara, D. Residue-wise local quality estimation for protein models from cryo-EM maps. *Nat. Methods* **19**, 1116–1125 (2022).
169. Croll, T. I. ISOLDE: a physically realistic environment for model building into low-resolution electron-density maps. *Acta Crystallogr. D* **74**, 519–530 (2018).
170. Terwilliger, T. C., Adams, P. D., Afonine, P. V. & Sobolev, O. V. Cryo-EM map interpretation and protein model-building using iterative map segmentation. *Protein Sci.* **29**, 87–99 (2020).
171. Eastman, P. et al. OpenMM 7: rapid development of high performance algorithms for molecular dynamics. *PLoS Comput. Biol.* **13**, e1005659 (2017).
172. Ou, X., Zhang, Y., Xiong, Y. & Xiao, Y. Advances in RNA 3D structure prediction. *J. Chem. Inf. Model.* **62**, 5862–5874 (2022).
173. Stasiewicz, J., Mukherjee, S., Nithin, C. & Bujnicki, J. M. QRNAS: software tool for refinement of nucleic acid structures. *BMC Struct. Biol.* **19**, 5 (2019).
174. Biesiada, M., Pacholska-Wieczorek, K., Adamia, R. W. & Purzycka, K. J. RNAComposer and RNA 3D structure prediction for nanotechnology. *Methods* **103**, 120–127 (2016).
175. Grassucci, R. A., Taylor, D. & Frank, J. Visualization of macromolecular complexes using cryo-electron microscopy with FEI Tecnai transmission electron microscopes. *Nat. Protoc.* **3**, 330–339 (2008).
176. Tan, Y. Z. et al. Addressing preferred specimen orientation in single-particle cryo-EM through tilting. *Nat. Methods* **14**, 793–796 (2017).
177. Li, X. et al. Electron counting and beam-induced motion correction enable near-atomic-resolution single-particle cryo-EM. *Nat. Methods* **10**, 584–590 (2013).
178. Zheng, S. Q. et al. MotionCor2: anisotropic correction of beam-induced motion for improved cryo-electron microscopy. *Nat. Methods* **14**, 331–332 (2017).
179. Tegunov, D. & Cramer, P. Real-time cryo-electron microscopy data preprocessing with Warp. *Nat. Methods* **16**, 1146–1152 (2019).
180. Grant, T., Rohou, A. & Grigorieff, N. cisTEM, user-friendly software for single-particle image processing. *eLife* **7**, e35383 (2018).
181. Rohou, A. & Grigorieff, N. CTFFIND4: fast and accurate defocus estimation from electron micrographs. *J. Struct. Biol.* **192**, 216–221 (2015).
182. Elfrich, J., Kong, L., Zottig, X. & Grigorieff, N. CTFFIND5 provides improved insight into quality, tilt and thickness of TEM samples. *eLife* **13**, RP9727 (2024).
183. Zhang, K. Gctf: real-time CTF determination and correction. *J. Struct. Biol.* **193**, 1–12 (2016).
184. Voss, N. R., Yoshioka, C. K., Radermacher, M., Potter, C. S. & Carragher, B. DoG Picker and TiltPicker: software tools to facilitate particle selection in single particle electron microscopy. *J. Struct. Biol.* **166**, 205–213 (2009).
185. Zhang, K. et al. Cryo-EM reveals how human cytoplasmic dynein is auto-inhibited and activated. *Cell* **169**, 1303–1314.e1318 (2017).
186. Frank, J. & Wagenknecht, T. Automatic selection of molecular images from electron micrographs. *Ultramicroscopy* **12**, 169–175 (1983).
187. Scheres, S. H. W. Semi-automated selection of cryo-EM particles in RELION-1.3. *J. Struct. Biol.* **189**, 114–122 (2015).
188. Chen, J. Z. & Grigorieff, N. SIGNATURE: a single-particle selection system for molecular electron microscopy. *J. Struct. Biol.* **157**, 168–173 (2007).
189. Huang, Z. & Penczek, P. A. Application of template matching technique to particle detection in electron micrographs. *J. Struct. Biol.* **145**, 29–40 (2004).
190. Roseman, A. M. FindEM—a fast, efficient program for automatic selection of particles from electron micrographs. *J. Struct. Biol.* **145**, 91–99 (2004).
191. Ogura, T. & Sato, C. An automatic particle pickup method using a neural network applicable to low-contrast electron micrographs. *J. Struct. Biol.* **136**, 227–238 (2001).
192. Punjani, A., Zhang, H. & Fleet, D. J. Non-uniform refinement: adaptive regularization improves single-particle cryo-EM reconstruction. *Nat. Methods* **17**, 1214–1221 (2020).
193. Pettersen, E. F. et al. UCSF Chimera—a visualization system for exploratory research and analysis. *J. Comput. Chem.* **25**, 1605–1612 (2004).
194. Magnus, M., Boniecki, M. J., Dawson, W. & Bujnicki, J. M. SimRNAweb: a web server for RNA 3D structure modeling with optional restraints. *Nucleic Acids Res.* **44**, W315–W319 (2016).
195. Watkins, A. M., Rangan, R. & Das, R. FARFAR2: improved de novo rosetta prediction of complex global RNA folds. *Structure* **28**, 963–976.e966 (2020).

196. Schwab, J., Kimanis, D., Burt, A., Dendooven, T. & Scheres, S. H. W. DynaMight: estimating molecular motions with improved reconstruction from cryo-EM images. *Nat. Methods* <https://doi.org/10.1038/s41592-024-02377-5> (2024).
197. Afonine, P. V. et al. Real-space refinement in PHENIX for cryo-EM and crystallography. *Acta Crystallogr. D* **74**, 531–544 (2018).
198. Saenger, W. *Principles of Nucleic Acid Structure* **1**, 1–458 (Springer, 1984).
199. Chou, F. C., Echols, N., Terwilliger, T. C. & Das, R. RNA structure refinement using the ERRASER-Phenix pipeline. *Methods Mol. Biol.* **1320**, 269–282 (2016).
200. Ding, J. et al. Capturing heterogeneous conformers of cobalamin riboswitch by cryo-EM. *Nucleic Acids Res.* **51**, 9952–9960 (2023).
201. Haack, D. B., Rudolfs, B., Jin, S., Weeks, K. M. & Toor, N. Scaffold-enabled high-resolution cryo-EM structure determination of RNA. Preprint at *bioRxiv* <https://doi.org/10.1101/2024.06.10.598011> (2024).
202. Zhang, K. et al. Structure of the 30 kDa HIV-1 RNA dimerization signal by a hybrid cryo-EM, NMR, and molecular dynamics approach. *Structure* **26**, 490–498.e493 (2018).
203. Li, S. et al. Structural basis of amino acid surveillance by higher-order tRNA–mRNA interactions. *Nat. Struct. Mol. Biol.* **26**, 1094–1105 (2019).
204. Jia, X. et al. Cryo-EM-guided engineering of T-box-tRNA modules with enhanced selectivity and sensitivity in translational regulation. Preprint at *bioRxiv* <https://doi.org/10.1101/2023.02.28.530422> (2023).
205. McRae, E. K. S. et al. Cryo-EM structure and functional landscape of an RNA polymerase ribozyme. *Proc. Natl Acad. Sci. USA* **121**, e2313332121 (2024).
206. Kristoffersen, E. L., McRae, E. K., Sørensen, N. R., Holliger, P. & Andersen, E. S. Roles of dimeric intermediates in RNA-catalyzed rolling circle synthesis. Preprint at *bioRxiv* <https://doi.org/10.1101/2024.05.14.594117> (2024).
207. Wang, L. et al. Structural basis of circularly permuted group II intron self-splicing. Preprint at *Research Square* <https://doi.org/10.21203/rs.3.rs-3888028/v1> (2024).
208. Langeberg, C. J., Szucs, M. J., Sherlock, M. E., Vicens, Q. & Kieft, J. S. Tick-borne flavivirus exoribonuclease-resistant RNAs contain a ‘double loop’ structure. Preprint at *bioRxiv* <https://doi.org/10.1101/2024.04.14.589432> (2024).
209. Liu, Z. X. et al. Hydrolytic endonucleolytic ribozyme (HYER) is programmable for sequence-specific DNA cleavage. *Science* **383**, eadh4859 (2024).
210. Valina, N. S., McRae, E. K. S., Geary, C. & Andersen, E. S. An RNA origami robot that traps and releases a fluorescent aptamer. *Sci. Adv.* **10**, eadk1250 (2024).
211. Zhang, X., Li, S., Pintilie, G., Palo, M. Z. & Zhang, K. Snapshots of the first-step self-splicing of *Tetrahymena* ribozyme revealed by cryo-EM. *Nucleic Acids Res.* **51**, 1317–1325 (2023).
212. Li, S., Palo, M. Z., Zhang, X., Pintilie, G. & Zhang, K. Snapshots of the second-step self-splicing of *Tetrahymena* ribozyme revealed by cryo-EM. *Nat. Commun.* **14**, 1294 (2023).
213. Kretsch, R. C. et al. Tertiary folds of the SL5 RNA from the 5' proximal region of SARS-CoV-2 and related coronaviruses. *Proc. Natl Acad. Sci. USA* **121**, e2320493121 (2024).
214. de Moura, T. R. et al. Conserved structures and dynamics in 5'-proximal regions of Betacoronavirus RNA genomes. *Nucleic Acids Res.* **52**, 3419–3432 (2024).
215. Torabi, S. F. et al. Structural analyses of an RNA stability element interacting with poly(A). *Proc. Natl Acad. Sci. USA* **118**, e2026656118 (2021).
216. Liu, N. et al. Bioactive functionalized monolayer graphene for high-resolution cryo-electron microscopy. *J. Am. Chem. Soc.* **141**, 4016–4025 (2019).
217. Wang, F. et al. Amino and PEG-amino graphene oxide grids enrich and protect samples for high-resolution single particle cryo-electron microscopy. *J. Struct. Biol.* **209**, 107437 (2020).
218. Benjamin, C. J. et al. Selective capture of histidine-tagged proteins from cell lysates using TEM grids modified with NTA–graphene oxide. *Sci. Rep.* **6**, 32500 (2016).
219. Yoshioka, C., Carragher, B. & Potter, C. S. Cryomesh: a new substrate for cryo-electron microscopy. *Microsc. Microanal.* **16**, 43–53 (2010).
220. Kolev, N. G., Hartland, E. I. & Huber, P. W. A manganese-dependent ribozyme in the 3'-untranslated region of *Xenopus* Vg1 mRNA. *Nucleic Acids Res.* **36**, 5530–5539 (2008).
221. Satyanarayana, T., Gowda, S., Ayllón, M. A., Albiach-Martí, M. R. & Dawson, W. O. Mutational analysis of the replication signals in the 3'-nontranslated region of citrus tristeza virus. *Virology* **300**, 140–152 (2002).

**Acknowledgements**

Cryo-EM data were collected on Can Cong at State Key Laboratory of Biotherapy West China Cryo-EM Center and processed at State Key Laboratory of Biotherapy Duyu High Performance Computing Center of West China Hospital. This work was supported by National Key Research and Development Program of China (2022YFC2303700), Natural Science Foundation of China (32222040, 32070049, 32300030 and 81970936), and the 1.3.5 Project for Disciplines of Excellence of West China Hospital (ZYC21006). The work in the Glatt lab was supported by the European Research Council under the European Union’s Horizon 2020 research and innovation program (grant agreement no. 101001394 to S.G.).

**Author contributions**

X.C., L.W., J.X., J.S.N., B.L., C.Z. and G.J. performed experiments, X.C., L.W., J.X., D.H., Y.Y., Z.S., J.S.N. and S.G. prepared the manuscript with contributions from all authors.

**Competing interests**

The authors declare no competing interests.

**Additional information**

**Extended data** is available for this paper at <https://doi.org/10.1038/s41596-024-01072-1>.

**Supplementary information** is available for this paper at <https://doi.org/10.1038/s41596-024-01072-1>.

**Correspondence and requests for materials** should be addressed to Zhaoming Su.

**Peer review information** *Nature Protocols* thanks Marco Marcia and the other, anonymous, reviewer(s) for their contribution to the peer review of their work.

**Reprints and permissions information** is available at [www.nature.com/reprints](http://www.nature.com/reprints).

**Publisher's note** Springer Nature remains neutral with regard to jurisdictional claims in published maps and institutional affiliations.

Springer Nature or its licensor (e.g. a society or other partner) holds exclusive rights to this article under a publishing agreement with the author(s) or other rightsholder(s); author self-archiving of the accepted manuscript version of this article is solely governed by the terms of such publishing agreement and applicable law.

**Related links****Key references using this protocol**

Kappel, K. et al. *Nat. Methods* **17**, 699–707 (2020): <https://doi.org/10.1038/s41592-020-0878-9>  
Luo, B. et al. *Nat. Catal.* **6**, 298–309 (2023): <https://doi.org/10.1038/s41929-023-00934-3>

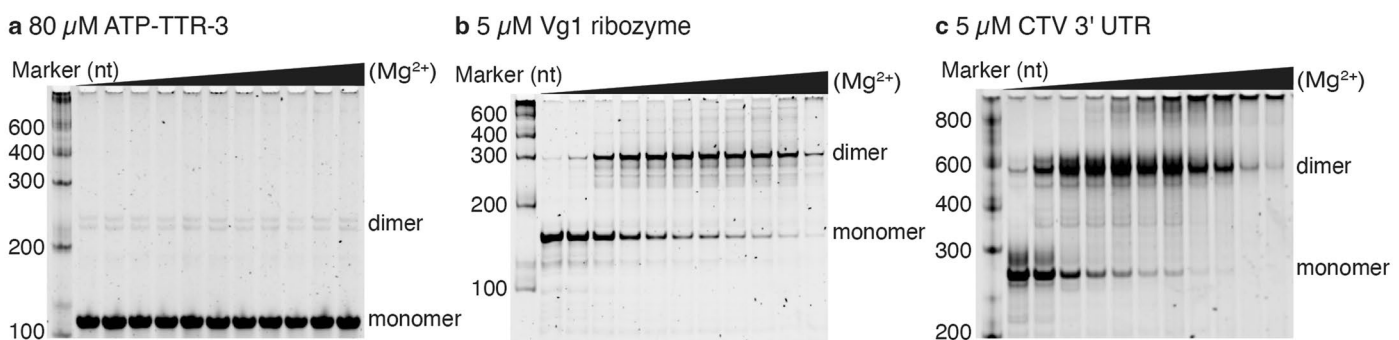
**Key data used in this protocol**

Su, Z. et al. *Nature* **596**, 603–607 (2021): <https://doi.org/10.1038/s41586-021-03803-w>

© Springer Nature Limited 2024

## Protocol

### Detection of the effect of increased Mg<sup>2+</sup> concentration on RNA oligomerization using native PAGE (Steps 10-12)

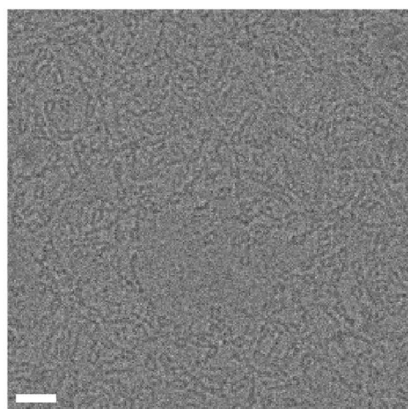


**Extended Data Fig. 1 | Detection of the effect of increased Mg<sup>2+</sup> concentration on RNA oligomerization using native PAGE.** This figure relates to Steps 10-12. (a–c) Native PAGE of (a) ATP-TTR-3, (b) Vg1 ribozyme, and (c) CTV 3' UTR.

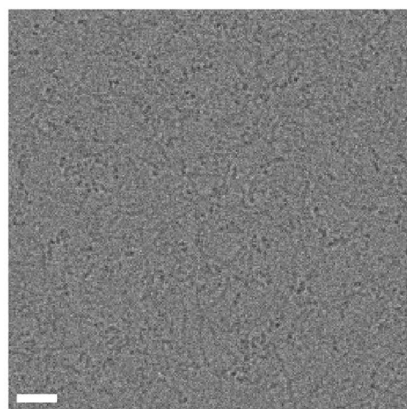
# Protocol

ATP-TTR-3 freezing conditions on different types of grids visualized under cryo-EM (Steps 19-26)

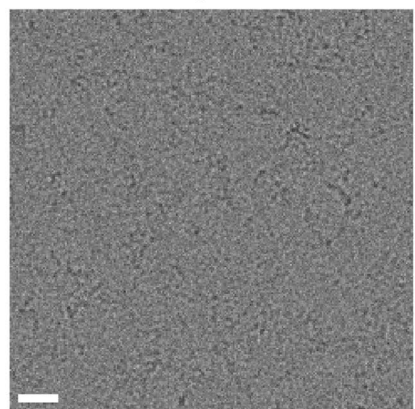
**a** 200-mesh Cu R2/1 Quantifoil



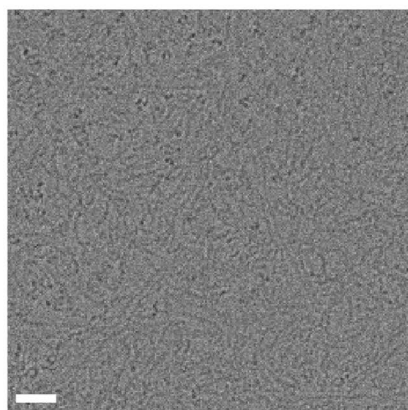
**b** 200-mesh Cu R1.2/1.3 Quantifoil



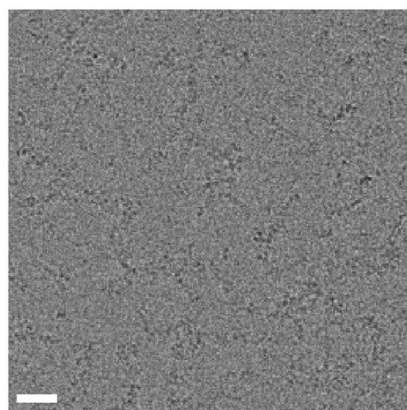
**c** 300-mesh ANTcryo R1.2/1.3 Nanodim



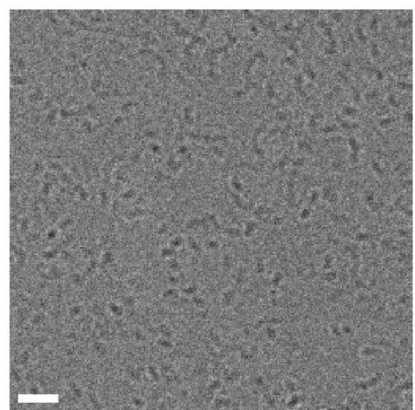
**d** 200-mesh Au R2/1 Quantifoil



**e** 200-mesh Au R1.2/1.3 Quantifoil



**f** 300-mesh Au-flat R1.2/1.3 Protochips

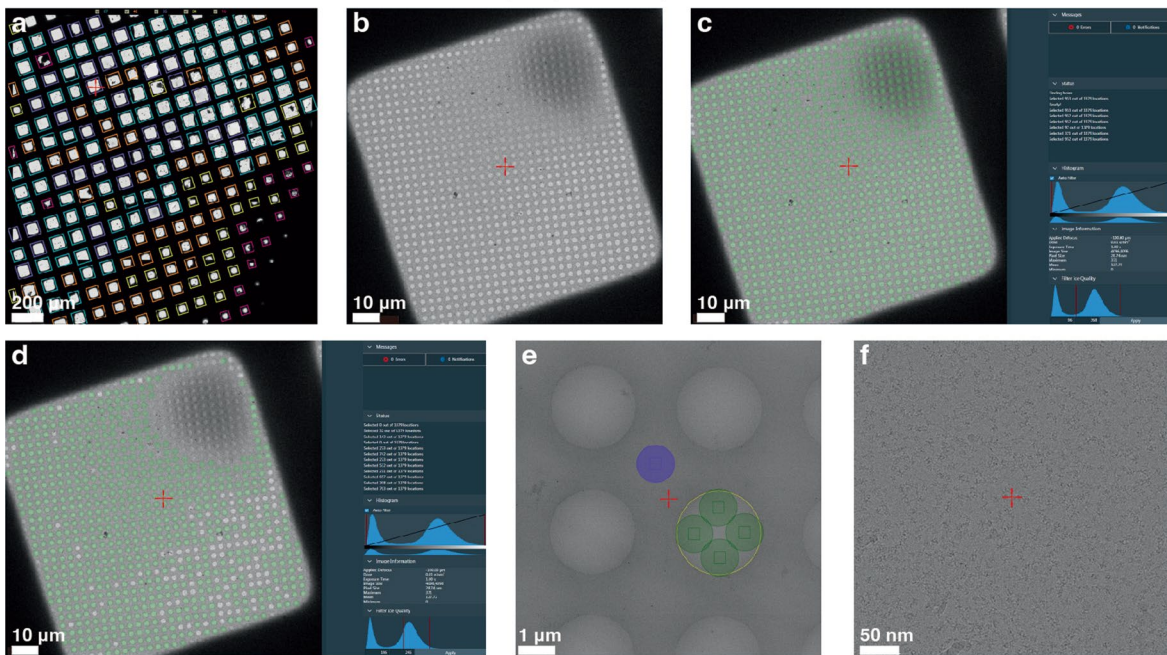


**Extended Data Fig. 2 | ATP-TTR-3 freezing conditions on different types of grids visualized under cryo-EM.** This figure relates to Steps 19-26. (a-f) Cryo-EM micrographs of RNA with CTAB detergent frozen on (a) 200-mesh Cu R2/1

Quantifoil, (b) 200-mesh Cu R1.2/1.3 Quantifoil, (c) 300-mesh ANTcryo R1.2/1.3 Nanodim, (d) 200-mesh Au R2/1 Quantifoil, (e) 200-mesh Au R1.2/1.3 Quantifoil, (f) 300-mesh Au-flat R1.2/1.3 Protochips. White scale bar represents 20 nm.

# Protocol

## EPU automatic data collection workflow (Steps 24-28)



**Extended Data Fig. 3 | EPU automatic data collection workflow.** This figure relates to Steps 24-28. (a-f) Representative images of (a) Atlas mode, (b) GridSquare mode with darker color indicating thicker ice, (c) automatic hole selection (green circles), (d) manually adjusted “Filter Ice Quality” threshold to only include holes with proper ice thickness, (e) Hole/EucentricHeight mode to

set up multiple exposure data collection (green circles with green squares inside) with superimposed “Autofocus Area” (blue circle with blue square inside) and “Drift Measurement Area” (purple circle) on the carbon film, (f) Data Acquisition mode. Scale bars are embedded into the figures.